

Correlated Quantum Phenomena of Spin-Orbit Coupled Perovskite Oxide Heterostructures: Cases of SrRuO₃ and SrIrO₃ Based Artificial Superlattices

Seung Gyo Jeong, Jin Young Oh, Lin Hao, * Jian Liu, * and Woo Seok Choi*

Unexpected, yet useful functionalities emerge when two or more materials merge coherently. Artificial oxide superlattices realize atomic and crystal structures that are not available in nature, thus providing controllable correlated quantum phenomena. This review focuses on 4d and 5d perovskite oxide superlattices, in which the spin-orbit coupling plays a significant role compared with conventional 3d oxide superlattices. Modulations in crystal structures with octahedral distortion, phonon engineering, electronic structures, spin orderings, and dimensionality control are discussed for 4d oxide superlattices. Atomic and magnetic structures, $J_{\rm eff}=1/2$ pseudospin and charge fluctuations, and the integration of topology and correlation are discussed for 5d oxide superlattices. This review provides insights into how correlated quantum phenomena arise from the deliberate design of superlattice structures that give birth to novel functionalities.

1. Introduction

1.1. Oxide Heterostructures

Heterostructures composed of transition metal oxides have been celebrated for decades in fundamental condensed matter research as they serve as one of the key material systems for the development of future functional devices, including thermal, optical, electronic, magnetic, and energy devices.^[1–8] Because of the

S. G. Jeong, J. Y. Oh, W. S. Choi Department of Physics Sungkyunkwan University Suwon 16419, South Korea E-mail: choiws@skku.edu

L. Hao

Anhui Key Laboratory of Condensed Matter Physics at Extreme Conditions High Magnetic Field Laboratory

HFIPS

Chinese Academy of Sciences Hefei, Anhui 230031, P. R. China E-mail: haolin@hmfl.ac.cn

J. Liu
Department of Physics and Astronomy
University of Tennessee
Knoxville, TN 37996, USA
E-mail: jianliu@utk.edu

The ORCID identification number(s) for the author(s) of this article can be found under https://doi.org/10.1002/adfm.202301770

DOI: 10.1002/adfm.202301770

strong internal electric field generated by the oxygen ions, the chemical bonding nature between the various transition metal elements and oxygen ions is either covalent or ionic.[9] This strong chemical bonding ensures highly coherent lattice matching epitaxial relationship between the thin films and the substrates or between the different lavers within oxide heterostructures.[4,10] Such coherent structure is not attainable in structures with, e.g., van der Waals bonding.[11,12] This feature also distinguishes oxide heterostructures from semiconductor heterostructures, which shape the contemporary electronics industry, by embedding correlated functionalities for further scalable and energy-efficient multifunctional devices. Hence, the idea of stacking the building

blocks of transition metal oxides with various physical and chemical properties to exploit synergetic functionality has been prevalent in the field. Oxide heterostructures can ideally realize combinatorial devices that can simultaneously sense, compute, memorize, and actuate by epitaxially combining the necessary layers. Moreover, the functionalities of each layer can be altered as they are being combined, thereby leading to emergent synergetic functionalities. Thus, the opportunity to develop new materials has been maximized.

Epitaxial oxide heterostructures have led to a revolutionary expansion in the fundamental physical and chemical sciences.^[4] In addition to the conventional strong correlation among charge, spin, lattice, and orbital degrees of freedom in a single transition metal oxide compound, oxide heterostructures of transition metal oxides provide important tuning parameters, [5] such as epitaxial strain, octahedral distortion, structural symmetry constraints, charge transfer, magnetic and superconducting proximity, orbital engineering, interfacial band bending, ferroelectric field effect, quantum tunneling, dimensional crossover, and inversion symmetry breaking. The systematic and facile control of these parameters has deepened our understanding of the underlying mechanisms of the functionalities.^[13] In particular, the ondemand growth of oxide heterostructures has allowed us to explore the vast landscape of intriguing and important problems in the field.

Oxide superlattices employ coherent lattice structures of the oxide heterostructures to the very limit, which is a single atomic layer.^[4] They promote single-crystalline structures that are not

1616928, 2023, 3, B. Downloaded from https://onlinelibrary.wiley.com/doi/10.1002/adfm.202301770 by University Of Temnessee Gsm, Wiley Online Library on [14/04/2024]. See the Terms and Conditions (https://onlinelibrary.wiley.com/ems-and-conditions) on Wiley Online Library for rules of use; OA articles are governed by the applicable Creative Commons Licenses

Table 1. Correlation strength in 3d, 4d, and 5d transition metal oxide superlattices. The symbols U, λ , and Δ represent on-site Coulomb interaction, spin-orbit coupling, and crystal field splitting energy, respectively.

Elements	<i>U</i> [eV]	λ [eV]	Δ [eV]
3d	5 – 7	0.01–0.10	1–2
4d	0.5–3	0.1-0.3	2–3
5d	0.4–2	0.1–1	3–4

available in nature, thereby overcoming the thermodynamic constraints for spontaneous natural crystal formation. The development of atomic-scale precision control of the layers enabled genuine man-made crystals with facile tunability of the lattice structures and periodicity. Even though the strong correlation often occurring in oxides largely modifies the structure, the electronic band structure is essentially the energy eigenfunction of electrons under a periodic potential. Hence, the control of the periodic potential via artificial engineering of lattices fundamentally allows altering the physical and chemical properties of the material. For example, the size of the unit cell of superlattices can be digitally increased with the periodicity superimposing the original periodicity of each constituent layer, giving rise to the band folding in the momentum space with the formation of minibands. By exploiting the aforementioned strong covalent/ionic bonding between the transition metal and oxygen, the crystalline symmetry, chemical stoichiometry, and dimensionality of the artificial crystal can be further modified. The strong covalent/ionic bonding also underscores the importance of the functional interfaces, the effect of which is considerably amplified in superlattices.

The numerous oxide superlattices can be classified in several ways. For example, tricolor superlattices, in which the inversion symmetry is broken, can be distinguished from conventional bi-color superlattices.^[10] Additionally, the global structures of the superlattices, for example, perovskite, spinel, pyrochlore, and brownmillerite, can be a basis for classification. However, the vast majority of oxide superlattices studied to date have perovskite structures. One can also categorize the oxide superlattices by focusing on the transition metal elements. Whereas 3d transition metal oxides have been intensively studied over the last several decades, recently, 4d and 5d transition metal oxides have become increasingly important with the introduction of appreciable spin-orbit coupling (λ), of which the strength is comparable to the on-site Coulomb interaction (U) and crystal field splitting energy (Δ) within the transition metal oxygen octahedra (Table 1). As a result of the various spin-orbit-entangled degrees of freedom and their non-trivial interactions, numerous exotic correlated phases can be realized in 4d and 5d transition metal oxides, including spin-orbit-assisted Mott insulators, $J_{\rm eff} = 1/2$ magnetism, quantum spin liquids, excitonic magnetism, multipolar orderings, and correlated topological semimetals.^[14] The combination of these novel spin-orbitentangled states with conventional oxide superlattice approaches provides a new frontier of correlated quantum phenomena with practical controllability that inspires future quantum electronic devices with various functionalities. Therefore, oxide superlattices containing 4d and 5d transition metal oxide layers possess



Figure 1. Schematic summary of artificial 4d and 5d oxide superlattices with their versatile functionalities.

correlated functional physics beyond that in superlattices with 3d transition metal elements, as schematically shown in Figure 1. Herein, first, we briefly summarize previous studies on 3d oxide superlattices, the idea and methods of which can be applied and extended to 4d and 5d oxide superlattices. Subsequently, we discuss the 4d and 5d oxide superlattices in further depth.

1.2. 3d Based Superlattice

Most traditional 3d perovskite oxides have been used as constituent layers in superlattices. Titanates (SrTiO₃, BaTiO₃, CaTiO₃, and LaTiO₃) have been extensively studied, partly owing to the intriguing physical behavior of SrTiO3, including its quantum paraelectric nature and ability to accommodate oxygen vacancies. Before the discovery of unexpected metallic behavior at the interface between two band insulators, i.e., LaAlO₃ and SrTiO₃, [15] the interface between a Mott insulator and a band insulator, i.e., LaTiO3 and SrTiO3, respectively, was found to be metallic owing to the "electronic reconstruction." [16] LaTiO₃/SrTiO₃ superlattices provided an ideal testbed for experimental examination of the unexpected metallic interface as they effectively amplify the conducting signature observed not only from the transport measurements but also by optical spectroscopy. As shown in Figure 2a, the structure can be viewed as a La substitution for Sr within the SrTiO₃ matrix in a layer-by-layer manner, i.e., delta-doping. Optical spectroscopy characterizes the intrinsic carrier density of the entire superlattice, as shown in Figure 2b.[17] Here, the sheet carrier density is independent of the overall La concentration, thus indicating that only the interface is metallic and not the entire sample. Note that such observation would have been extremely difficult with a single interface in conventional oxide heterostructures. The LaTiO₂/SrTiO₂ interface has the potential for use in transparent conducting electrode applications as the visible light can penetrate the sample

16163028, 2023, 38, Downloaded from https://onlinelibrary.wiley.com/doi/10.1002/adfm.202301770 by University Of Termessee Gsm, Wiley Online Library on [14/04/2024]. See the Terms and Conditions (https://onlinelibrary.wiley.com/to-

nditions) on Wiley Online Library for rules of use; OA articles are governed by the applicable Creative Commons I

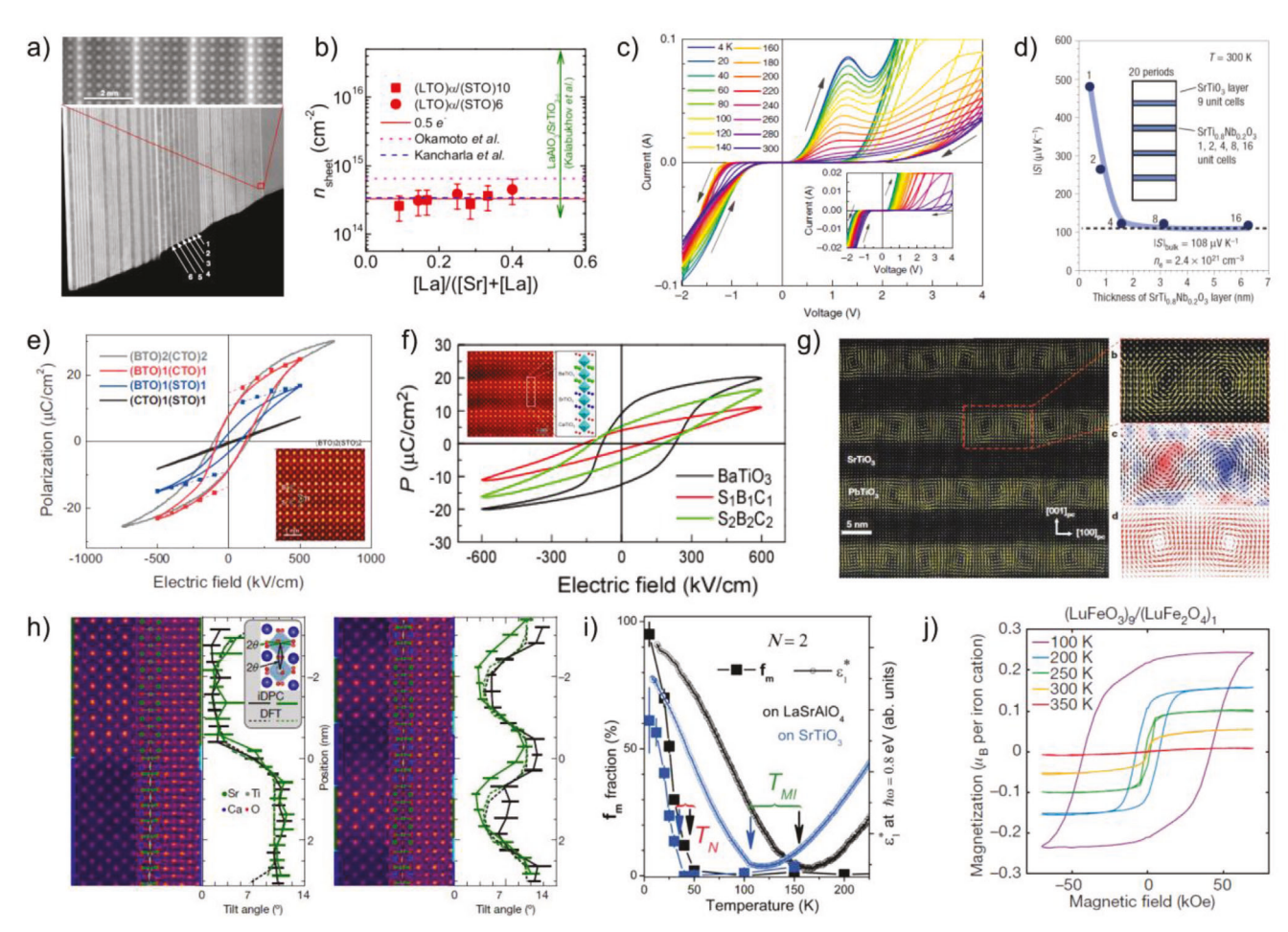


Figure 2. a) Cross-section scanning transmission electron microscopy image. Reproduced with permission. [16] Copyright 2002, Springer Nature. b) Optical spectroscopy analysis for sheet carrier density $n_{\rm sheet}$. Reproduced with permission. [17] Copyright 2007, American Physical Society. c) Quantum resonant tunneling results of LaTiO₃/SrTiO₃ superlattices. Reproduced with permission. [21] Copyright 2015, Springer Nature. d) Seebeck coefficient S in SrTiO₃/SrTiO₃, NbO₂O₃ superlattices with varying SrTiO₃, NbO₂O₃ thickness. Reproduced with permission. [24] Copyright 2007, Springer Nature. e) Polarization hysteresis of Ti based superlattices. Reproduced with permission. [25] Copyright 2007, Wiley-VCH GmbH. f) Polarization hysteresis of Ti based tricolor superlattices. Reproduced with permission. [10] Copyright 2005, Springer Nature. g) Observation of polar vortex in PbTiO₃/SrTiO₃ superlattices Cross-section scanning transmission electron microscopy with magnified image, the curl of the polar displacement, and polarization vector from simulation are shown. [27] Copyright 2016, Springer Nature. h) Octahedral tilt angle of different thicknesses of SrTiO₃/CaTiO₃ superlattices from annular dark-field and integrated differential phase contrast image. Reproduced with permission. [28] Copyright 2022, Springer Nature. i) Temperature-dependent muon ratio f_m affected by local magnetic field and normalized permittivity e_1 * in LaNiO₃/LaAlO₃ superlattices grown on LaSrAlO₄ and SrTiO₃ each. Reproduced with permission. [34] Copyright 2011, American Association for the Advancement of Science. j) Temperature-dependent magnetic hysteresis of (LuFeO₃)₉/(LuFe₂O₄)₁ superlattices. Reproduced with permission. [35] Copyright 2016, Springer Nature.

without much absorption.^[18] The La delta-doping approach was later developed as fractional doping of the superlattice, thus enabling control of the carrier density at the interfaces.^[19] This approach was found to be beneficial for thermoelectric applications.^[20] Another important functionality of LaTiO₃/SrTiO₃ superlattices is quantum resonant tunneling (Figure 2c).^[21] This report is the first observation of resonant tunneling in oxide superlattices, which has been an important subject in semiconductor superlattices. On the other hand, the dimensional quantum confinement of 3d¹ electrons was optically characterized in the LaTiO₃/LaAlO₃ superlattices.^[22]

As in the case of La doping, SrTiO₃ is a very effective system that exhibits a wide variety of electronic phases (from insulator to superconductor) upon doping. Nb doping has proven to be efficient, and by constructing superlattices of metallic

Nb-doped $SrTiO_3$ and $SrTiO_3$ layers, the dimensionality of the metallic layer can be reduced to the thickness of a single unit cell. One of the merits of the reduced dimension is the enhancement of the electron-phonon coupling, which increases the thermopower of the low-dimensional system, as shown in Figure 2d.^[23,24]

Titanate superlattices have been extensively studied in terms of their ferroelectric properties. BaTiO $_3$ is ferroelectric, SrTiO $_3$ is incipient ferroelectric, and CaTiO $_3$ is paraelectric. However, by combining these materials at the atomic scale, the ferroelectricity can be further enhanced, as shown in Figure 2e. The paraelectric layers become ferroelectric owing to cooperative structural distortion within the superlattices. On the other hand, the three titanate perovskites can be combined to form tricolor superlattices with inherent inversion symmetry breaking. Inversion

www.afm-journal.de

16163028, 2023, 3.8, Downloaded from https://onlinelibrary.wiley.com/doi/10.1002/adfm.202301770 by University Of Temnessee Gsm, Wiley Online Library on [14/04/2024]. See the Terms and Conditions (https://onlinelibrary.wiley.com/terms-and-conditions) on Wiley Online Library for rules of use; OA articles are governed by the applicable Creative Commons Licenses

symmetry breaking is essential for the emergence of ferroelectricity, and ferroelectricity may be expected even with nonferroelectric constituents. The tricolor superlattices exhibit enhanced ferroelectric polarization, thus corroborating the intuitive symmetry-breaking mechanism (Figure 2f).[10] Such a polar order could be further modified by geometric constraints offered by the oxide heterostructures. The epitaxial tensile strain in PbTiO₃/SrTiO₃ multilayers induced flux-closures, [26] which was later extended to smaller polar vortex structures in PbTiO₃/SrTiO₃ superlattices, as shown in Figure 2g.^[27] Furthermore, the modulation of the lattice structure and interfaces leads to an entirely different global vibrational response of the superlattices (Figure 2h), thereby leading to a greater control over the thermal conductivity.[28,29]

Except for titanates, 3d perovskite superlattices have been realized using vanadates, [30] manganites, [31] ferrites, [32] cobaltites, [33] and nickelates.^[34] In nickelates, the dimensionality change results in a collective change in the correlated electronic and magnetic phase transitions (Figure 2i). For oxide superlattices other than perovskites, hexagonal LuFeO3 superlattices have representatively demonstrated magnetoelectric coupling promoted by geometric ferroelectricity (Figure 2j).[35]

This review summarizes recent studies on 4d and 5d oxide superlattices. Most of the 4d and 5d superlattices studied thus far contain SrRuO₃ and SrIrO₃ layers, respectively. Hence, herein, we focus on the superlattices of these two important materials. Chapter 2 introduces state-of-the-art atomic-scale epitaxy techniques that enable the realization of artificial superlattices. Chapter 3 discusses the SrRuO₃ based superlattices. Starting from the lattice structure modulation, we discuss artificial phonon engineering, ferromagnetism, dimensionality-induced phase transition, and topologically nontrivial spin structures. In Section 4, we discuss SrIrO₃ based superlattices. The crystal structure, epitaxial strain, spin-charge fluctuation, and fluctuation of $J_{\text{eff}} = 1/2$ pseudospin in the 2D limit are discussed. We will further compare the natural layered crystal of the Ruddlesden-Popper series with the superlattices. Finally, we summarize this review in Section 5 with an outlook.

2. Atomic Scale Epitaxy Techniques: Realization of Artificial Oxide Crystal

The development of modern epitaxy techniques has provided atomic-scale precision controllability of state-of-the-art oxide heterostructures. Prominent epitaxy techniques for realizing oxide superlattices include sputter deposition, pulsed laser epitaxy, and molecular beam epitaxy. Sputtering was first employed to fabricate iron oxide films in 1852.[36,37] To this day, sputtering is widely used for thin film growth as it is economical and useful for mass production in the industry.[38]The sputtering process uses the plasma produced by electrical discharge and the electrostatic acceleration of ions to deposit the thin film material on the substrate surfaces. Oxide heterostructures and superlattices can be grown using two target compounds. High-quality oxide superlattices grown by sputter deposition include cuprates, [39] titanates, [38,40] ruthenates, [41] nickelates, [42,43] and manganites. [44]

Owing to the improvement in vacuum techniques in the 1960s, both pulsed laser epitaxy and molecular beam epitaxy have been developed. [45,46] Pulsed laser epitaxy is one of the most appreciated approaches that demonstrate the atomic-scale epitaxy of oxide superlattices. The thin film growth process is as follows.[47] 1) A pulsed laser ablates the surface of a target in a vacuum chamber and generates a plasma plume. 2) The plasma plume propagates and reaches the heated substrate. 3) The ion clusters crystallize on the substrate surface through a thermodynamic process. Pulsed laser epitaxy is useful for synthesizing complex heterostructures and superlattices using a target manipulator. The growth window of pulsed laser epitaxy is typically wide for transition metal oxides and can be modulated using several experimental parameters, such as the laser (pulse energy and repetition rate), substrate (material, surface, and temperature), and type of background gas, pressure, and flow rate in the growth chamber.^[48] In particular, the interaction (or scattering) between the plasma and the background gas determines the kinetics, oxidation state, and stoichiometry of the incoming plume, as well as the final surface dynamics of the incoming species. These factors settle the growth mechanisms of oxide thin films, for example, the layer-by-layer, step flow, and island growth modes. [47,49-51] For example, in cases of SrRuO3 and SrIrO3-based superlattices, the growth of the thin film layer of SrRuO3 and SrIrO3 depends sensitively on the substrate temperature, oxygen background pressure, and laser fluence. First, due to the volatile nature of Ru ions at high temperatures, substrate temperatures of around 700 °C are commonly used. Second, a sufficiently oxygen-rich environment of 100 mTorr is required to synthesize stoichiometric SrRuO₃ and SrIrO₃ layers. [49,52] Third, since high laser fluence can induce unintended cation vacancies and change the growth modes, $^{[53,54]}$ a laser fluence of around 1.2 J cm $^{-2}$ is typically used for the growth of SrRuO₃ (and SrIrO₃) layers. Finally, when constructing a superlattice, we should consider the deposition conditions of the partner layer, ensuring that they do not compromise the functionality of SrRuO3 (or SrIrO3). It is crucial to experimentally verify whether the selected deposition conditions are appropriate. Although measuring small changes in the chemical composition ratio of SrRuO3 according to these changes in experimental conditions may be difficult, the variations in the ferromagnetic phase transition temperature and electrical transport behaviors are rather sensitive. [49,53] On the other hand, by adjusting the number of laser pulses, the growth of each layer within a superlattice can be accurately controlled with atomic-scale precision, even without reflection high energy electron diffraction.^[55] Thanks to the versatile technical advantages, the majority of oxide superlattices with atomic-scale precision thickness control have been reported as using pulsed laser epitaxy.

Molecular beam epitaxy supplies each constituent element of perovskite oxide independently, under ultrahigh vacuum conditions, whereas both sputtering and pulsed laser epitaxy typically use stoichiometric ceramic targets. Molecular beam epitaxy offers selective cation control of perovskite oxides with atomic-scale precision thickness control via the instantaneous shutter control of individual elements.^[56] High-vacuum conditions also provide a high mean free path for electrons and ions suitable for in-situ characterizations, including high-energy electron diffraction, low-energy electron diffraction, X-ray photoelectron spectroscopy, and Auger electron spectroscopy. One of the experimental parameters of oxide molecular beam epitaxy for stoichiometric films is the oxidant and/or the oxidant background pressure. Because molecular oxygen in early oxide

1616928, 2023, 3, B. Downloaded from https://onlinelibrary.wiley.com/doi/10.1002/adfm.202301770 by University Of Temnessee Gsm, Wiley Online Library on [14/04/2024]. See the Terms and Conditions (https://onlinelibrary.wiley.com/ems-and-conditions) on Wiley Online Library for rules of use; OA articles are governed by the applicable Creative Commons Licenses

Table 2. Summary of reported 4d SrRuO₃ based superlattices. [41,54,55,70,86–164]

molecular beam epitaxy is insufficient in numerous cases, oxygen plasma and/or ozone gases have become popular for achieving more aggressive oxidizing environments; however, they are accompanied by high vapor pressure and require external vapor inlet systems. More recently, solid source metalorganic molecular beam epitaxy has been suggested to obtain low vapor pressures and low source temperatures, which is more stable and cheaper compared with other oxide molecular beam epitaxies. [57] Finally, atomic layer deposition has also proven to be useful in depositing oxide thin films, although the realization of perovskite oxide superlattices has yet to be demonstrated.

3. 4d SrRuO₃ Based Superlattices

The 4d perovskite oxide SrRuO₃ exhibits itinerant ferromagnetism with various correlated functionalities.^[58-60] In bulk, SrRuO₃ exhibits an orthorhombic structure at room temperature with the *Pbnm* space group having $a^-a^-c^+$ rotation pattern in the Glazer notation. The bulk lattice constants are a = 5.5670 Å, b =5.5304 Å, and c = 7.8446 Å in orthorhombic notation, ^[61] whereas the pseudo-cubic lattice constant is 3.93 Å.[49] Owing to their chemical stability, electrical conductivity, and versatile physical properties, SrRuO₃ films have received considerable attention for both fundamental correlated physics and applications. [58] In particular, the spin-orbit coupling strength of the 4d Ru ions is comparable to the electronic correlation energy scales, for example, Hund's coupling, crystal field splitting, and electron hopping, [14] thus leading to novel spin-orbit-coupled electronic ground states and physical phenomenon. The three Ru t_{2g} orbitals (d_{xy} , d_{xz} , and d_{v2}) within SrRuO₃ are filled with four electrons following Hund's rule, thereby stabilizing S = 1 spin states in the bulk.^[62] Theoretical calculations suggested a half-metallic behavior with Stoner spin splitting of SrRuO₃.^[63] When the stoichiometry deviates from the ideal SrRuO₃, for example, when Ru–O vacancies are introduced, a structural phase transition from orthorhombic to tetragonal is observed, along with changes in the electronic and chemical behaviors.[49,64]

By taking advantage of the epitaxial heterostructuring, facile control over the d-electron configuration, octahedral bonding geometry, crystalline symmetry, magnetic interactions, and electronic dimensionality can be achieved. Since the first growth of single-crystalline SrRuO₂ epitaxial films in 1992 reported by Eom et al., [65] numerous SrRuO₃ heterostructures have been demonstrated to exhibit intriguing functional phenomena, such as metal-insulator transition, [66,67] structural phase transition, [68,69] electrocatalytic activity, [64] spinphonon coupling,^[70] itinerant ferromagnetism,^[71,72] controllable magnetic anisotropy,[52,73] anomalous and/or topological Hall effect, [74-79] Weyl fermion behavior, [80] topological magnon, [81,82] and chiral phonon-mediated magnetic interactions. [55] Several studies have demonstrated epitaxially grown SrRuO3 thin films on SiO₂/Si substrates,^[83–85] which implies the potential integration of correlated functional oxides with Si based electronics. Atomically designed SrRuO3 superlattices provide further extended controllability of the correlated functionalities, depending on the type of partner oxide layer and substrate, chemical stoichiometry, individual layer thickness, repetition number, and stacking order of the supercell structure. Table 2 summarizes the reported SrRuO₃ based superlattices with various functional part-

4d SrRuO ₃ based superlattices	Functionality of partner compounds	Refs.
SrRuO ₃ /SrTiO ₃	Quantum paraelectric	[54,55,70,86–110]
SrRuO ₃ /BaTiO ₃	Ferroelectric	[111,112]
SrRuO ₃ /PbTiO ₃		[41,114]
SrRuO ₃ /PbZr _{0.52} Ti _{0.48} O ₃		[113,115]
SrRuO ₃ /LaAlO ₃	Dielectric	[116]
SrRuO ₃ /SrCuO ₂	Infinite layer	[117]
SrRuO ₃ /La _{0.7} Sr _{0.3} MnO ₃	(Anti-)Ferromagnetic	[118–137, 143]
SrRuO ₃ /Pc _{0.7} Ca _{0.3} MnO ₃		[138-143]
SrRuO ₃ /La _{0.7} Ca _{0.3} MnO ₃		[144–146]
SrRuO ₃ /PrMnO ₃		[147–149]
SrRuO ₃ /SrMnO ₃		[150–155]
SrRuO ₃ /LaCoO ₃		[156]
SrRuO ₃ /LaNiO ₃		[157]
SrRuO ₃ /BiFeO ₃	Multiferroic	[158–160]
SrRuO ₃ /SrIrO ₃	5d oxides	[161–163]
SrRuO ₃ /SrIrO ₃ /SrZrO ₃ SrRuO ₃ /SrHfO ₃ /SrZrO ₃		[164]

ner compounds. $[^{41,54,55,70,86-164}]$ Herein, several emergent functionalities of SrRuO₃ based superlattices and their modulations are reviewed in the following Sections.

3.1. Modulation of Correlated Lattice Degree of Freedom

The customized lattice degree of freedom of orthorhombic SrRuO₃ provides a facile control knob for determining multiple correlated functionalities.^[58] A theoretical study proposed that the orthorhombic SrRuO3 with an octahedral distortion and the tetragonal SrRuO₃ without octahedral tilt have almost the same formation energy, differing by only a few tens of meV.[165] By taking advantage of the nearly degenerate state of the orthorhombic and tetragonal structures of SrRuO₃, it is possible to control the octahedral tilt and stabilize various structural phases through epitaxial heterostructures. Such structural modification modulates the ferromagnetic behavior (transition temperature, coercive field, magnetic easy axis, and magnetization value), electronic structure (crystal field and orbital hybridization), magnetotransport, and topological behavior. This section introduces various structural modulations in SrRuO₂ based superlattices from microscopic octahedral distortion to macroscopic crystalline symmetry.

3.1.1. Octahedral Distortion

Contemporary scanning transmission electron microscopy can directly visualize minute distortions of RuO₆ octahedra in SrRuO₃ based heterostructures. Wang et al. reported the SrRuO₃ thickness-dependent evolution of lattice mismatch within SrRuO₃/LaCoO₃ multilayers grown on SrTiO₃ substrates using selected-area electron diffraction patterns (**Figure 3**a). [156]

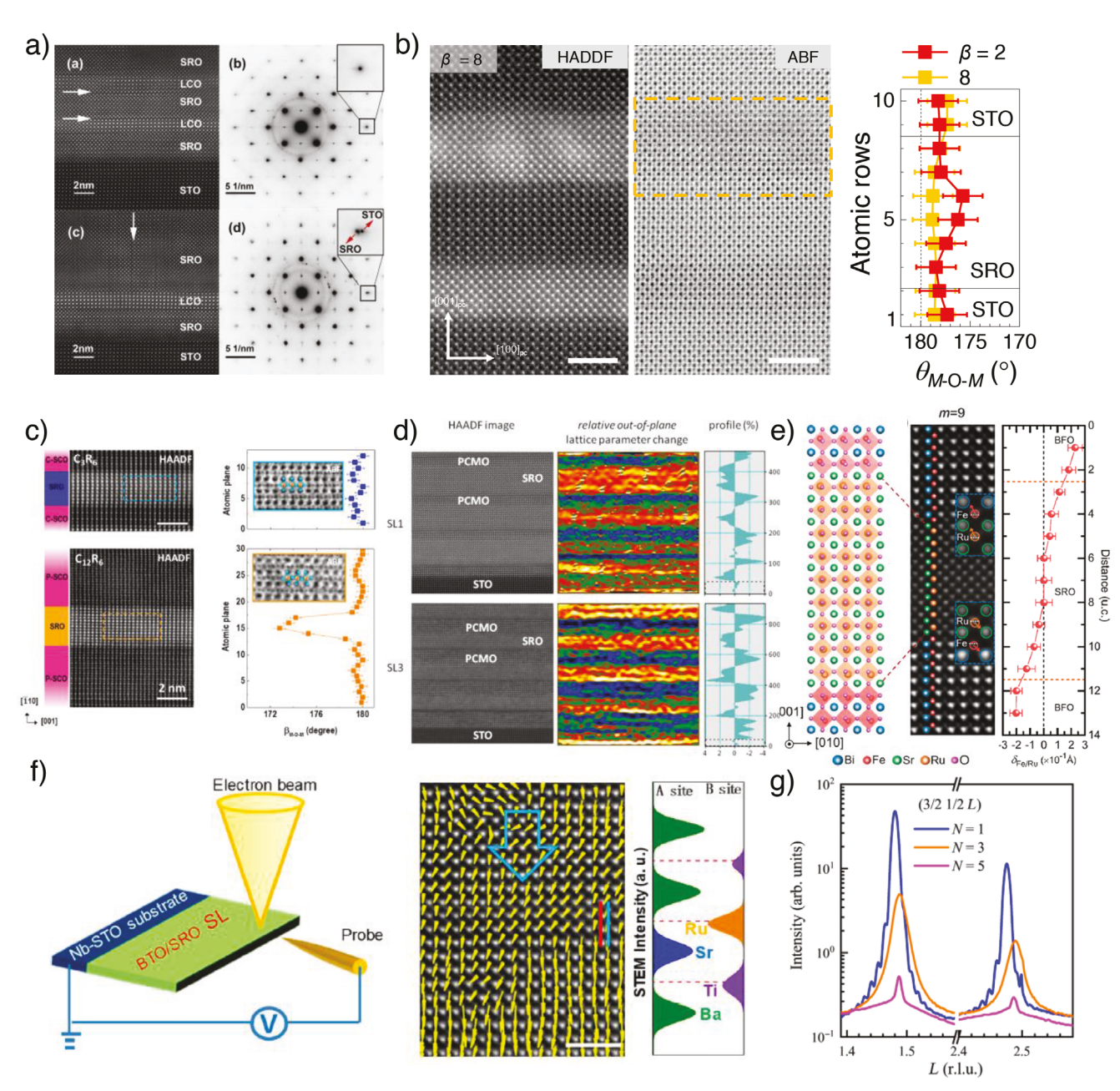


Figure 3. a) Cross-sectional scanning transmission electron microscopy and selected area electron diffraction images of SrRuO₃/LaCoO₃ multilayer thin films with different SrRuO₃ layer thickness. Reproduced with permission. Copyright 2018, Elsevier. b) Scanning transmission electron microscopy images for SrRuO₃/SrTiO₃ superlattices and propagation of octahedral distortion angle with respect to SrTiO₃ layer thickness. Reproduced with permission. Copyright 2020, Wiley-VCH GmbH. The scale bars denote 2 nm. c) Scanning transmission electron microscopy image and octahedral distortion angle of SrRuO₃/SrCuO₂ superlattices. Reproduced with permission. Copyright 2021, American Chemical Society. d) Scanning transmission electron microscopy image, mapping for relative out-of-plane lattice parameter deviation of SrRuO₃/Pr_{0.7}Ca_{0.3}MnO₃ superlattices from SrTiO₃ and its profile. Reproduced with permission. Copyright 2011, IOP Publishing. e) Schematic, scanning transmission electron microscopy image of interfacial SrRuO₃/BiFeO₃ multilayer structure and its ionic displacements induced by ferroelectric polarization of BiFeO₃. Reproduced with permission. Speriodiced with permission. Speriodiced Society. f) Schematic and polar map of in situ transmission electron microscopy for electrical field control of Ru ion displacement through ferroelectric polarization in SrRuO₃/BaTiO₃ superlattices. The blue arrow means downward polarization direction. Reproduced with permission. Copyright 2020, American Chemical Society. g) Observation on octahedral distortion of SrRuO₃/SrTiO₃ superlattice by half-order X-ray diffraction measurements. Reproduced with permission. Copyright 2020, American Association for the Advancement of Science.

16163028, 2023, 3.8, Downloaded from https://onlinelibrary.wiley.com/doi/10.1002/adfm.202301770 by University Of Temnessee Gsm, Wiley Online Library on [14/04/2024]. See the Terms and Conditions (https://onlinelibrary.wiley.com/terms-and-conditions) on Wiley Online Library for rules of use; OA articles are governed by the applicable Creative Commons Licenses

www.advancedsciencenews.com

CIENCE NEWS

The authors detected Ruddlesden-Popper-type faults induced by excessive Sr ions within the SrRuO3 layers. The microstructure could be further modified by controlling the SrRuO₂ layer thickness. Jeong et al. demonstrated the propagation of octahedral distortions in SrRuO₃/SrTiO₃ superlattices. Even for the same thickness of the SrRuO3 layer, the octahedral distortion was systematically modulated by controlling the atomicscale thickness of adjacent SrTiO₃ layers (Figure 3b).^[91] Reportedly, as the STO thickness increased, the cubic nature of the SrTiO₃ layer better restrained the octahedral distortion of the SrRuO₃ layer within the superlattices. A similar approach was adopted by Shan et al., in which the octahedral distortion in SrRuO₃/SrCuO₂ superlattices was modulated by dimensionality control of the infinite layered SrCuO2 (Figure 3c).[117] With decreasing SrCuO2 layer thickness, the CuO2 infinite layer was shown to change from planar to chain-type, which modulated the polyhedral connectivity at the interface. On the other hand, Ziese et al. showed that the out-of-plane lattice constant for the SrRuO₃ layer in SrRuO₃/Pr_{0.7}Ca_{0.3}MnO₃ superlattices could be controlled by the thickness of the Pr_{0.7}Ca_{0.3}MnO₃ layer (Figure 3d).^[141] Yao et al. suggested that the ferroelectric polarization of BiFeO3 induced ionic displacements of the interfacial SrRuO₃ layer in the SrRuO₂/BiFeO₂ multilayers (Figure 3e).^[158] This modified the metallic SrRuO₃ layer. Mao et al. further demonstrated electrical field control of the Ru ion displacement via switchable ferroelectric polarization in a SrRuO3/BaTiO3 superlattice using in situ transmission electron microscopy, as shown in Figure 3f.[112] By applying an electrical field along the out-of-plane direction, they controlled the ion displacement in both the atomically thin metallic SrRuO3 and ferroelectric BaTiO3 layers within the superlattice. Specifically, the asymmetry between the top BaO-RuO2 and bottom SrO-RuO₂ interfaces induces bistable switchable polarization, leading to an electrical field control of Ru ion displacements. On the other hand, finite octahedral rotation led to the two perovskite unit cell periodicity (unit cell doubling) and the resultant half-order Bragg diffraction peak, as studied by May et al. [166] Figure 3g shows the octahedral distortion variation in the SrRuO₃/SrTiO₃ superlattice observed by half-order diffraction measurements using synchrotron X-ray facilities.[107]

3.1.2. Crystalline Symmetry

The RuO₆ octahedral distortion determines the crystalline symmetry of SrRuO3 based superlattices. Off-axis X-ray diffraction measurements around (204) SrTiO₃ Bragg reflections with four different azimuth angles (ϕ) of 0°, 90°, 180°, and 270° typically revealed the asymmetric crystal structure of orthorhombic SrRuO₃ heterostructures (Figure 4a).[49] In conventional SrRuO₃ single films, the crystalline symmetry of SrRuO₃ is modulated by controlling the thickness, [68] epitaxial strain, [69] and chemical composition of the SrRuO₂ layers. [64] For superlattices, the control of octahedral tilt propagation was shown to result in an orthorhombic to tetragonal structural phase transition in SrRuO₃/SrTiO₃ superlattices by manipulating the thickness of the SrTiO₃ layer (Figure 4b).[91] A structural phase map as a function of both SrRuO₂ and SrTiO₂ layer thicknesses was constructed, as shown in Figure 4c. Despite the same thickness and stoichiometry of the SrRuO3 layer, the interfacial octahedral connectivity between SrRuO3 and SrTiO3 with atomic-scale thickness modulation systematically realized the structural phase transition of the SrRuO₂/SrTiO₂ superlattice. This further modified the electromagnetic properties of the ferromagnetic SrRuO3 layer, including the magnetic coercive field, saturation magnetization, and ferromagnetic transition temperature. Sahoo et al. confirmed similar structural phase transitions in SrRuO₃/PrMnO₃ superlattices by varying the thickness of the PrMnO₃ layer, as shown in Figure 4d.[147] A shift in the magnetic hysteresis loop was observed, and it was enhanced in the case of the tetragonal superlattice, thus indicating crystalline symmetry-dependent interfacial antiferromagnetic coupling. The distorted lattice structure in the SrRuO₃ layer within the superlattice can also influence the crystalline symmetry of the partner layer, with inversion symmetry breaking at the interface. Behera et al. proposed a possible orthorhombic structure in the La_{0.7}Sr_{0.3}MnO₃ layers within SrRuO₃/La_{0.7}Sr_{0.3}MnO₃ superlattices on a (110)-oriented SrTiO₃ substrate using X-ray diffraction and Raman spectroscopy (Figure 4e).[129] Four unit cell layers of La_{0.7}Sr_{0.3}MnO₃, sandwiched between 14 unit cell layers of SrRuO3, exhibited an orthorhombic structure, leading to modification of the magnetic behavior. Using density functional theory calculations and

ferroelectric measurements, Callori et al. discussed the possi-

bility of three different types of interfaces depending on the chemical composition and inversion symmetry breaking in the

SrRuO₃/PbTiO₃ superlattice (Figure 4f).^[41] As the thickness of

the PbTiO₃ layer within the superlattices decreased, the polar-

ization asymmetry was enhanced owing to the compositional

inversion symmetry breaking, which led to modified ferroelec-

tric phases. Hence, the superlattice approach provides facile

and versatile controllability of the bonding geometry in cor-

related quantum oxides, thus providing numerous intriguing

3.2. Correlated Phonon Engineering

functionalities.

Facile structural modification in artificial quantum oxides enables the manipulation of phonon dispersion, phonon group velocity, electric polarization, and the density of states of phonons.[167] This has potential for future acoustic applications, including quantum Bragg mirrors and cavities, [168] quantum acoustic memory and transducers, [169] microwaveoptical converters, [170] quantum amplifiers, [171] and circuit acoustodynamics. [172] Most studies on phonon engineering have been limited to high-quality III-V compound semiconductors. However, recent phonon engineering in correlated oxides can lead to novel applications of tunable coherent phonon excitations for future quantum acoustic devices integrated with their correlated functionalities.

3.2.1. Zone-Folded Phonon and Its Dynamics

The superimposed periodicity of the superlattice induces the backfolding of the acoustic phonon dispersion, thereby generating zone-folded acoustic phonons in the GHz and/or THz frequency range. Jeong et al. demonstrated phonon dispersion in SrRuO₃/SrTiO₃ superlattices, as shown in Figure 5a.^[88] As

1616328, 2023, 3, B. Downloaded from https://onlinelibrary.wiley.com/doi/10.1002/adfm.202301770 by University Of Temnessee Gsm., Wiley Online Library on [14/04/2024]. See the Terms and Conditions (https://onlinelibrary.wiley.com/emes-and-conditions) on Wiley Online Library for rules of use; OA articles are governed by the applicable Creative Commons Licenses

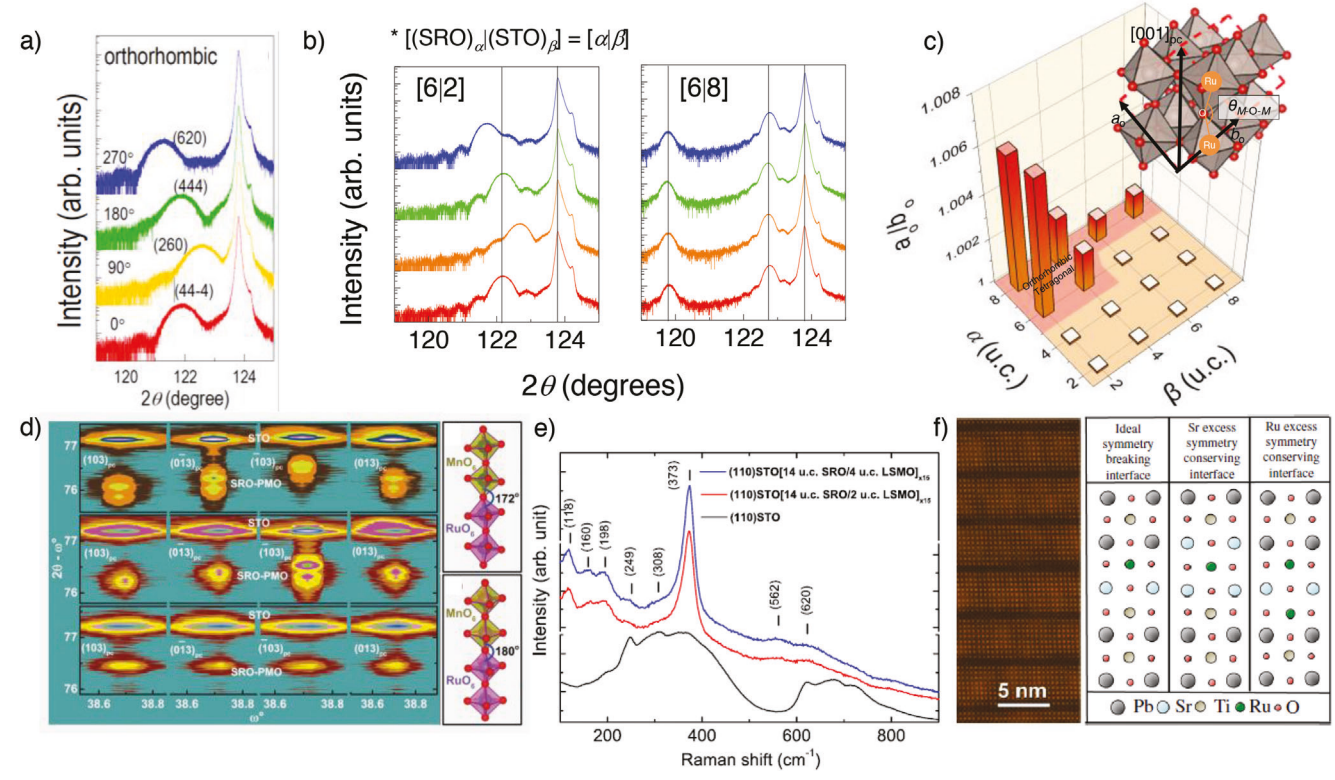


Figure 4. a) Asymmetric crystal structure of orthorhombic SrRuO₃ heterostructure observed by off-axis measurement around (204) SrTiO₃ Bragg reflections with four different azimuth angles. Reproduced with permission.^[49] Copyright 2017, Springer Nature. b) Structural phase transition of SrRuO₃/SrTiO₃ superlattices from orthorhombic to tetragonal as SrTiO₃ layer thickness increases, color notation is same as Figure 4a.^[91] Copyright 2020, Wiley-VCH GmbH. c) Octahedral distortion mapping of SrRuO₃/SrTiO₃ superlattices with respect to SrRuO₃ and SrTiO₃ layer thickness. Reproduced with permission.^[91] Copyright 2020, Wiley-VCH GmbH. d) Structural phase transition of SrRuO₃/PrMnO₃ with respect to PrMnO₃ layer thickness shown by reciprocal space mapping around (103) SrTiO₃ Bragg reflections for four different azimuth angles. Reproduced with permission.^[147] Copyright 2018, Wiley-VCH GmbH. e) Raman spectroscopy of (110) oriented SrTiO₃ and SrRuO₃/La_{0.7}Sr_{0.3}MnO₃ superlattice on (110) oriented SrTiO₃ with different La_{0.7}Sr_{0.3}MnO₃ thickness. Reproduced with permission.^[129] Copyright 2014, AIP publishing. f) Scanning transmission electron microscopy image and the three types of theoretically possible interfaces of SrRuO₃/PbTiO₃ superlattice. Reproduced with permission.^[41] Copyright 2012, American Physical Society.

the supercell periodicity is designed to be ten times of the bulk SrTiO₃ lattice constant, the reciprocal lattice constant of the superlattice decreases by ten times with the appearance of an equivalent backfolded Brillouin zone. This leads to zone-centered acoustic phonons near the Γ -point. The left panel of Figure 5b shows the theoretically estimated phonon dispersion with the presence of zone-folded acoustic phonons in SrRuO₃/SrTiO₃ superlattices. Clear Raman excitations of zone-folded acoustic phonons with systematic control of their excitation frequency in the THz frequency range were demonstrated via precise thickness control of the supercell periodicity (middle and right panels of Figure 5b). Such coherent phonon modes of superlattices were also observed in the time-resolved pump-probe measurement, as shown in the top panel of Figure 5c, studied by Yang et al.[103] By examining the fast Fourier-transformed pump-probe spectra of the SrRuO₃/(SrTiO₃ or SrIrO₃) superlattices, the excitation frequency and mean free path of the zone-folded acoustic phonons were obtained. The bottom panel of Figure 5c shows the experimentally observed phonon mean free path following the theoretical model, thus validating the experimental approaches. Bojahr et al. compared the oscillation phase of zone-folded acous-

tic phonons in optical pump-probe measurements to ultrafast X-ray diffraction in SrRuO₃/SrTiO₃ superlattices (Figure 5d).^[108] Both optical measurements showed the same fluence dependence of the phase but complex wavelength dependence of the broadband data. Schmising et al. reported the ultrafast structural evolution of the lattice and polarization dynamics in a SrRuO₃/PbZr_{0.2}Ti_{0.8}O₃ superlattice using femtosecond X-ray diffraction.^[113] Figure 5e shows the relative angular shift of the selected Bragg reflection, representing a transient expansion of the superlattice structure by 0.24%. The optical excitation of the SrRuO₃ metal layers generates a large stress that compresses the PbZr_{0.2}Ti_{0.8}O₃ layers within the superlattice, thereby offering optically controllable ferroelectric polarizations. On the other hand, the photoinduced ultrafast stress generation in ferromagnetic SrRuO₃ confirmed the subpicosecond magnetostriction effect in the nanolayered SrRuO₃/SrTiO₃ superlattice via ultrafast X-ray diffraction. [95] It was shown that the phonon-mediated and magnetostrictive stress contributions had similar strengths but opposite signs in the SrRuO₃/SrTiO₃ superlattice. The amplitudes of the ultrafast X-ray signals (solid diamonds) followed the temperature-dependent magnetization squared below the

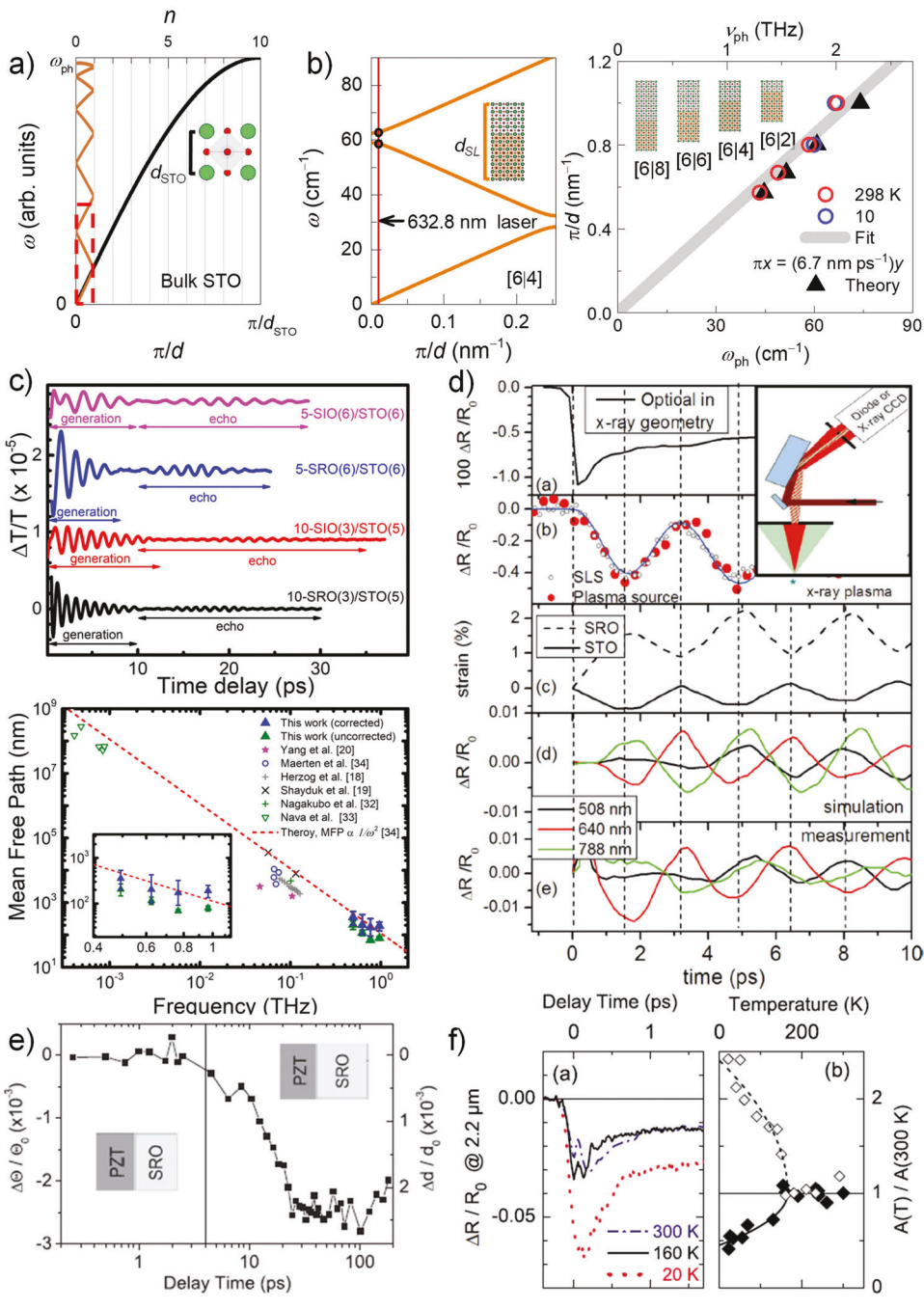


Figure 5. a) Schematic of zone-folded phonon dispersion of bulk SrTiO₃ and SrRuO₃/SrTiO₃ superlattice. The black curve is bulk SrTiO₃ dispersion and the orange curve is zone-folded superlattices dispersion due to *n* times larger supercell lattice. d_{STO} is SrTiO₃ lattice constant. Reproduced with permission. [88] Copyright 2022, Wiley-VCH GmbH. b) Theoretical estimation of zone-folded phonon dispersion of SrRuO₃/SrTiO₃ superlattice from the red box of Figure 5a and Raman spectra, where red, orange, yellow, and green curves are [6|2], [6|4], [6|6], and [6|8] superlattices respectively. Linear relation between phonon frequency $ω_{ph}$ and reciprocal lattice spacing π/d is extracted from the spectra. Reproduced with permission. [88] Copyright 2022, Wiley-VCH GmbH. c) Time-resolved pump-probe of SrRuO₃ (or SrIrO₃)/SrTiO₃ superlattice where T is transmission and frequency-dependent phonon mean free path. Reproduced with permission. [103] Copyright 2021, IOP Publishing. d) Comparison of zone-folded acoustic phonon in SrRuO₃/SrTiO₃ superlattice observed by optical pump-probe measurement and ultrafast X-ray diffraction, reflectivity change with respect to probe wavelength reproduced with permission. [108] Copyright 2012, American Physical Society. e) Relative angular shift $ΔΘ/Θ_0$ of SrRuO₃/PbZr_{0.2}Ti_{0.8}O₃ of the selected (0 0 56) Bragg reflection where $Δd/d_0$ is superlattice period change. Reproduced with permission. [113] Copyright 2007, American Physical Society. f) Optical reflectivity change for three different temperatures and comparison between temperature dependence of the amplitude of the reflectivity change [A(T)/A(300 K)], (open diamond) and superlattice phonon oscillation (solid diamond). Reproduced with permission.

16163028, 2023, 38, Downloaded from https://onlinelibrary.wiley.com/doi/10.1002/adfm.202301770 by University Of Temnes

ee Gsm, Wiley Online Library on [14/04/2024]. See the Terms and Conditions (https://onlinelibrary.wiley.com/terms-and-conditions) on Wiley Online Library for rules of use; OA articles are governed by the applicable Creative Commons License

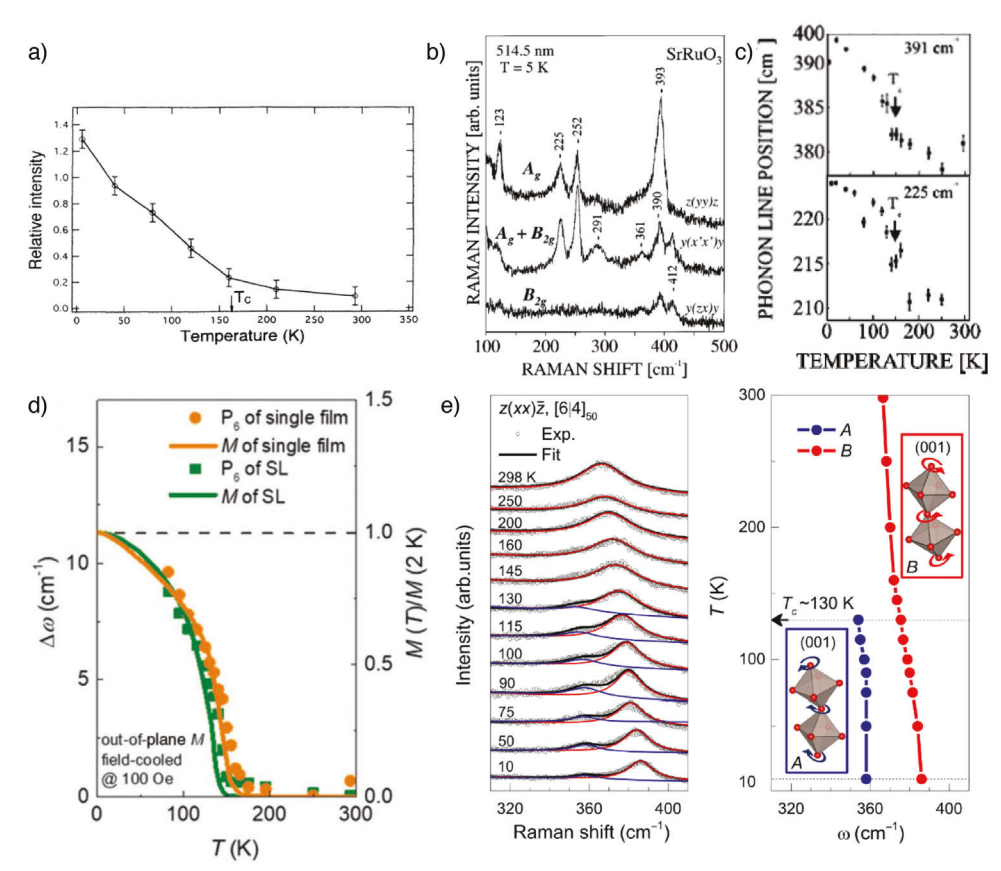


Figure 6. a) Temperature-dependent Raman peak intensity at 250 cm⁻¹ of SrRuO₃ thin film showing phonon anomalies at ferromagnetic transition temperature, T_c is ferromagnetic transition temperature. Reproduced with permission. Copyright 1995, American Physical Society. b) Polarized Raman spectra of ≈300 nm thickness SrRuO₃ thin film on (010) and (001) SrTiO₃ substrates in 3 configurations. Reproduced with permission. Copyright 1999, American Physical Society. c) Temperature dependence of the Raman peak position of (010)-oriented SrRuO₃ thin film, T_c is ferromagnetic transition temperature. Reproduced with permission. Copyright 1999, American Physical Society. d) Temperature dependence of both phonon anomaly, shift of P₆ Raman mode peak $\Delta \omega$ and magnetization to compare spin–phonon coupling of single SrRuO₃ film and SrRuO₃/SrTiO₃ superlattice. Reproduced with permission. Copyright 2020, The Royal Society of Chemistry. e) Phonon mode splitting corresponding to oxygen vibrations with 2 orthogonal polarizations in bulk SrRuO₃ across ferromagnetic phase transition temperature. Reproduced with permission. Copyright 2022, American Association for the Advancement of Science.

ferromagnetic transition temperature. This represents a close interplay between the lattice and spin degrees of freedom in $SrRuO_3$ heterostructures.

3.2.2. Spin-Phonon Coupling

Strong spin–phonon coupling plays an important role in understanding the correlated long-range spin order in SrRuO₃ systems. For example, in 1994, Kirillov et al. reported temperature-dependent Raman spectra of a SrRuO₃ single film to exhibit phonon anomalies at the ferromagnetic transition temperature (**Figure 6a**).^[173] The report However, they could not investigate the polarization selection rules for the phonon analysis owing to the multidomain structure of SrRuO₃ single films. Iliev et al. further developed the polarized Raman spectra of SrRuO₃ films with a thickness of approximately 300 nm grown on (010)- and (001)-oriented SrTiO₃ substrates (Figure 6b). ^[174] The authors tentatively assigned the experimentally observed Raman excitations using lattice dynamical calculations. Figure 6c summarizes the

temperature dependence of the peak position and linewidth of the four different Raman branches of the (010)-oriented SrRuO₃ film. The temperature dependence of the phonon peak position exhibited an anomaly around the ferromagnetic transition temperature. The temperature anomaly of the 391 cm⁻¹ phonon mode (regarding apical oxygen vibrations) could be understood as spin-exchange coupling modulated by ionic displacement. However, other phonon anomalies (especially for the 225 cm⁻¹ phonon mode is mainly related to Sr ion vibration) could not be explained by the conventional magnetostriction effect. This suggests that the mechanism of spin-phonon coupling in SrRuO₃ is complicated. Although the phonon linewidths have a relatively large experimental error, the authors suggested that the linewidth peaked near the transition temperature, which also supports the coupling between the optical phonons and fluctuations of the magnetic order parameter near the phase transition.

A more recent study on $SrRuO_3/SrTiO_3$ superlattices has demonstrated that a similarly strong spin–phonon coupling can be preserved in the atomically thin $SrRuO_3$ layers within the



www.advancedsciencenews.com



www.afm-journal.de

superlattice, as shown in Figure 6d.^[70] A slight difference in the ferromagnetic transition temperature between the single film and superlattice was detected in the phonon spectra, thus providing experimental proof of the preserved spin-phonon coupling. Furthermore, the temperature-dependent Raman spectra of the $SrRuO_3/SrTiO_3$ superlattice show that the phonon mode at \approx 367 cm⁻¹ split into two modes, at \approx 358 and \approx 386 cm⁻¹ below the ferromagnetic phase transition temperature (Figure 6e). The split in phonon mode could be assigned to oxygen vibrations with orthogonal polarizations in orthorhombic bulk SrRuO₃ by utilizing lattice dynamical calculations. It was proposed that the superposition of two orthogonal linear phonon modes with phase differences could give rise to circular phonons, which could combine with spins or magnetic moments.^[55] The molecular field in the ferromagnetic phase of the SrRuO₃ layer induced the phonon Zeeman effect and the resultant temperature-dependent phonon splitting below the ferromagnetic transition temperature in the Raman spectra, thus evidencing chiral symmetry breaking. This revealed a chiral phonon-mediated interlayer exchange interaction and synthetic spin structure in the superlattice. The synthetic spin structure will be further discussed in Section 3.5.2.

3.3. Tunable Ferromagnetism

Superlattice design provides unprecedented tunability of spin ordering in $\rm SrRuO_3$ layers. This Section discusses various magnetic and magnetotransport behaviors in $\rm SrRuO_3$ based superlattices. We also introduce unconventional magnetic interactions across the heterointerface and/or between $\rm SrRuO_3$ layers within the superlattices. This summary can inspire the design of correlated magnetic superlattices for future spintronic applications by tuning ferromagnetic coercivity, remnant magnetization, spin–orbit coupling, and magnetotransport properties. In particular, spintronic applications may include magnetoresistive memories, magnetic racetracks, spin–orbit torque memories, and current-induced magnetization switching devices. $^{[60,175,176]}$

3.3.1. Structural Modulation of Ferromagnetic Order

Owing to the finite spin-orbit interaction, the global and local structural modifications of the SrRuO3 layer lead to tunable anisotropic ferromagnetic properties, including saturation magnetization, coercive field, and magnetotransport behaviors. For example, Jeong et al. examined the crystalline symmetrydependent spin state of a SrRuO3/SrTiO3 superlattice via atomic-scale thickness control of the SrTiO_3 layers. $^{[91]}$ As the orthorhombic distortion of the SrRuO3 layer evolves toward tetragonal symmetry, the crystal field splitting between the d_{xy} and $d_{xz,yz}$ orbitals is enhanced, resulting in a reduction in saturation magnetization. This is schematically shown in the left panel of Figure 7a. X-ray abortion spectroscopy with linear dichroism demonstrated the enhancement of the unoccupied state at d_{xv} orbitals of the tetragonal SrRuO3/SrTiO3 superlattice (right panel of Figure 7a), experimentally supporting this argument. Figure 7b shows the structural dependence of magnetization as a function of the magnetic field for the orthorhombic and tetragonal SrRuO₃/SrTiO₃ superlattices. The magnetic coercive field significantly increased for the tetragonal superlattices compared with the orthorhombic ones. Lin et al. consistently demonstrated that SrCuO₂/SrRuO₃/SrCuO₂ heterostructures exhibit structure-dependent magnetic hysteresis behavior via dimensionality control of infinite-layer-SrCuO₂ (Figure 7c).^[117]

Magnetotransport measurements also reveal the structural modulation of the ferromagnetic behavior. Evidently, the magnetotransport signal originates predominantly from the metallic SrRuO₃ layer when the partner layer of the superlattice is insulating. Figure 7d shows the magnetic field-dependent magnetoresistance (left panel) and anomalous Hall effect (right panel) of the SrRuO₃/SrTiO₃ superlattices, confirming the structural evolution of the magnetic coercive field depending on the SrTiO3 layer thickness.[89] Furthermore, an anomalous Hall signal contains contributions from topological spin dynamics. Chen et al. theoretically suggested the existence of Weyl nodes in ferromagnetic SrRuO₃, inspired by the observation of nonmonotonic temperature dependence of anomalous Hall signal and magnetization. These observations suggest a finite Berry curvature in the SrRuO3. [177] Itoh et al. measured the temperaturedependent spin-wave gap using neutron diffraction, exhibiting identical nonmonotonic temperature dependence. This further supports the presence of Weyl Fermions along with spin-wave excitation.^[81] Based on these studies, Jeong et al. showed that the size of the spin-wave gap could be further enhanced by using a tetragonal SrRuO3 layer, induced by the modulated magnetic anisotropy in superlattices (Figure 7e).[89] Figure 7f shows the temperature-dependent anomalous Hall resistivity of the SrRuO₃/Pr_{0.7}Ca_{0.3}MnO₃ superlattice.^[141] Whereas the anomalous Hall signals of orthorhombic SrRuO3 single films (green and yellow lines) and SrRuO3/SrTiO3 superlattices (red and blue lines) were negative at low temperatures, the tetragonal SrRuO₃/Pr_{0.7}Ca_{0.3}MnO₃ superlattice (navy line) exhibited a positive sign. Ziese et al. performed angle-dependent magnetoresistance measurements, as shown in Figure 7g.[138] The experimental results for orthorhombic (left panel of Figure 7g) and tetragonal (right panel of Figure 7g) superlattices show good agreement with the fitting results, thus representing the structural dependence of the magnetotransport behavior. Cui et al. reported that the angle-dependent magnetoresistance of SrRuO₃/SrTiO₃ superlattices changes from twofold to fourfold perpendicular symmetry with increasing SrTiO₃ layer thickness owing to structural modifications (Figure 7h).[107]

3.3.2. Interfacial and Interlayer Exchange Coupling

Interfacial exchange coupling of the $SrRuO_3$ layer with different magnetic compounds and/or interlayer exchange coupling between the $SrRuO_3$ layers within superlattices leads to an intriguing correlated magnetic order with functionalities. Qu et al. showed the reorientation of lateral magnetic anisotropy in $SrRuO_3/La_{0.67}Ca_{0.33}MnO_3$ superlattices, as shown in **Figure 8a.** [145] The magnetic field-dependent magnetization curves of the superlattices exhibited a rotation of the magnetic easy axis from the orthorhombic [010] to [100] axis with increasing repetition number of the superlattices. By performing X-ray

1616928.2023, 38, Downloaded from https://onlinelibrary.wiley.com/doi/10.1002/adfm.2023/170 by University Of Temessee Gas, Wiley Online Library of 14/04/2024]. See the Terms and Conditions (https://onlinelibrary.wiley.com/terms-and-conditions) on Wiley Online Library of rules of use; OA articles are governed by the applicable Creative Commons Interps://onlinelibrary.wiley.com/terms-and-conditions) on Wiley Online Library.

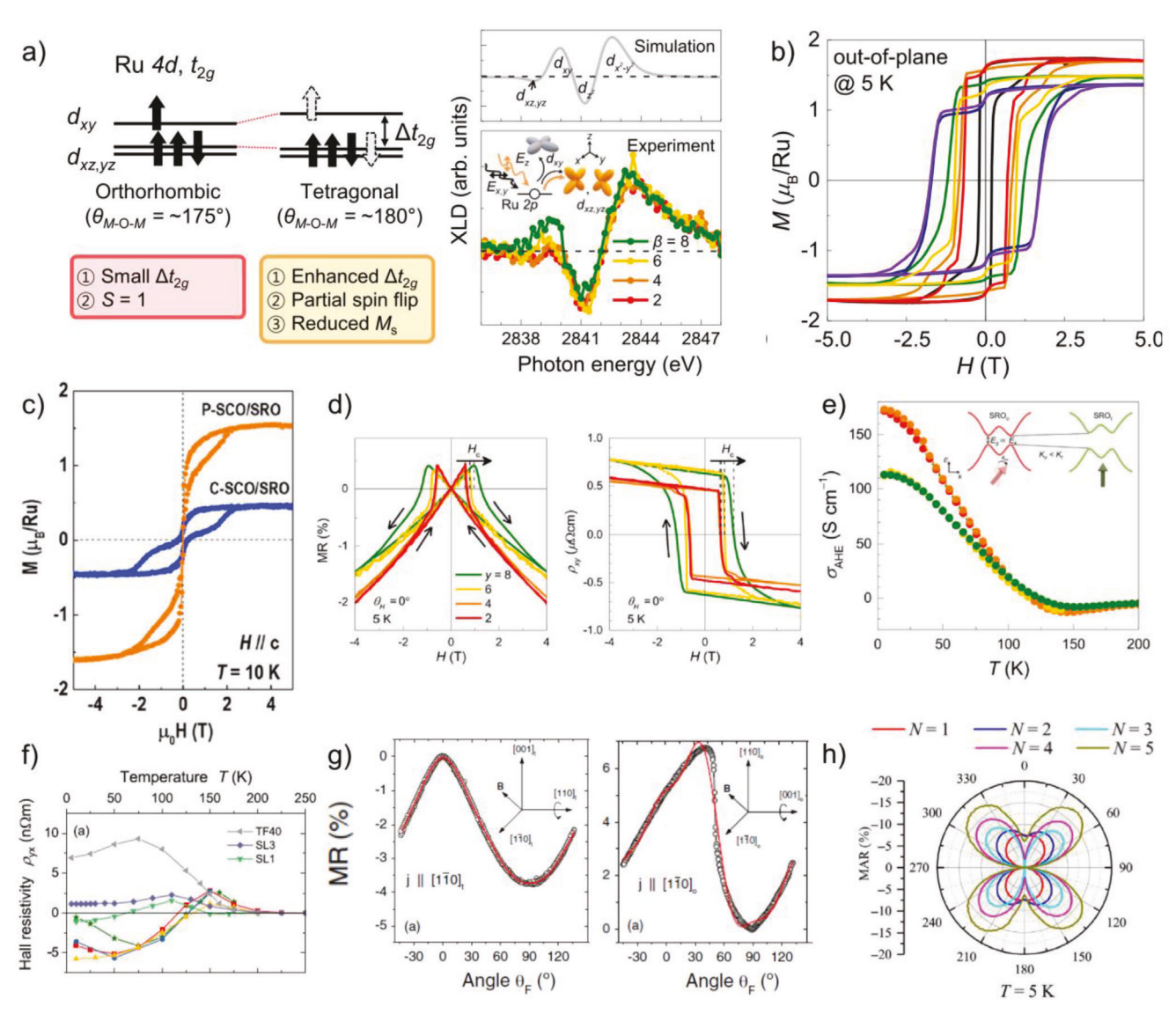


Figure 7. a) Orbital energy splitting difference between orthorhombic and tetragonal SrRuO₃ where the solid (white) arrow is fully (partially) occupied spin states and change of X-ray linear dichroism signal at Ru *L*-edge as SrTiO₃ thickness in SrRuO₃/SrTiO₃ superlattices changes. Reproduced with permission. [91] Copyright 2020, Wiley-VCH GmbH. b) Systematic change of saturation magnetization with structural phase transition of SrRuO₃/SrTiO₃ superlattice between orthorhombic and tetragonal, black, red, orange, yellow, green, blue, and purple are SrRuO₃ thin film and [6| β] superlattice with β = 2, 4, 6, 8, 10, 18, and 24, respectively. Reproduced with permission. [91] Copyright 2020, Wiley-VCH GmbH. c) Structural dependence of magnetic field-dependent magnetization of SrCuO₂/SrRuO₃/SrCuO₂ heterostructure with respect to the SrCuO₂ layer thickness, P-SCO and C-SCO mean planar-type and chain-type structure SrCuO₂, respectively. Reproduced with permission. [117] Copyright 2021, American Chemical Society. d) Magnetoresistance and anomalous Hall effect in SrRuO₃/SrTiO₃ superlattices, $\theta_{\rm H}$ is angle of H-field from the film normal direction. Reproduced with permission. [89] Copyright 2021, American Chemical Society. e) Temperature-dependent anomalous Hall conductivity $\sigma_{\rm AHE}$ of SrRuO₃ in orthorhombic and tetragonal structure, inset is bandgap change with respect to structure change. Reproduced with permission. [89] Copyright 2021, American Chemical Society. f) Temperature, inset is bandgap change with respect to structure change. Reproduced with permission. [89] Copyright 2021, American Chemical Society. f) Temperature, inset is bandgap change with respect to structure change. Reproduced with permission. [89] Copyright 2021, American Chemical Society. f) Temperature, inset is bandgap change with respect to structure change. Reproduced with permission. [89] Copyright 2021, Dop Publishing. g) Magnetic field angle $\theta_{\rm F}$ -dependent magnetoresistance measurement of orthorhom

absorption spectroscopy and structural characterizations, the combination of epitaxial strain and interfacial coupling was suggested to be the origin of magnetic easy axis modulation. On the other hand, the exchange interaction across the interface of ferromagnetic SrRuO₃ and antiferromagnetic layers frequently

revealed an exchange bias effect, characterized by the shift of the magnetic hysteresis loop. Padhan and Prellier reported a large difference between the field-cooled and zero-field-cooled magnetic hysteresis loops and anisotropic behavior depending on the magnetic field direction for SrRuO₃/SrMnO₃ superlattices

Adv. Funct. Mater. 2023, 33, 2301770

16163028, 2023, 38, Downloaded from https://onlinelibrary.wiley.com/doi/10.1002/adfm.202301770 by University Of Temnessee Gsm, Wiley Online Library on [14/04/2024]. See the Terms and Conditions (https://onlinelibrary.wiley.com/tems/

ditions) on Wiley Online Library for rules of use; OA articles are governed by the applicable Creative Commons License

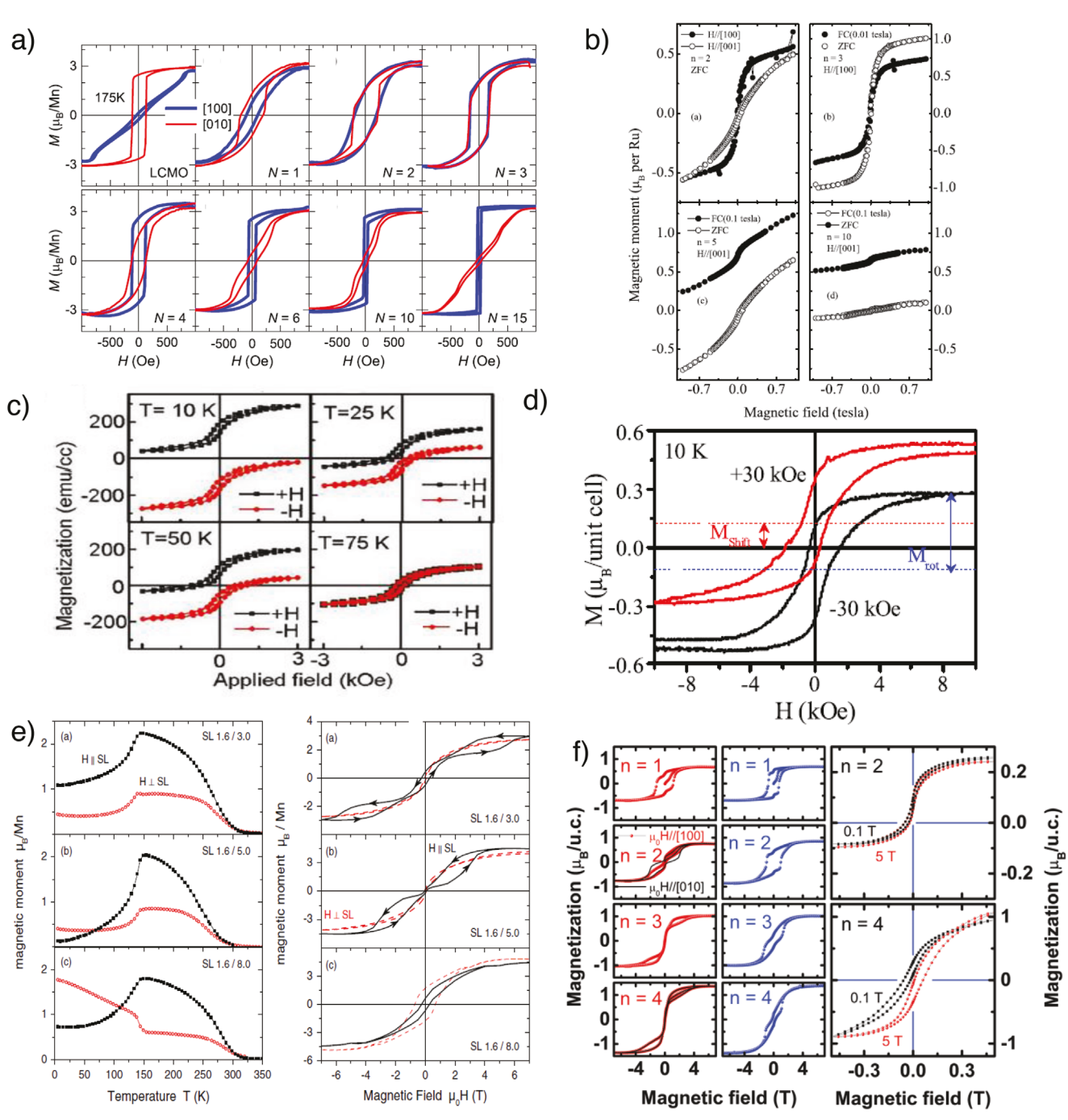


Figure 8. a) Repetition number *N*-dependent lateral magnetic anisotropy of SrRuO₃/La_{0.67}Ca_{0.33}MnO₃ superlattices with the same supercell. Reproduced with permission. Operation and cooling method of SrRuO₃/SrMnO₃ superlattices. Reproduced with permission. Operature dependence of exchange bias effect, splitting of the magnetization loop in SrRuO₃/LaNiO₃ superlattices. Reproduced with permission. Operature dependence of exchange bias effect, splitting of the magnetization loop in SrRuO₃/LaNiO₃ superlattices. Reproduced with permission. Operature dependence of magnetic moment for the three different SrRuO₃/La_{0.7}Sr_{0.3}MnO₃ superlattices with different SrRuO₃ thickness regarding out-of-plane (red circles) and in-plane (black squares) magnetic moment measured by field cooled method. Right panel, magnetic field dependent magnetic moment of the three different SrRuO₃/La_{0.7}Sr_{0.3}MnO₃ superlattices. Reproduced with permission. Operation of SrRuO₃ thickness of the three different SrRuO₃/La_{0.7}Sr_{0.3}MnO₃ superlattice. Reproduced with permission. Operation of SrRuO₃ thickness. The red and blue curves are zero field-cooled in-plane and out-of-plane magnetization, respectively. The right panel is field-cooled in-plane magnetic hysteresis. Reproduced with permission. Operation of SrRuO₃ Wiley-VCH GmbH.

16163028, 2023, 3.8, Downloaded from https://onlinelibrary.wiley.com/doi/10.1002/adfm.202301770 by University Of Temnessee Gsm, Wiley Online Library on [14/04/2024]. See the Terms and Conditions (https://onlinelibrary.wiley.com/terms-and-conditions) on Wiley Online Library for rules of use; OA articles are governed by the applicable Creative Commons Licenses

ADVANCED FUNCTIONAL MATERIALS

with different SrMnO₃ layer thicknesses (Figure 8b).^[151] Here, anisotropic interfacial coupling was demonstrated between the biasing moments of the ferromagnetic SrRuO₂ layer and pinning moments of the antiferromagnetic SrMnO₂ layer within the superlattices. Figure 8c shows the temperature-dependent exchange bias in the SrRuO3/LaNiO3 superlattices investigated by Liu and Ning.[157] The appearance temperature of the magnetic bias effect is defined, which is much lower than the magnetic transition temperature of SrRuO₃. Singh and Chen reported a vertical shift of the hysteresis loop in SrRuO₃/BiFeO₃ superlattices, as shown in Figure 8d.[159] This shift was attributed to pinned Ru4+ moments at the interface and local defects in the SrRuO₃ layer. Ziese et al. reported antiferromagnetic interlayer coupling in SrRuO₃/La_{0.7}Sr_{0.3}MnO₃ superlattices.^[136] The left panel of Figure 8e shows the out-of-plane (circles) and in-plane (squares) magnetic moments as functions of temperature. By varying the SrRuO₃ layer thickness, a change in the magnetization below the ferromagnetic transition temperature of SrRuO₃ was evident, thus indicating an interlayer-coupled spin order. The magnetic-field-dependent magnetization curves in the right panel of Figure 8e support the SrRuO3 thicknessdependent interlayer coupling in the SrRuO₃/La_{0.7}Sr_{0.3}MnO₃ superlattices. Sahoo et al. also studied interlayer exchange coupling in SrRuO₃/PrMnO₃ superlattices.^[147] This superlattice is composed of two ferromagnets in which the two layers exchange couples. As an example, Figure 8f shows the modulated magnetic field-dependent magnetization curves of the superlattice as a function of the PrMnO3 thickness, indicating the interlayer coupling. More recently, Jeong et al. suggested unconventional interlayer exchange coupling and resultant synthetic spin structures via chiral phonons in SrRuO₃/SrTiO₃ superlattices.[55]

3.4. Dimensionality-Induced Phase Transition

Dimensional crossover with an electromagnetic phase transition is a key concept for realizing and understanding the lowdimensional correlated functionality of SrRuO₃ heterostructures. In this section, we introduce the atomic-scale modulation of electronic ground states, which are strongly coupled to the magnetic ground state in SrRuO₃ based superlattices. As the dimensionality of SrRuO₂ decreases, the ferromagnetic metallic ground state in the bulk becomes unstable, which is indicative of an intriguing dimensional crossover. Innovation in atomicscale epitaxy and microscopy techniques has opened a pathway for investigating the monolayer limit of SrRuO₃ heterostructures. In particular, one advantage of periodic superlattice structures is that they provide measurable experimental signals of monolayer SrRuO3 with tunable functionality compared with SrRuO₃ single films. We also summarize the recent debate on the magnetic and transport behavior of monolayer SrRuO₃ within superlattices.

3.4.1. Atomic Scale Control of Electronic Ground State Coupled Magnetic Behavior

Ueda et al. examined the magnetic and electrical transport properties of SrRuO₃/BaTiO₃ superlattices grown on SrTiO₃ (110)

substrates with various stacking periodicities.[111] As the periodicity of the superlattice decreases, the temperature-dependent resistivity exhibits an electrical phase transition from metal to insulator owing to the reduced dimensionality of the SrRuO₂ layer (top panel of Figure 9a). The magnetization versus temperature curves in the bottom panel of Figure 9a shows a concomitant decrease of magnetization and ferromagnetic transition temperature with decreasing periodicity. The inset of Figure 9a further signifies the antiferromagnetic-like behavior of the superlattice consisting of two unit cell layers of SrRuO3 and five unit cell layers of BaTiO3, similar to layered ruthenates. Liu et al. reported that SrRuO₃/LaAlO₃ superlattices with varying SrRuO₃ layer thicknesses preserved the ferromagnetic behavior down to two unit cell layers of the SrRuO3 with a ferromagnetic transition temperature of 110 K (Figure 9b). [116] Izumi et al. demonstrated SrRuO3 thickness-dependent ferromagnetic behavior observed by temperature-dependent magnetization measurement in Figure 9c, in SrRuO₃/SrTiO₃ superlattices.^[86,87] As the SrRuO₃ layer thickness decreased, the magnetic transition temperature systematically decreased to 60 K for the two unit cell layers of SrRuO₃ within the superlattice. The monolayer SrRuO₃ did not exhibit magnetic transition down to 2 K. Temperaturedependent resistivity curves of the SrRuO₃/SrTiO₃ superlattice consistently exhibited a decrease in temperature with maximum magnetoresistivity related to the ferromagnetic transition temperature, with decreasing SrRuO₃ layer thickness (Figure 9d). In particular, a monolayer SrRuO₃ superlattice with five unit cell layers of SrTiO3 showed insulating temperature dependence in the absence of ferromagnetic transitions. More recently, consistent demonstration of dimensional crossover in both electronic and magnetic phase transitions for atomically thin SrRuO3 layers within SrRuO₃/SrTiO₃ superlattices was reported.^[92] A clear distinction between the metallic and insulating phases was also observed from temperature-dependent thermopower measurements. Suppression of the electronic charge carriers in the monolayer SrRuO3 superlattice induced a large enhancement in the thermopower at low temperatures. Furthermore, a phase instability at the border of the dimensional crossover, i.e., at the two unit cell layers of SrRuO3, with a temperature-dependent metalinsulator transition along with a metamagnetic transition, was observed. Notably, distinct partner oxide layers of two unit cell SrRuO₃ superlattices exhibit exotic magnetic behavior with transition temperature, thus indicating the tunable magnetic functionality of the low-dimensional SrRuO₃ superlattices. Figure 9fi further show the dimensionality-induced electronic phase transition of the SrRuO₃/SrTiO₃ superlattices with strongly coupled magnetic phase transitions. [54,98,100] Numerous experiments by different research groups consistently demonstrated the presence of electromagnetic phase transition across the dimensional crossover in the SrRuO3 layers. On the other hand, typical residual resistance ratios of SrRuO3 based superlattices range from 0.1 to 8 for SrRuO₃/SrTiO₃ superlattice and around 1 for SrRuO₃/BaTiO₃ superlattice and SrRuO₃/LaAlO₃ superlattice. It should be noted that most superlattice studies have focused on the properties of the SrRuO3 layer with only a few atomic layers thickness, where metal-insulator transitions are frequently observed. Furthermore, when a superlattice is composed of a metallic partner layer, it is difficult to determine the electrical transport properties of SrRuO₃. Therefore, in most cases, the discussion

16163028, 2023, 38, Downloaded from https://onlinelibrary.wiley.com/doi/10.1002/adfm.202301770 by University Of Temnes

ee Gsm, Wiley Online Library on [14/04/2024]. See the Terms

) on Wiley Online Library for rules of use; OA articles are governed by the applicable Creative Commons License

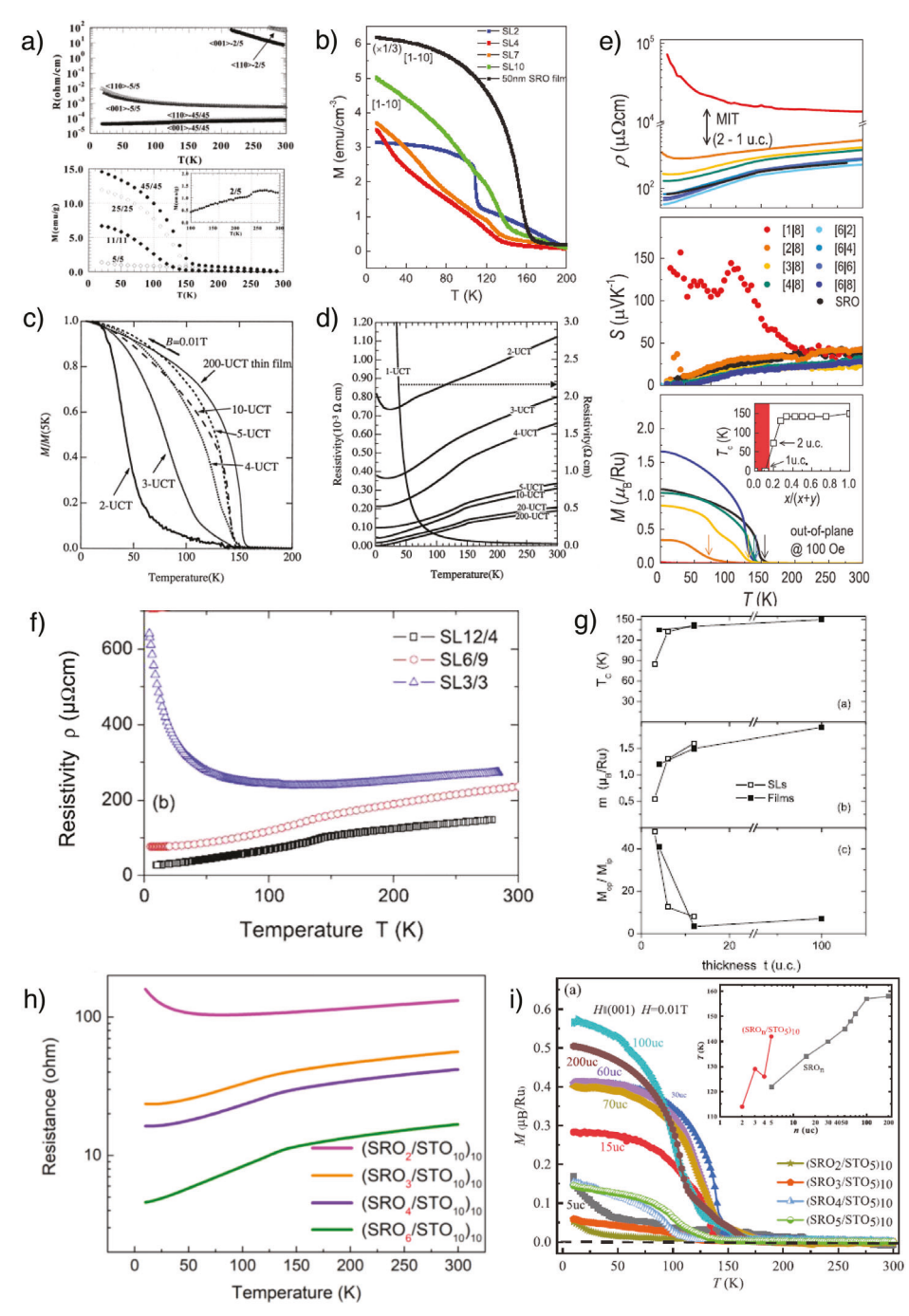


Figure 9. a) Temperature-dependent transport and magnetization with respect to stacking periodicity of SrRuO₃/BaTiO₃ superlattice grown on SrTiO₃ (001) and (110) substrates. Reproduced with permission. [111] Copyright 2000, Elsevier. b) Temperature-dependent magnetization of SrRuO₃/LaAlO₃ superlattices with varying SrRuO₃ layer thickness, SL(n) means [(SrRuO₃)n/(LaAlO₃)n] superlattice with same thickness ≈100 nm. Reproduced with permission. [116] Copyright 2012, AIP Publishing. c) Temperature-dependent magnetization of SrRuO₃/SrTiO₃ superlattices with varying SrRuO₃ thickness. Reproduced with permission. [87] Copyright 1998, Elsevier. d) Temperature-dependent transport of SrRuO₃/SrTiO₃ superlattices with different SrRuO₃ thickness. Reproduced with permission. [86] Copyright 1998, The Physical Society of Japan. e) Dimensional crossover effect of SrRuO₃/SrTiO₃ superlattice as a function of SrRuO₃ thickness, resistivity, Seebeck coefficient, and magnetization evolve with respect to both SrRuO₃ and SrRuO₃ thickness. The plots show metal-insulator transition between [1|8] and [2|8] superlattices. Reproduced with permission. [92] Copyright 2020, American Physical Society. f) Temperature-dependent resistivity and g) Summarized magnetic properties, magnetic transition temperature, saturation magnetization at magnetization ratio between out-of-plane and in-plane, of three different SrRuO₃/SrTiO₃ superlattices, repetition number of the three superlattices are same as 15. Reproduced with permission. [100] Copyright 2013, IOP Publishing. h) Temperature-dependent resistance of SrRuO₃/SrTiO₃ superlattices with varying SrRuO₃ layer thickness. Reproduced with permission. [98] Copyright 2020, American Physical Society. i) Temperature-dependent magnetization of SrRuO₃ thin films and SrRuO₃/SrTiO₃ superlattices as a function of SrRuO₃ thickness. Reproduced with permission. [54] Copyright 2022, Wiley-VCH GmbH.

16163028, 2023, 38, Downloaded from https://onlinelibrary.wiley.com/doi/10.1002/adfm.202301770 by University Of Tennessee Gsm, Wiley Online Library on [14/04/2024]. See the Terms and Conditions (https://onlinelibrary.wiley.com/terms

-and-conditions) on Wiley Online Library for rules of use; OA articles are governed by the applicable Creative Commons License

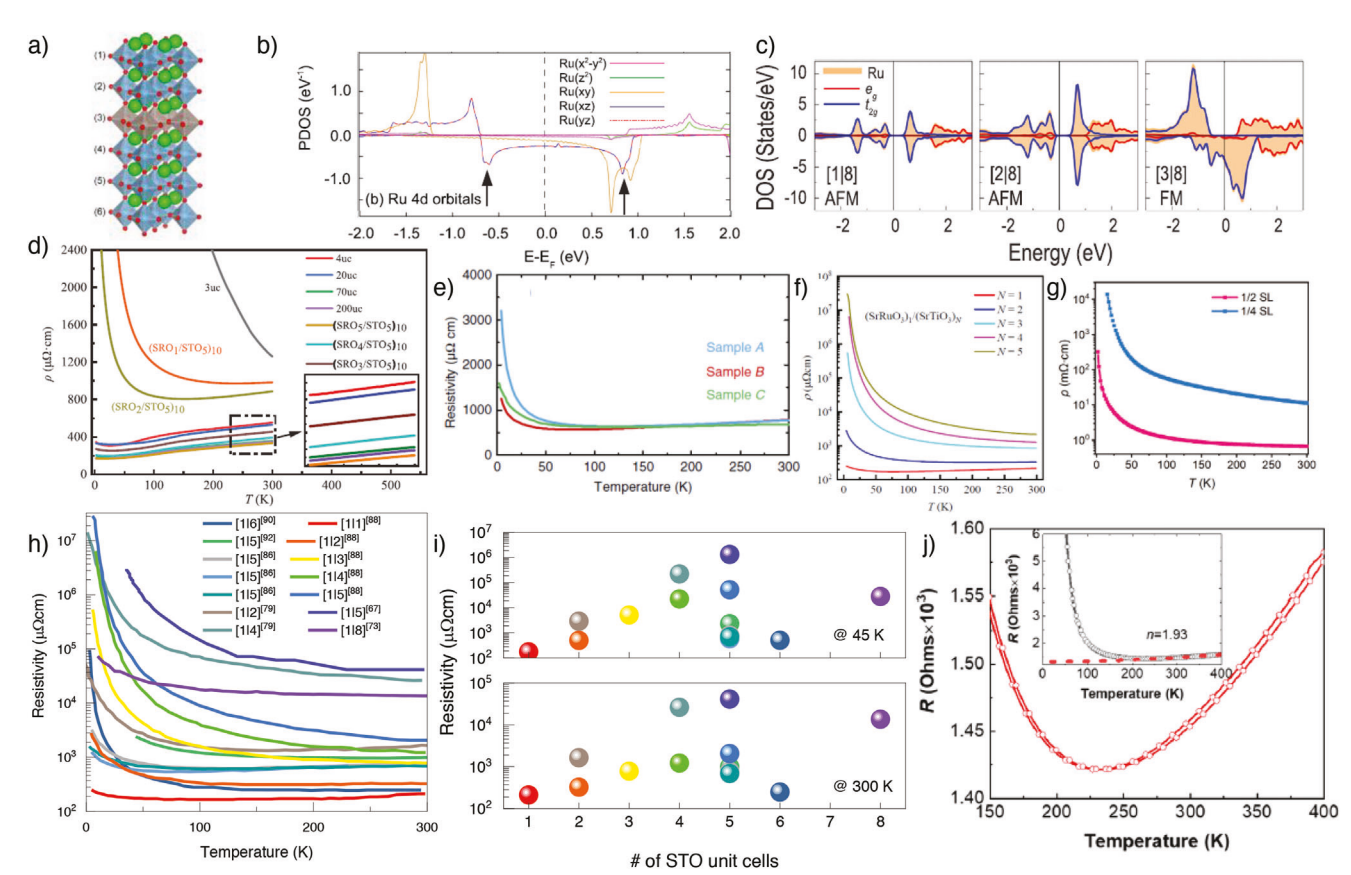


Figure 10. a) Schematic and b) projected density of states of Ru orbitals of oxide superlattice composed monolayer SrRuO₃ layer and 5 unit cell layers of SrTiO₃. Reproduced with permission. [102] Copyright 2012, American Physical Society. c) Dimensionality-induced phase transition of SrRuO₃/SrTiO₃ superlattice as a function of the thickness of the SrRuO₃ layer. Reproduced with permission. [102] Copyright 2020, American Physical Society. d) Temperature-dependent transport of SrRuO₃ thin films and SrRuO₃/SrTiO₃ superlattice with varying SrRuO₃ layer thickness. Reproduced with permission. [104] Copyright 2022, Wiley-VCH GmbH. e) Temperature-dependent transport of three monolayer SrRuO₃ superlattices, both sample A and B are [115]₂₀, and sample C is [1120]₁. Reproduced with permission. [105] Copyright 2019, American Physical Society. f) Temperature-dependent resistivity of SrRuO₃/SrTiO₃ superlattice with varying SrTiO₃ thickness. Reproduced with permission. [107] Copyright 2020, American Association for the Advancement of Science. g) Temperature-dependent transport of SrRuO₃/SrTiO₃ superlattice with two different SrTiO₃ thickness. Reproduced with permission. [105] Copyright 2022, Springer Nature. h) Summary of the temperature-dependent resistivity of SrRuO₃ superlattice at 45 K and 300 K. The colors in the figure correspond to the labeling of Figure 10h. j) Temperature-dependent transport of monolayer SrRuO₃ superlattice with 10 unit cell layers of BaTiO₃, red dashed line in the inset is fitting curve using parallel resister formula. Reproduced with permission. [112] Copyright 2020, American Chemical Society.

of impurities and other crystallographic defects in the material through residual resistance ratio values of $SrRuO_3$ superlattices is limited.

3.4.2. Debate on Monolayer SrRuO₃ within Superlattices

The monolayer limit of $SrRuO_3$ has tremendous potential for achieving a novel low-dimensional ground state in the electronic, magnetic, and topological states. Verissimo-Alves et al. theoretically proposed a spin-polarized 2D electron gas in a $SrRuO_3/SrTiO_3$ superlattice composed of a monolayer of $SrRuO_3$ and five unit cell layers of $SrTiO_3$, as schematically illustrated in **Figure 10a**. [102] The authors used local spin density approximation methods with an effective on-site Coulomb interaction of 4.0 eV for the Ru-d orbitals. Figure 10b shows the typical double peak feature of the Ru-d_{xz,yz} states (marked by arrows) that are similar to those frequently observed in 1D metallic systems, rep-

resenting the low-dimensional electronic structure of the monolayer SrRuO3 superlattice. Jeong et al. demonstrated the systematic evolution of the dimensionality-induced metal-insulator transition coupled with the magnetic phase transition using the generalized gradient approximation method (Figure 10c).[92] Whereas the trilayer SrRuO₃ superlattice preserved the ferromagnetic metallic state similar to that of the bulk, the ground states of the monolayer and bilayer SrRuO3 superlattices were antiferromagnetic insulating states with a finite bandgap between the d_{xy} and $d_{yz,zx}$ orbitals of the Ru- t_{2g} states. Thus, they suggested that anisotropic hybridization of the Ru- $t_{2\alpha}$ orbitals caused dimensionality-induced concomitant magnetic and electronic phase transitions in the atomically thin SrRuO3 superlattices. It was further mentioned that the on-site Coulomb interaction value is important for theoretically reproducing the experimentally observed electromagnetic phase of low-dimensional SrRuO₃ systems.



www.advancedsciencenews.com



www.afm-journal.de

The experimental realization and characterization of SrRuO₃ monolayers have received considerable attention. Compared with single film, monolayer SrRuO₂ superlattices have a structural advantage in terms of accessible experimental signals required to explore the low-dimensional SrRuO3 layers. Figure 10d shows the clear insulating behavior of the monolayer SrRuO3 superlattice, characterized by Deng et al.^[54] Note that the resistivity value was much lower compared with that for the SrRuO₃ single film of three atomic unit cell thickness, in which the thinner films could not be measured.[178] The superlattices were also beneficial for preserving the layer-by-layer growth of the SrRuO3 layer by controlling laser fluence of pulsed laser epitaxy,[54] with minimized surface depletion effect. However, we also note that the quantitative resistivity values of monolayer SrRuO₃ superlattices reported by different groups show considerable differences, suggesting the highly sensitive electrical transport behavior of these superlattices within different dielectric environments mostly provided by the neighboring SrTiO₃ layers. Boschker et al. reported monolayer SrRuO3/SrTiO3 superlattices with five unit cell layers of SrTiO₃. [105] Figure 10e shows the temperature-dependent resistivity of three different superlattices with the same periodicity, revealing diverse resistivity values, particularly at low temperatures. Figure 10f,g consistently show the clear insulating behavior of the monolayer SrRuO₃ in other SrRuO₃/SrTiO₃ superlattices, where the resistivity significantly increases with the thickness of the SrTiO3 layer, as observed by two different groups.[99,107]

To confirm the effect of the thickness of the SrTiO₃ layer in the monolayer SrRuO3 superlattices, we summarized the reported temperature-dependent resistivity of the SrRuO₃ monolayer within different SrRuO₃/SrTiO₃ superlattices (Figure 10h,i).[86,92,99,105,107,109] Figure 10h shows a large variation in the experimental observations from different groups for monolayer SrRuO3 superlattices depending on the thickness of the SrTiO₃ layer. The resistivity values extracted at 40 and 300 K as a function of SrTiO₃ layer thickness are shown in Figure 10i. Evidently, most monolayer SrRuO₃ superlattices exhibited increased resistivity as the SrTiO3 layer thickness increased at both the selected temperatures. This simple analysis indicates a viable interlayer electronic coupling between the SrRuO3 monolayers through an atomically thin SrTiO₃ layer, thus determining the electronic state of the monolayer SrRuO₃ superlattices. However, so far, experimental studies on SrRuO₃ monolayer superlattices are limited on electrical transport measurements. We hope that future studies will further investigate how the interlayer coupling between the SrRuO₃ monolayers could determine the magnetic ground state associated with, e.g., the metal-insulator transition. On the other hand, most studies so far have been limited to SrRuO₃/SrTiO₃ superlattices, where charge transfer at the interface is highly suppressed.^[92] The suppression of charge transfer at the SrRuO₃/SrTiO₃ interface has been predicted theoretically by Zhong and Hansmann, in which the energy level of oxygen ions at the interface has been aligned to predict the difference in work function or electron affinity.[179] SrRuO3 and SrTiO₃ happen to have similar energy levels of oxygen p-orbital state with respect to the Fermi energy. This result suggests that different partner layers other than the SrTiO₂ layer might lead to non-zero charge transfer at the interface, thereby resulting in novel electronic phases in the monolayer SrRuO₃ superlattices.

Figure 10j shows the temperature-dependent resistivity curves of superlattices with monolayer $\rm SrRuO_3$ and 10 unit cell layers of $\rm BaTiO_3$, which is more metallic than the more extensively studied $\rm SrRuO_3/SrTiO_3$ superlattices. $^{[112]}$ This experimental observation implies that more intriguing physics potentially related to charge transfer might further be hidden in the monolayer $\rm SrRuO_3$ superlattices.

3.5. Synthetic Spin Structures

Owing to the strongly correlated electrons and a considerable spin—orbit interaction, SrRuO₃ based superlattices have introduced various novel synthetic spin structures. In this Section, we discuss synthetic spin structures via spin—phonon coupling and topologically nontrivial spin textures observed and manipulated in SrRuO₃ based superlattices.

3.5.1. Spin-Phonon Coupling-Induced Synthetic Spin Structures

As mentioned in Section 3.3.2, ferromagnetic SrRuO₃ is known to have strong spin-phonon coupling, which has been experimentally validated for both single films and superlattices. Based on the strong spin-phonon coupling, the existence of chiral phonons in the SrRuO₃/SrTiO₃ superlattice was proposed based on the observation of the phonon Zeeman effect.^[55] Chiral symmetry breaking of phonons induces emergent quantum magnetic phenomena such as the phonon Hall effect,[180] optically driven effective magnetic field, [181] AC Stark effect, [182] topologically induced viscosity split,[183] and pseudogap phases.[184] Jeong et al. introduced a chiral phonon-induced interlayer exchange interaction between ferromagnetic SrRuO3 and the resultant synthetic spin structures in SrRuO₃/SrTiO₃ superlattices (Figure 11a). The left panel of Figure 11a shows the unexpected oscillatory behavior of in-plane magnetization as a function of the SrTiO₃ layer thickness in the SrRuO₃/SrTiO₃ superlattices. The noncollinear spiral spin state observed from the polarized neutron reflectivity was suggested to be responsible for the observed magnetic oscillation (middle and right panels of Figure 11a), thus suggesting the presence of interlayer exchange coupling. As SrTiO₂ is insulating, the conventional Ruderman-Kittel-Kasuva-Yosida interaction cannot explain the observed behavior. Instead, chiral phonons have been proposed as mediating quasi-particles for unconventional interlayer-exchange interactions.

3.5.2. Topologically Nontrivial Synthetic Spin Structures

The strong antiferromagnetic interlayer coupling and/or Dzyaloshinskii–Moriya interactions at the symmetry-broken interfaces of the superlattice can lead to a topologically nontrivial synthetic spin texture, i.e., magnetic skyrmions, in SrRuO₃, envisioning novel spintronic functionalities. Noncollinear spin structures in SrRuO₃ based superlattices are typically manifested by the topological Hall effect in magnetotransport measurements. Vrejoiu and Ziese proposed that strong antiferromagnetic interlayer coupling with different magnetocrystalline anisotropies in SrRuO₃/La_{0.7}Sr_{0.3}MnO₃ superlattices can induce

16163028, 2023, 38, Downloaded from https://onlinelibrary.wiley.com/doi/10.1002/adfm.202301770 by University Of Temessee Gsm, Wiley Online Library on [14/04/2024]. See the Terms and Conditions (https://onlinelibrary.wiley.

ditions) on Wiley Online Library for rules of use; OA articles are governed by the applicable Creative Commons License

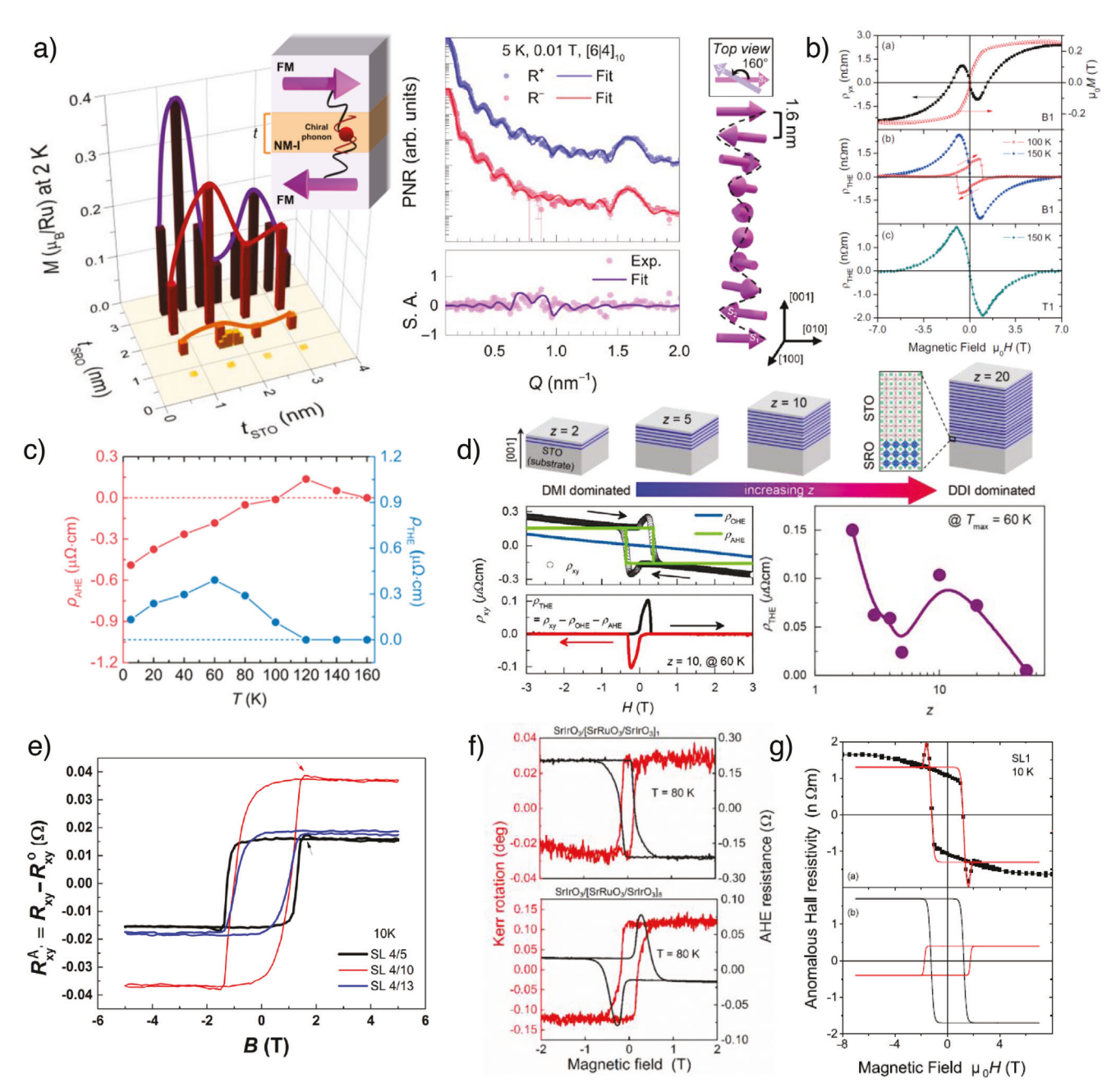


Figure 11. a) In-plane magnetization in SrRuO₃/SrTiO₃ superlattices at 2 K as a function of SrRuO₃ and SrTiO₃ layer thickness (Left panel). Inset is schematic of chiral phonon-induced interlayer magnetic coupling. The middle panel is experimental results of polarized neutron reflectivity (PNR) with spin asymmetry (S.A.) signal (bottom). The right panel is corresponding spin structure of SrRuO₃/SrTiO₃ superlattices. Reproduced with permission. [55] Copyright 2022, American Association for the Advancement of Science. b) Interlayer coupling-induced topological Hall effect in SrRuO₃/La_{0.7}Sr_{0.3}MnO₃ superlattice, B1 and T1 are bilayer of 2 nm La_{0.7}Sr_{0.3}MnO₃ on the 5 nm SrRuO₃ and trilayer of 6 nm SrRuO₃ layer between 2 nm La_{0.7}Sr_{0.3}MnO₃ for both interface, the black rectangle is Hall resistivity and red triangle is magnetization. Reproduced with permission. [122] Copyright 2016, Wiley-VCH GmbH. c) Temperature-dependent anomalous Hall resistivity and topological Hall resistivity in [(SrRuO₃)₉/(BiFeO₃)₁₂]₂ multilayer. Reproduced with permission. [158] Copyright 2022, American Chemical Society. d) Schematic of repetition number dependence of topological Hall effect in SrRuO₃/SrTiO₃ superlattice, Hall resistivity plot, and actual repetition number dependence of topological Hall effect in SrRuO₃/SrTiO₃ Superlattice. Reproduced with permission. [163] Copyright 2021, Elsevier. e) Topological Hall resistance at 10 K of SrRuO₃/SrIO₃ superlattice. Reproduced with permission. [163] Copyright 2017, American Chemical Society. f) Kerr rotation and anomalous Hall resistance with hump structure that is built as SrIrO₃/SrRuO₃/SrIrO₃ trilayers changed to SrRuO₃/SrIrO₃ superlattice. Reproduced with permission. [162] Copyright 2021, American Physical Society. g) Anomalous Hall resistivity with and without hump signal in SrRuO₃/Pr_{0.7}Ca_{0.3}MnO₃ SL1 and SL3 in Figure 7f. Reproduced with permission. [109] Copyright 2019, IOP Publishing.



www.advancedsciencenews.com



www.afm-journal.de

the topological Hall effect, as shown in Figure 11b.[122] In these superlattices, the exchange field was estimated to be in the range of several Teslas. Because the ferromagnetic La_{0,7}Sr_{0,3}MnO₃ layer is comparatively soft, the topological Hall effect can develop in the SrRuO₃ layers. Yao et al. observed a temperaturedependent topological Hall effect in SrRuO₃/BiFeO₃ multilayers originating from the broken inversion symmetry near the interface (Figure 11c).[158] Jeong et al. investigated the tunable topological Hall effect in a SrRuO3/SrTiO3 superlattice by controlling the repetition number of the supercell structures, as shown in Figure 11d.[90] The competition between the Dzyaloshinskii-Moriya and dipole-dipole interactions can be modulated by the repetition number of SrRuO₃/SrTiO₃ superlattices. Using Monte-Carlo simulations, it was shown that the Dzyaloshinskii-Moriya interaction-stabilized Néel-type skyrmions for low-repetition superlattices and dipole-dipole interaction-stabilized Bloch-type skyrmions for high-repetition superlattices were realized. This resulted in a nonmonotonic dependence of the topological Hall signal depending on the repetition number. By adopting a strong spin-orbit coupling of 5d oxides with ferromagnetic SrRuO₃, Pang et al. further reported the interfacial Dzyaloshinskii-Moriya interaction in SrRuO₃/SrIrO₃ superlattices, resulting in a topological Hall effect (arrow in Figure 11e).[163]

It is worth discussing other potential mechanisms of the unconventional Hall signal in SrRuO₃ based heterostructures. Kan et al. suggested that the inhomogeneous magnetoelectric properties of atomically thin SrRuO3 layers induce a topological Halllike hump signal as a function of the magnetic field strength.^[185] Yang et al. reported the absence of the hump-like signal in the Hall resistance loops of SrIrO₃/SrRuO₃/SrIrO₃ trilayers (top panel of Figure 11f), whereas the SrRuO₃/SrIrO₃ superlattices exhibited a hump structure in the magnetic field-dependent Hall measurements (bottom panel of Figure 11f).[162] This result was interpreted as the unavoidable inhomogeneity in the SrRuO₃ layers within the superlattices. Ziese et al. reported that the hump signal of the SrRuO₃/Pr_{0.7}Ca_{0.3}MnO₃ superlattice can be explained by a combination of two different Hall contributions, which have different temperature dependence and opposite Hall sign, as shown in Figure 11g.[138] The structural modification of SrRuO₃/Pr_{0.7}Ca_{0.3}MnO₃ superlattices separates the tetragonal and orthorhombic structures within the SrRuO₃ layers. Based on their structural characterization, they suggested that combining two different magnetic domains from tetragonal and orthorhombic structures, which have opposite Hall signals, could potentially lead to a topological Hall-like hump signal. Clear experimental observations are necessary for a better understanding of the unconventional Hall signal. Several techniques for imaging the topological non-trivial spin textures include magnetic force microscopy, scanning tunneling microscopy, Lorentz transmission electron microscopy, and magnetic X-ray scattering. First, magnetic force microscopy and scanning tunneling microscopy have limitations in observing the spin texture of the inner SrRuO₃ layers in some heterostructures because they use a probe tip. Conventional Lorentz transmission electron microscopy still has limitations in high-magnification measurements at temperatures below 150 K and under a magnetic field of about 1 T. We expect that magnetic X-ray scattering is considered the most realistic method for observing the spin texture of the internal

 $\rm SrRuO_3$ layers while applying an external magnetic field at low temperatures. $^{[186]}$ If changes in the superlattice diffraction peak are observed, distinguishable observations can be obtained due to the significantly larger experimental signal provided by the superlattice peak compared to that of thin single films.

As exemplified by the abovementioned intriguing Hall effect and the potential existence of real-space or reciprocal-space magnetic textures, [74] heterostructures composed of SrIrO₃ and SrRuO₃ have attracted intense attention in the past few years. As this portion of the work has been summarized in detail in a recent review, [187] it is skipped in the current work. It is worthy to note that iridate by itself is another good example showcasing how the intriguing interplay of electron correlation and spin–orbit coupling leads to a rich variety of emergent phenomena. [188–192] In the next Chapter, we will review studies related to iridate based superlattices other than SrIrO₃/SrRuO₃ heterostructures.

4. 5d SrIrO₃ Based Superlattices

 $SrIrO_3$ is the most notable building block for constructing 5d superlattices because of the readily obtained perovskite structure in thin films. 40 nm is believed to be the critical thickness to keep the high quality of perovskite $SrIrO_3$ thin film, above which impurity phases like monoclinic $SrIrO_3$ and Ir-deficiency phases may exist. Nonetheless, it would be helpful to start with the physics related to Sr_2IrO_4 , to better understand the physics of the quasi-isolated square lattice composed of four IrO_6 octahedra, and to better apprehend the motivation for engineering the square lattice in different superlattice structures.

A well-recognized scenario in iridates is that the octahedral crystal field splits the 5d orbitals into $e_{\rm g}$ and $t_{\rm 2g}$ orbitals. The latter entangles with spin, giving rise to a half-filled $J_{\rm eff}=1/2$ doublet on top of a fully occupied $J_{\rm eff}=3/2$ quartet. As a result, although correlation (\approx 2 eV) is much reduced in iridates, it is still strong enough to split the narrow $J_{\rm eff}=1/2$ band (the bandwidth is of about 0.5 eV) into an empty upper Hubbard band (UHB) and a full lower Hubbard band (LHB), leading to a Mott gap of \approx 0.1 eV in the single-layer iridate ${\rm Sr_2IrO_4}$. The Mott physics not only accounts for the insulating behavior of ${\rm Sr_2IrO_4}$ but also renders the square-lattice iridate as another promising candidate for pursuing next-generation high- T_c superconductivity. [196,197]

The $J_{\text{eff}} = 1/2$ state also results in novel magnetic properties. The most essential consequence of the strong spin-orbitentangled state is that simple spin is no longer a good quantum number for describing the electron wave function while the magnetic moments are described within the $J_{\text{eff}} = 1/2$ manifold. [198] Nevertheless, the quasi-isotropic shape of the $J_{\rm eff}=1/2$ state has an equal mixture of d_{xy} , d_{yz} , and d_{zx} orbitals (under cubic crystal symmetry). Thus, the intersite magnetic interaction on a straight bond is necessarily isotropic, i.e., a Heisenberg exchange interaction is obtained, similar to the S = 1/2 sites. This local rotational symmetry thus enables a square lattice of $I_{\text{eff}} = 1/2$ states to capture the rich physics of the 2D Hubbard model and 2D Heisenberg model, as schematically shown in Figure 12. Previous studies on bulk samples have shed light in this direction but only unveiled the tip of the iceberg owing to the limited flexibility in the crystal structure. Table 3 summarizes the reported SrIrO3 based superlattices depending on the functionality of the partner perovskite oxide layer, which fosters the

1616928.2023, 38, Downloaded from https://onlinelibrary.wiley.com/doi/10.1002/adfm.2023/170 by University Of Temessee Gas, Wiley Online Library of 14/04/2024]. See the Terms and Conditions (https://onlinelibrary.wiley.com/terms-and-conditions) on Wiley Online Library of rules of use; OA articles are governed by the applicable Creative Commons Interps://onlinelibrary.wiley.com/terms-and-conditions) on Wiley Online Library.

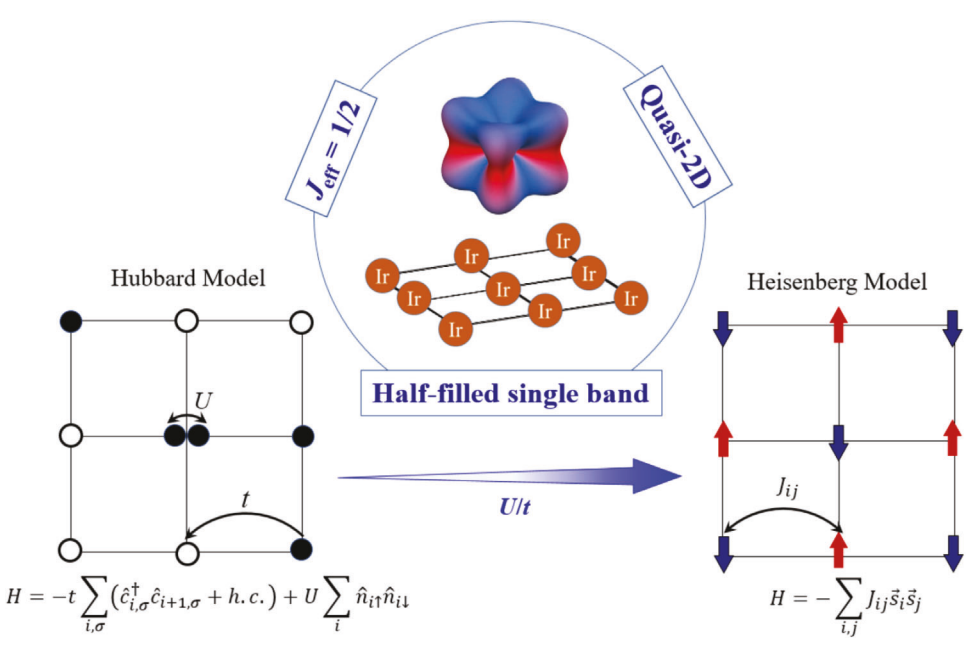


Figure 12. Physics relevant to the 2D square-lattice iridate, ranging from the charge Hubbard model to the spin Heisenberg model.

Table 3. Summary of reported 5d SrIrO₃ based superlattices.^[75,199–218]

5d SrIrO ₃ based superlattices	Functionality of partner compounds	Refs.
SrIrO ₃ /SrTiO ₃	Quantum paraelectric	[75, 199–205]
SrIrO ₃ /CaTiO ₃	Incipient ferroelectric	[206]
$SrIrO_3/La_{1-x}Sr_xMnO_3$	(Anti-)ferromagnetic	[207–211]
SrIrO ₃ /SrMnO ₃		[212]
SrIrO ₃ /LaCoO ₃		[213,214]
SrIrO ₃ /LaFeO ₃		[215]
SrIrO ₃ /LaMnO ₃		[216]
SrIrO ₃ /LaNiO ₃		[217]
SrIrO ₃ /CaMnO ₃		[218]

controllability of emergent correlated behaviors. [75,199–218] Next, we review recent exciting findings on superlattices composed of square-lattice iridates by the extensive control of lattice structure, chemical composition, etc.

4.1. Crystal, Electronic, and Magnetic Structures Manipulation

4.1.1. Manipulating Electronic Properties via Atomic-Scale Precision Control of Crystal Structure

Controllability over crystal structure at the atomic-scale precision is the most prestigious merit of artificial heterostructures, because of which one is able to harness artificial crystals that mimic natural bulk materials. More importantly, one is thus able to create materials that do not have a natural counterpart. Therefore, take iridates for an example, numerous exotic magnetic structures, textures, or domain structures can be obtained through the artificial design thanks to the strong interlock between crystal structure and magnetic structure. From the fun-

damental research point of view, the ability to synthesize a realistic system that is simplified enough to only capture all the necessary ingredients is the key to understand profound theory problems. From the application point of view, designing new magnetic materials on demand of more efficient control and read functionalities is of vital importance for the development of spintronics. Figure 13a shows the representative lattice structure of a (SrIrO₃)1/(SrTiO₃)1 superlattice, where perovskite SrIrO3 and SrTiO3 monolayers are stacked alternately along the c-axis. The most important building block in the superlattice is a square lattice composed of corner-sharing IrO₆ octahedra, whereas the SrTiO₃ spacer is cubic and electronically and magnetically inert. [75,199,219–223] Similar to all other perovskite systems, IrO₆ octahedron may rotate around the c-axis, which is dubbed as octahedral rotation, or rotate around the diagonal direction in the ab-plane leading to an octahedral tilt, as extensively discussed in the previous Chapter for the ruthenate. [224,225] Octahedral rotation and tilt play drastically different roles in determining the local/global crystal symmetry of SrIrO₃. As schematically shown in Figure 13b, for a square lattice with a staggered octahedral rotation pattern, the global rotational symmetry is the same as that without rotation.^[226] By contrast, the octahedral tilt breaks not only the local inversion symmetry but also the global rotational symmetry (Figure 13c).

Matsuno et al. synthesized a series of (SrIrO₃) $n/(\text{SrTiO}_3)1$ superlattices with n values ranging from 1 to $4.^{[75]}$ Electrical transport measurements suggest that (SrIrO₃) $3/(\text{SrTiO}_3)1$ is at the boundary between the semimetallic phase and the Mott insulating phase. All the superlattices feature a half-filled $J_{\text{eff}}=1/2$ state thanks to the absence of interfacial charge transfer between Ir and Ti. The degradation of the insulating state with increasing n indicates that the electron correlation was successively suppressed due to the increasing SrIrO₃ spacer thickness. This control of quantum confinement was later confirmed by Kim et al., based on density functional theory calculations. The study found

16163028, 2023, 38, Downloaded from https://onlinelibrary.wiley.com/doi/10.1002/adfin.202301770 by University Of Temessee Gas, Wiley Online Library on [14/04/2024]. See the Terms and Conditions (https://onlinelibrary.wiley.com/terms-and-conditions) on Wiley Online Library on [14/04/2024]. See the Terms and Conditions (https://onlinelibrary.wiley.com/terms-and-conditions) on Wiley Online Library for rules of use; OA articles are governed by the applicable Creative Commons I

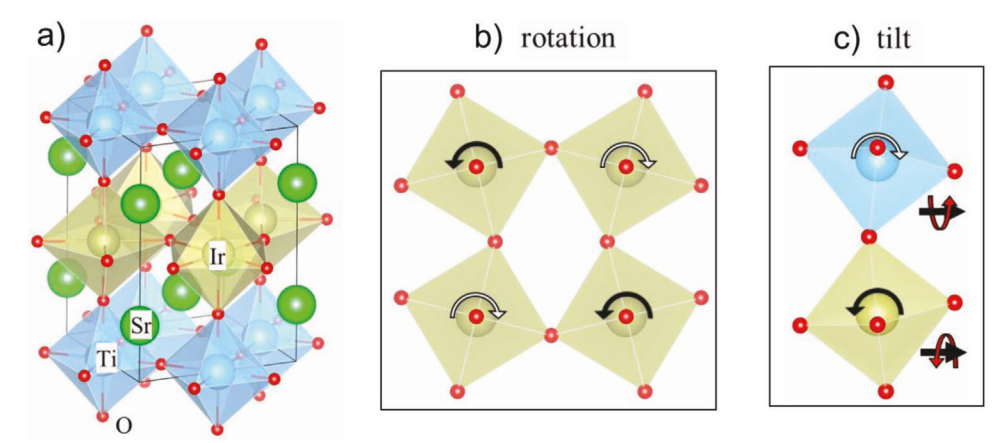


Figure 13. a) Lattice structure of (SrIrO₃) 1/(SrTiO₃) 1. Schematics of b) octahedral rotation and c) tilt.

that the vertical charge hopping within the multiple-layer SrIrO₃ spacer increased the $J_{\text{eff}} = 1/2$ bandwidth, which in turn reduced the effective electron correlation. [200] The (SrIrO₃)1/(SrTiO₃)1 superlattice thus represents as a rare artificial layered structure for simulating the 2D single-band Hubbard model.[201] To introduce additional tunability to the layered structure, Hao et al. systematically changed the SrTiO3 thickness while leaving SrIrO₃ only a monolayer thick.^[199] The (SrIrO₃)1/(SrTiO₃)2 and (SrIrO₃)1/(SrTiO₃)3 with thicker SrTiO₃ spacers are indeed more insulating than (SrIrO₃)1/(SrTiO₃)1 with a SrTiO₃ monolayer spacer, similar to the case of SrRuO₃ (see Section 3.4.2), indicating that the charge-hopping channel across the SrTiO₃ spacer is finite and controllable, although the conduction band of SrTiO₃ is approximately 2 eV higher than the upper $J_{\text{eff}} = 1/2$ Hubbard band.^[75,202] The charge-hopping channels across the SrTiO₃ in the superlattice structure were reaffirmed in a subsequent theoretical work.[202]

4.1.2. Magnetic Structure Manipulation

The superlattice series also exhibits an interesting magnetic phase diagram. While all insulating superlattices are antiferromagnetically ordered at the base temperature, the transition temperature T_N can be changed by over two orders of magnitude.^[75] As shown in Figure 14a, (SrIrO₃)1/(SrTiO₃)1 has a maximum $T_{\rm N}$ of approximately 150 K, which decreases monotonically with increasing SrIrO₃ layer thickness. A well-defined antiferromagnetic transition is almost unobservable in the semimetallic $(SrIrO_3)4/(SrTiO_3)1$. On the other hand, T_N decreased with increasing the SrTiO₃ layer thickness, as shown in Figure 14b. This difference indicates that the SrIrO3 layer thickness alone does not determine T_N in the superlattices. A possible scenario is that the interlayer coupling decreases by separating the neighboring SrIrO₃ layers. In fact, the interlayer coupling is speculated to decrease exponentially with increasing distance from the neighboring magnetic layer.[227] This is consistent with the significantly reduced T_N from ≈ 150 to 40 K when the spatial distance between neighboring SrIrO3 layers increased from a SrTiO3 monolayer to a $SrTiO_3$ bilayer.^[199] Additionally, the T_N was found to be approximately the same when increasing the SrTiO₃ slab from bilayer to trilayer, which is indicative of reaching the regime where the 2D magnetic ordering is predominantly stabilized by magnetic anisotropy, which will be discussed in more detail in Section 4.3.2.

The magnetic anisotropy in square-lattice iridates is highly sensitive to dimensionality. The magnetization and magnetic scattering measurements suggest that (SrIrO₃)1/(SrTiO₃)1 has an easy plane anisotropy,^[75] similar to the bulk monolayersystems Sr₂IrO₄ and Ba₂IrO₄. [228] To resolve the magnetic anisotropy of (SrIrO₃)2/(SrTiO₃)1, Meyers et al. measured the azimuthal angle dependence of the magnetic peak using the magnetic resonant scattering technique. [203] A key difference between the easy-plane and easy-axis anisotropy is that the easyplane magnetic moments can be completely removed from the scattering plane, giving rise to the zero intensity of magnetic peak, while the magnetic peak intensity of an easy-axis system is nonzero at any finite azimuthal angle.[228-232] In parallel to the easy-axis model, the authors found that the magnetic peak is always observable in the studied azimuthal range. This result demonstrates that (SrIrO₃)2/(SrTiO₃)1 has a dominant easy-axis anisotropy,^[203] similar to Sr₃Ir₂O₇.

By virtue of the dimensionality-controlled magnetic anisotropy, Gong et al. prepared an interesting hybrid superlattice structure with an alternating stacking of (SrIrO₃)1/(SrTiO₃)1 and (SrIrO₃)2/(SrTiO₃)1 superlattices, as schematically showing in Figure 14d,e.[204] It is found that the hybrid superlattice orders only at a single temperature close to the Neel temperature of (SrIrO₃)2/(SrTiO₃)1, thus suggesting a uniform magnetic structure. However, detailed magnetic scattering measurements revealed that the hybrid superlattice has a dominant canted easy plane anisotropy similar to that of (SrIrO₃)1/(SrTiO₃)1. This result suggests that the magnetic behavior of the hybrid superlattice is not a simple addition to the magnetic order of the monolayer and bilayer superlattices. In contrast, integrating the monolayer member and bilayer member of the Ruddlesden-Popper iridates into a single structure leads to two separate ordering temperatures and the addition of orthogonal anisotropy.[233] The difference between the hybrid superlattice and hybrid Ruddlesden-Popper structure could be ascribed to the extra in-plane half-unit-cell slide between the monolayer and bilayer slabs in the Ruddlesden-Popper structure, which

16163028, 2023, 38, Downloaded from https://onlinelibrary.wiley.com/doi/10.1002/adfm.202301770 by University Of Temessee Gsm, Wiley Online Library on [14/04/2024]. See the Terms and Conditions (https://onlinelibrary.wiley.com/term

and-conditions) on Wiley Online Library for rules of use; OA articles are governed by the applicable Creative Commons License

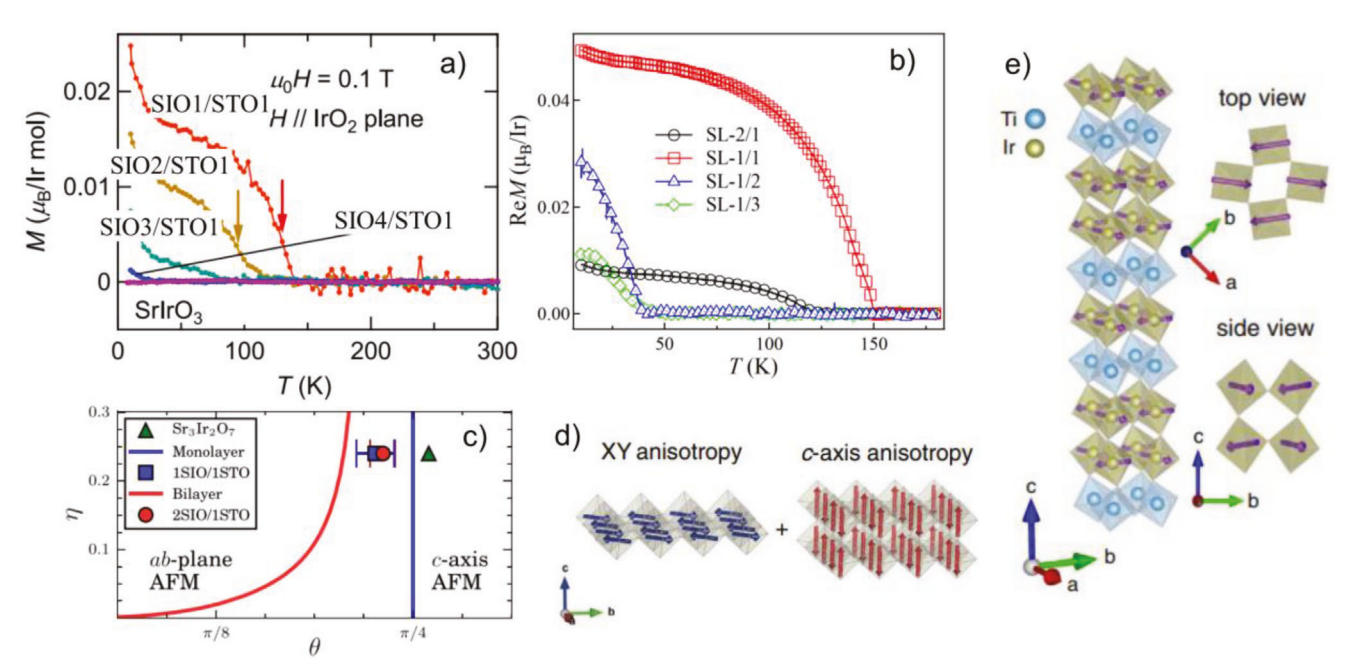


Figure 14. a) Temperature-dependent magnetization of $(SrIrO_3)n/(SrTiO_3)1$. Reproduced with permission. [75] Copyright 2015, American Physical Society. b) Temperature-dependent magnetization of $(SrIrO_3)n/(SrTiO_3)m$. Reproduced with permission. [199] Copyright 2017, American Physical Society. c) Classic magnetic phase diagram of monolayer- and bilayer-iridates. (here, η is the ratio of Hund's coupling on Coulomb repulsion and θ denotes tetragonal distortion of IrO₆ octahedron). Reproduced with permission. [203] Copyright 2019, Springer Nature. d) Schematic of the addition of an easy-plane monolayer iridate and easy-axis bilayer iridate. e) Magnetic structure of a hybrid $(SrIrO_3)1/(SrTiO_3)2/(SrTiO_3)1$ superlattice. Reproduced with permission. [204] Copyright 2022, American Physical Society.

suppresses monolayer-bilayer magnetic coupling.^[204] Another possible contribution is that the bilayer in the artificial superlattice is much closer to the spin–flop transition than its Ruddlesden-Popper counterpart.^[179]

In particular, square-lattice iridates have magnetic anisotropy primarily owing to the high-order perturbation from the virtual hopping between $J_{\text{eff}} = 1/2$ and $J_{\text{eff}} = 3/2$ states in the presence of a nonzero Hund's coupling. The induced pseudo-dipolar interaction produces a predominantly out-of-plane magnon gap, the sign of which varies with tetragonal distortion. This spin model explains the easy-plane anisotropy of Sr₂IrO₄ well and predicts an easy-axis antiferromagnetic state with IrO6 octahedra being heavily elongated along the c-axis. [198] However, the predicted magnon gap is much smaller than that measured using resonant inelastic X-ray scattering in Sr₃Ir₂O₇.^[234] Kim et al. reported that compared to single-layer iridates, an additional interlayer pseudo-dipolar interaction must also be considered in the bilayer system, which eventually leads to a far larger anisotropy term that favors c-axis anisotropy irrespective of tetragonal distortion.^[231,234] Meyers et al. found that, the octahedral tilt, albeit small in the (SrIrO₃)2/(SrTiO₃)1, significantly reduces the interlayer pseudo-dipolar interaction. Thus, although (SrIrO₃)2/(SrTiO₃)1 still hosted c-axis anisotropy similar to that of the bulk, it is closer to the phase boundary between the easyplane and easy-axis magnetic phases, as shown in Figure 14c. [203] Nevertheless, Gong et al. found that the octahedral tilt of the hybrid superlattice is smaller than that of (SrIrO₃)2/(SrTiO₃)1, indicating that the interlayer pseudo-dipolar interaction is not the primary reason for the dominant easy-plane anisotropy in the bilayer slab. A bilayer-Hubbard model analysis revealed that a moderate correlation strength also leads to a giant magnon gap and suggested that the bilayer system in the intermediate regime could be the long-sought excitonic insulator.^[235]

4.2. Enhancing and Manipulating $J_{\rm eff}=1/2$ Pseudospin Fluctuations

4.2.1. Extreme Spin Fluctuations in the 2D Limit

In general, spin fluctuation in the 2D limit is much stronger than that in 3D materials, and the critical behavior of 2D spin fluctuation depends sensitively on magnetic anisotropy.[236,237] For example, the correlation length diverges in a power-law manner when approaching the ordering temperature in the presence of Ising-type magnetic anisotropy. The divergence is faster if the easy-axis anisotropy is switched to the easy-plane anisotropy. The spin fluctuation then reaches an extreme situation of an exponential-type diverging trend when the anisotropy is zero. According to the Mermin-Wagner theorem, the spin fluctuation of 2D isotropic magnets is so strong that any longrange order will be melted at a non-zero temperature owing to $|M| < \frac{C}{\sqrt{T}} \cdot \frac{1}{|\ln \sqrt{|h|}|}$, where M represents net magnetization or staggered magnetization, h denotes a uniform field or staggered field in ferromagnetic or antiferromagnetic systems, and C is a constant.[238] Extreme spin fluctuation offers an ideal platform for achieving a highly efficient spin response, which is beneficial for designing ultrafast spintronic devices. Additionally, spin fluctuation in the 2D square lattice is recognized to be closely related

16163028, 2023, 38, Downloaded from https://onlinelibrary.wiley.com/doi/10.1002/adfm.202301770 by University Of Tennessee Gsm, Wiley Online Library on [14/04/2024]. See the Terms

and Conditions (https://onlinelibrary.wiley.com/terms-and-conditions) on Wiley Online Library for rules of use; OA articles are governed by the applicable Creative Commons License

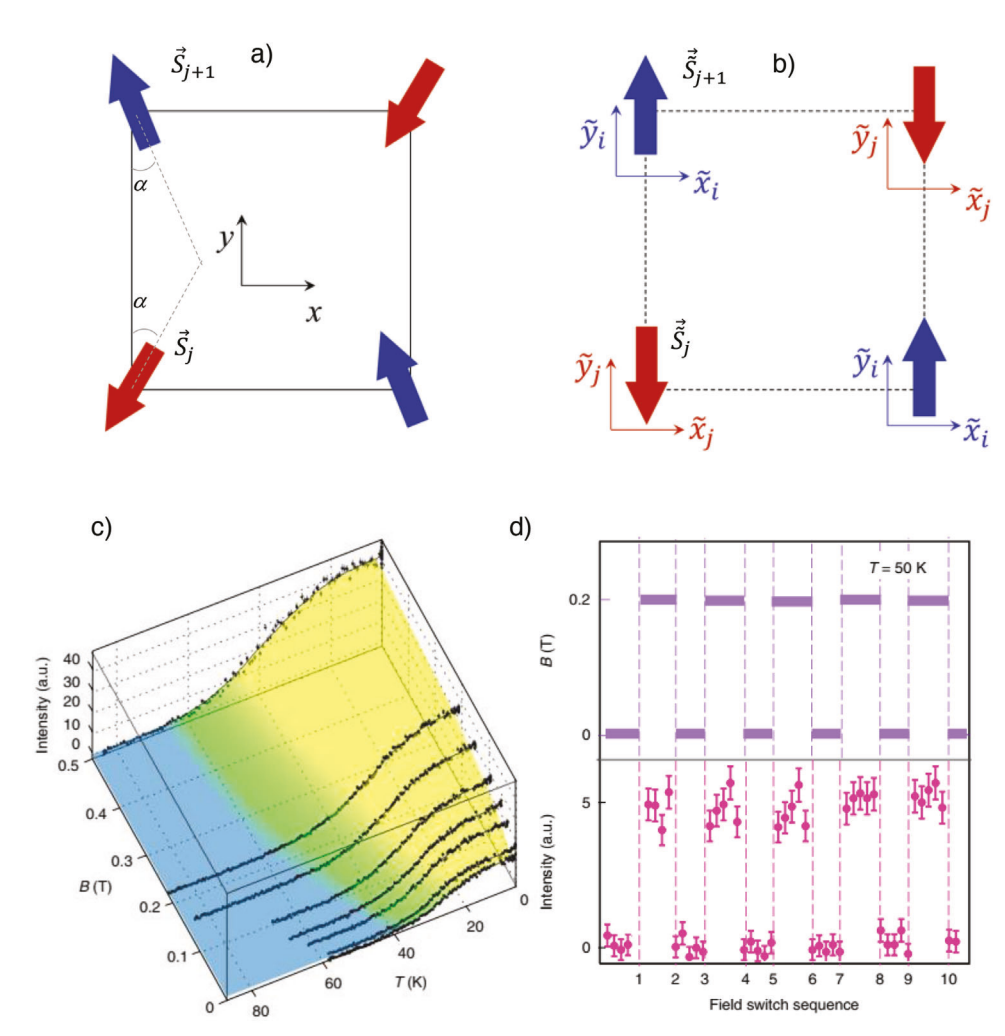


Figure 15. Schematics of canted antiferromagnetic structure in a) the global frame and b) a staggered local frame. c) Temperature-dependent magnetic peak intensity of (SrIrO₃)1/(SrTiO₃)2 under various magnetic fields. Reproduced with permission. Copyright 2018, Springer Nature. d) Switching sequence of a 0.2 T magnetic field and the associated change in the magnetic peak intensity of (SrIrO₃)1/(SrTiO₃)2. Reproduced with permission. [205] Copyright 2018, Springer Nature.

to the unconventional superconductivity in cuprates^[239,240] and is essential for advancing fundamental physical understanding.

4.2.2. Staggered Field Effect in Antiferromagnets

In certain antiferromagnetic materials with locally broken inversion symmetry, an external magnetic field may behave effectively as a staggered field to linearly couple to the antiferromagnetic order parameter. For example, in Cu benzoate, the Dzyaloshinskii–Moriya interaction can be written in the form $H_{\rm DM} = \sum (-1)^j \vec{D} \cdot$

 $(\vec{S}_j \times \vec{S}_{j+1})$, where \vec{D} is the Dzyaloshinskii–Moriya vector and \vec{S}_j is the spin operator at site j. Here, factor (-1) j denotes the staggered Dzyaloshinskii–Moriya pattern along the spin chain. After rotation along the \vec{D} direction through an alternating angle $\alpha/2$, where $\tan \alpha = D/J$, i.e., $\vec{S}_j^+ \to \widetilde{\vec{S}}_j^+ \cdot e^{i\alpha/2}$, $\vec{S}_{j+1}^+ \to \widetilde{\vec{S}}_{j+1}^+ \cdot e^{-i\alpha/2}$, the Dzyaloshinskii–Moriya term can be absorbed into the exchange interaction, giving rise to an effective Heisenberg-like model. [226] In 2D square-lattice systems, the Hamiltonian transformation

can be thought of as the conversion of the global spin frame (**Figure 15a**) to the twisted local frame (Figure 15b). Considering the Zeeman effect under an external field h along the x-direction $H_{\rm Zeeman} = -h\sum_j S_j^x$ in the redefined spin frame, one will arrive

at
$$H_{\text{Zeeman}} = -h \cos \frac{\alpha}{2} \sum_{j} \tilde{S}_{j}^{x} - h \sin \frac{\alpha}{2} \sum_{j} (-1)^{j} \tilde{S}_{j}^{y}$$
. Clearly, a stag-

gered field, linearly coupled with the AFM order parameter, is generated along the γ -axis. Furthermore, the staggered field effect is governed by D/J, which increases with spin—orbit coupling in general. Note that for a 1D spin chain, the staggered pattern of the Dzyaloshinskii—Moriya interaction on neighboring bonds does not break the global rotation symmetry.

4.2.3. Manipulating 2D Extreme Antiferromagnetic Fluctuations

The staggered field effect enables direct control of antiferromagnetic fluctuations. As mentioned in Section 4.1.2, $(SrIrO_3)1/(SrTiO_3)2$ and $(SrIrO_3)1/(SrTiO_3)3$ are at the 2D limit because the almost unchanged T_N with further suppressed

16163028, 2023, 3.8, Downloaded from https://onlinelibrary.wiley.com/doi/10.1002/adfm.202301770 by University Of Temnessee Gsm, Wiley Online Library on [14/04/2024]. See the Terms and Conditions (https://onlinelibrary.wiley.com/terms-and-conditions) on Wiley Online Library for rules of use; OA articles are governed by the applicable Creative Commons Licenses

www.advancedsciencenews.com

SCIENCE NEWS

enews.com www.afm-journal.de

interlayer coupling. [199,241] The in-plane staggered rotation pattern of IrO_6 octahedra and the large spin—orbit coupling gives rise to a substantial staggered field upon application of an in-plane magnetic field. As shown in Figure 15c, the crossover temperature T_0 , which can be treated as the ordering temperature for practical application, increases rapidly with the in-plane magnetic field. This observation is striking and even counterintuitive, considering that antiferromagnets are generally resilient to external magnetic fields. [242] The giant magnetic response was ascribed to the unique combination of a hidden SU(2) symmetry protected by the global crystal rotational symmetry, a large staggered field effect due to the strong spin—orbit coupling, and a vanishingly small interlayer coupling due to the quasi-2D nature of the artificial structure.

The sharp increase in the ordering temperature with the magnetic field indicates that the disordered state above T_0 can be transitioned into a long-range order state by applying certain magnetic fields, thus offering a novel approach for designing magnetic field switching of antiferromagnetic order, as shown in Figure 15d. The magnetic logic bit (on/off) is typically defined by the orientation of the order parameter in the magnetic ordering state in antiferromagnetic spintronics. [243-246] This is distinct from the above study, where the on state does not rely on the specific spin orientation in the ordered state, whereas the off state is simply a trivial disordered state. Moreover, the key to realizing such an efficient staggered response to a uniform stimulus is the SU(2)-symmetry-preserved Dzyaloshinskii-Moriya interaction, which can be achieved in various antiferroic materials via sophisticated lattice engineering strategies. This finding may stimulate more exciting work in exploring and realizing advanced nanoscale devices with antiferroic materials, which are much abundant but largely unexplored.

4.3. Enhancing and Manipulating $J_{\text{eff}} = 1/2$ Charge Fluctuations

4.3.1. Charge Fluctuations in the Intermediate Regime

The spin and charge degrees of freedom are entangled in the half-filled single-band Hubbard system because charge localization is tied to the formation of local magnetic moments. [201,247]Thus, the local magnetic moments are effective local particlehole pairs. Correspondingly, breaking up a pair by exciting the charges into the electron-hole continuum above the charge gap annihilates the local magnetic moment (i.e., longitudinal spin fluctuations), and vice versa. In the strong-coupling Mott limit, the local magnetic moments survive well above $T_{\rm N}$ because the charge degree of freedom remains frozen until the thermal fluctuations substantially disturb the Mott gap, which can be several orders of magnitudes higher than T_N . Consequently, the spincharge fluctuation is typically weak in this regime. In the weakcoupling Slater limit, the system is metallic above T_N without the local magnetic moments, thus resulting in weak spin-charge fluctuations. Compared to the two limits, the intermediate coupling regime has an optimum spin-charge fluctuation because both local moments and charge carriers exist above T_N . A generic phase diagram of a half-filled single-band system is schematically drawn in Figure 16a. As mentioned earlier, electron correlation is the key parameter in determining the charge fluctuations, which is expected to be maximized in the intermediate regime. Nevertheless, the crossover regime between the weak- and strong limit is quite broad. Whether or how the charge fluctuations vary with electron correlation in this regime is still an open question. In a broader picture, it is well known that both square lattice iridates and cuprates can be described with the single-band Hubbard model. However, after carrier doping, physical properties of the two systems are distinct. Explicitly speaking, holedoped cuprates are the profound high- $T_{\rm c}$ superconductors, while no superconductivity was observed in iridates yet. Resolving the physics of charge fluctuations in carrier-doped iridate superlattices may shed light on the lacking of superconductivity in the 5d oxides.

4.3.2. Modulating Electron Correlation via Epitaxial Strain

Epitaxial strain is one of the most vital and readily accessible knots for modulating the effective electron correlation in thinfilm and heterostructure studies. Kim et al. predicted that the $J_{\rm eff}=1/2$ bandwidth of the (SrIrO₃)1/(SrTiO₃)1 superlattice decreases with increasing tensile strain. [219] Kim et al. confirmed the $J_{\rm eff}=1/2$ band feature in the superlattice, as shown in Figure 16b, and unveiled that the substantial strain effect in (SrIrO₃)1/(SrTiO₃)1 as compared to Sr₂IrO₄ arises from the additional vertical hopping channels in the former, [202] as schematically shown in Figure 16c. Kim et al. later expanded the strain study on (SrIrO₃)m/(SrTiO₃)1 with m > 1. [200] Ranging from -4% to 4% of the epitaxial strain, the authors found that the electronic structure, albeit slightly different owing to the different stacking patterns of the superlattice series, displayed a similar strain dependence.

Experimentally, Yang et al. prepared a series of (SrIrO₃)1/(SrTiO₃)1 superlattices on different substrates to implement variable epitaxial strains of 0, -0.95%, and -1.06%. [249] With X-ray absorption spectroscopy measurements at the O K-edge, the authors found that the $J_{\rm eff}$ = 1/2 single-band feature was preserved under epitaxial strain. In the above X-ray absorption measurements, the intensity difference between the out-of-plane and in-plane channels was considered to be a measure of the relative hybridization strength of Ir with planar oxygen. [250,251] Notably, the X-ray absorption intensity in the out-of-plane channel was always larger than the in-plane signal, indicating a dominant hybridization between Ir and planar oxygen in all the superlattices (Figure 16d). By extracting the X-ray linear dichroism, which is the difference spectra between the out-of-plane and in-plane channels, the authors unveiled that in-plane hybridization systematically increased with compressive strain. This is a strong evidence that the effective electron correlation in superlattices decreases monotonically with increasing compressive strain.

Electronic correlation modulation was also captured in the electrical transport and magnetic measurements. Although all the superlattices had an insulating ground state, the insulating behavior was weakened in the compressed superlattices, confirming that the reduced electron correlation is consistent with the electronic structure. Interestingly, the authors observed an emergent high-temperature metallic phase in (SrIrO₃)1/(SrTiO₃)1 with the largest compressive strain.

16163028, 2023, 38, Downloaded from https://onlinelibrary.wiley.com/doi/10.1002/adfm.202301770 by University Of Temessee Gsm, Wiley Online Library on [14/04/2024]. See the Terms and Conditions (https://onlinelibrary.wiley.com/term

iditions) on Wiley Online Library for rules of use; OA articles are governed by the applicable Creative Commons License

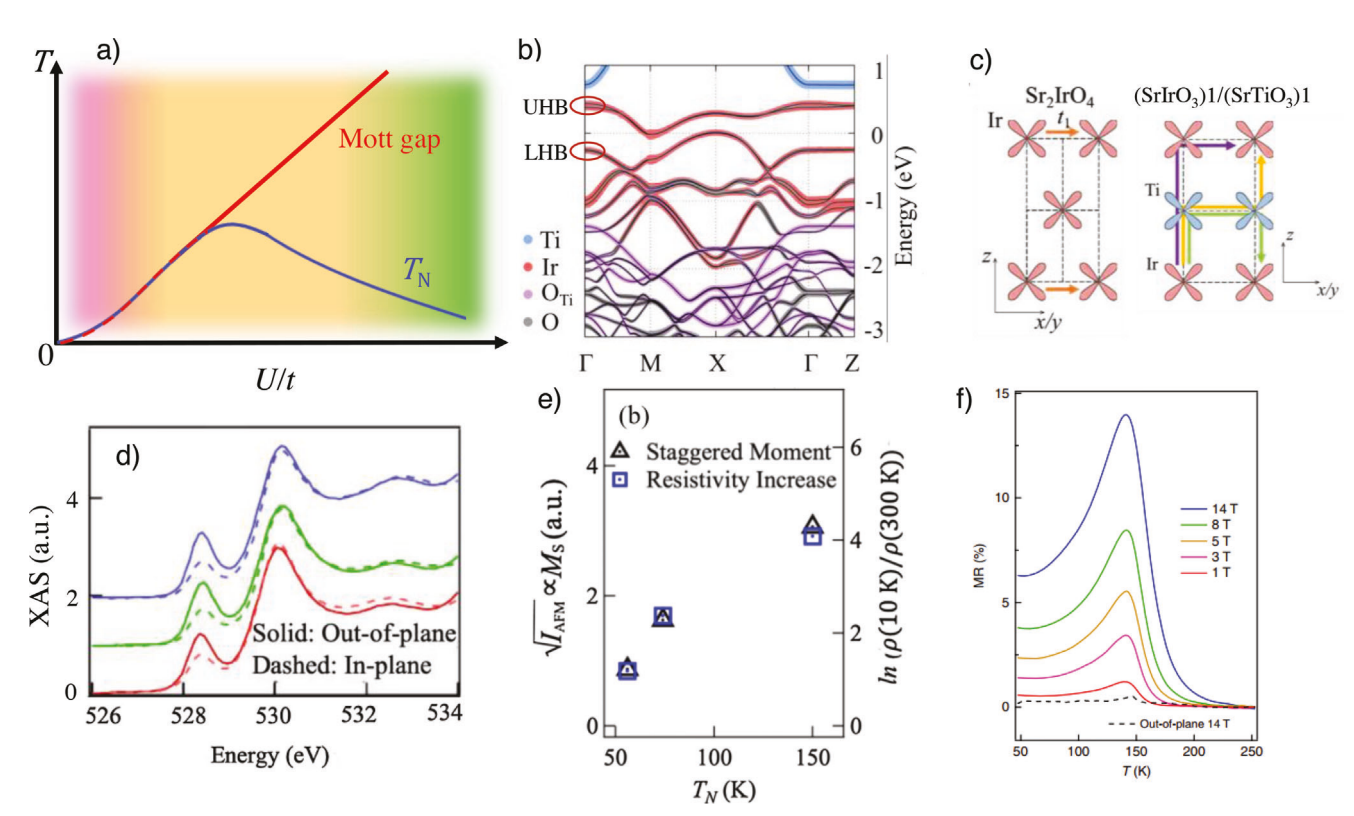


Figure 16. a) A generic phase diagram of the half-filled single-band Hubbard system as a function of *U*/t. b) Representative band structure of (SrIrO₃)1/(SrTiO₃)1. Reproduced with permission.^[202] Copyright 2016, American Physical Society. c) Orbital arrangements of Ir and Ti orbitals for Sr₂IrO₄ and (SrIrO₃)1/(SrTiO₃)1. Reproduced with permission.^[202] Copyright 2016, American Physical Society. d) Polarization-dependent X-ray absorption spectra of (SrIrO₃)1/(SrTiO₃)1 grown on SrTiO₃ (red), LSAT (green), and NdGaO₃ (blue) substrates. Reproduced with permission.^[249] Copyright 2020, American Physical Society. e) Staggered moment and resistivity increase of (SrIrO₃)1/(SrTiO₃)1 as a function of Neel temperature. Reproduced with permission.^[249] Copyright 2020, American Physical Society. f) Magnetoresistance dependence on temperature under various magnetic fields. Reproduced with permission.^[254] Copyright 2019, Springer Nature.

Moreover, all the superlattices had the same antiferromagnetic structure while the Neel temperature T_N decreased monotonically with increasing compressive strain. Intuitively, the halffilled single-band systems can be ascribed to Mott insulators because of the insulating state being established well above $T_{\rm N}$. [247] However, the reduced T_N , due to enhanced electron hopping, clearly contradicts the expectation of the exchange interaction $J \propto 4t^2/U$ (t and U denote electron hopping and correlation, respectively) at the strong coupling limit. [252] The magnetic peak intensity was quantified at the base temperature and revealed that the antiferromagnetic order parameter decreased monotonically with compressive strain. The fact that the antiferromagnetic order parameter, antiferromagnetic ordering temperature, and strength of the insulating behavior decrease simultaneously with the effective electron correlation (Figure 16e), revealed that charge fluctuations play a dominant role in the stability of the antiferromagnetic ordering. This is a key feature of Slater-type insulators in the weak-coupling limit.[247,253] The coexistence of characteristics of weak and strong coupling limits indicates that the (SrIrO₃)1/(SrTiO₃)1 superlattice system should be within the Slater-Mott crossover regime. In contrast to these two limits, knowledge about the intermediate regime is very limited, [253] which is discussed in more detail in the next section.

4.3.3. Manipulating Charge Fluctuations via Staggered Field Effect

To explore the intermediate regime in-depth, Hao et al. performed a comprehensive magnetotransport study of (SrIrO₃)1/(SrTiO₃)1 grown on a SrTiO₃ substrate. [254] As mentioned in Section 4.3.1, the intermediate regime (or the Slater-Mott crossover regime) hosts energetic charge fluctuations, which effectively lead to longitudinal spin fluctuations.^[249] The intriguing spin-charge interplay causes a notable anomaly in the resistivity when cooling through T_N . After applying an in-plane magnetic field, the authors observed a substantial magnetoresistance effect above T_N . Positive magnetoresistance is unusual because transverse spin fluctuations typically play a dominant role in antiferromagnetic semiconductors, and a negative magnetoresistance effect is commonly observed. [255,256] In addition, magnetoresistance above T_{N} exhibits a similar temperature dependence of the staggered susceptibility, which increases quickly with temperature approaching T_N , as shown in Figure 16f. Another interesting observation is the anisotropic characteristic of the anomalous magnetoresistance, i.e., a large magnetoresistance is observed when the magnetic field is parallel to the plane, whereas the out-of-plane magnetoresistance is almost unobservable. Note that because of the finite antiferromagnetic order parameter, a staggered field effect also exists in

www.advancedsciencenews.com



www.afm-journal.de

the intermediate regime, which is expected to stabilize the localized magnetic moments and enhance the particle-hole binding. As a large staggered field is only produced in the presence of an in-plane magnetic field owing to the in-plane net magnetic moment, this observation demonstrates that magnetoresistance originates from the suppression of spin-charge fluctuations under staggered magnetic fields.

Further insights into the anomalous magnetoresistance were gained through theoretical simulation using a 2D model built on a $J_{\rm eff} = 1/2$ square lattice. The authors reported that a staggered field increases the size of the antiferromagnetic order parameter by suppressing longitudinal spin fluctuation. The effect is most significant around T_N , where the spin susceptibility is maximized. The carrier density is strongly suppressed owing to the staggered magnetic field and reaches its minimum around $T_{\rm N}$. The carrier density reduction renders the anomalous magnetoresistance even more peculiar than the carrier mobility-driven magnetoresistance effects in most cases. [257–262] The anomalous magnetoresistance thus probes the longitudinal spin fluctuations by virtue of the spin-orbit coupling-induced staggered field effect, and offers a novel pathway to control the binding energy of the fluctuating particle-hole pairs via a magnetic field in the Slater-Mott crossover regime.

4.4. Topology-Correlation Interplay in Artificial Iridates

The intermediate regime is interesting not only because of the coexistence of spin and charge fluctuations but also because of the possibility of integrating both electronic topology and correlation in a single system. The concept of electronic topology was developed with the prediction and discovery of a variety of symmetryprotected surface states, edge states, etc.[263,264] These studies focused primarily on noninteracting systems that can be well understood in single-particle band pictures. Nonetheless, the interaction between electrons is typically nonzero in real materials and can sometimes lead to emergent phenomena beyond band structure prediction. A well-known example is the Mott insulating state in 2D half-filled single-band systems, for which noninteracting band theory predicts a good metal. Thus, whether and how the electronic topology manifests in correlated systems is generally unknown. This is particularly true for the intermediate regime, where both the single-electron approach in the weakcoupling limit and the superexchange approach in the strongcoupling limit fail to capture the energetic spin and charge excitations. It is believed that designer electronic topology and electronic correlation based on artificial heterostructures are promising routes to understanding the intriguing interplay.^[265]

As discussed in Section 4.3.2, (SrIrO₃)1/(SrTiO₃)1 is a realistic 2D half-filled Hubbard model system in the intermediate regime. To implement a nontrivial electronic topology, Yang et al. prepared (SrIrO₃)1/(CaTiO₃)1 superlattices on SrTiO₃ substrates.^[206] The key difference between the lattice structures of (SrIrO₃)1/(CaTiO₃)1 and (SrIrO₃)1/(SrTiO₃)1 is the realization of a large octahedral tilting in the former by reducing the tolerance factor. The effective Hamiltonian of the distorted 2D square lattice can be written as:

$$H = -t \sum_{\langle ij \rangle} \sum_{\alpha,\beta} \left[c_{i\alpha}^{\dagger} \left(e^{i\theta \mathbf{d}_{ij} \cdot \sigma} \right)_{\alpha\beta} c_{j,\beta} + h.c. \right] + U \sum_{i} n_{i\uparrow} n_{i\downarrow}$$
 (1)

where the first term accounts for the nearest-neighboring <ij> hopping, as schematically shown in **Figure 17**a, $c_{i\alpha}^{\dagger}$ ($c_{i\alpha}$) is the creation (annihilation) operator of a $J_{\rm eff} = 1/2$ electron with spin α on site i, σ is the vector of Pauli matrices, and U is the onsite electron-electron repulsion. In contrast to the typical 2D Hubbard model, electron hopping between neighboring sites is mediated by a finite SU(2) gauge field, $e^{i\theta d_{ij} \cdot \sigma}$. Octahedral rotation contributes to the staggered normal component of the gauge field, whereas octahedral tilt results in planar components. Unlike the rotation, the octahedral tilt breaks the global fourfold rotational symmetry such that the planar components cannot be gauged simultaneously on the square lattice. This effect can be intuitively captured as the gauge-invariant flux ϕ of any closed path of hopping, as shown in Figure 17b. In the absence of correlation, the model leads to a Dirac semimetal, and the nonzero flux emerges in the momentum space as a Berry phase, which is the main source of the spontaneous Hall effect. [266,267] In the strong-coupling limit, the flux gives rise to Ising anisotropy along d_{\square} .

Consistent with the model analysis, a large anomalous Hall effect below T_N was observed. Interestingly, both the saturated and remnant anomalous Hall conductivities exhibited a nonlinear temperature dependence, i.e., they first increased quickly and then began decreasing with cooling, as shown in Figure 17c. This unconventional behavior indicates that the anomalous Hall effect is governed by physical quantities that compete with each other. Indeed, the authors observed that the anomalous Hall angle σ_{vx}/σ_{xx} , which measures the strength of the charge deflection, increased with cooling, whereas the anomalous Hall coefficient $S_{\rm H} = \sigma_{vx} / M_{\rm s}$ which is proportional to the effective charge carrier density, had an opposite dependence, as shown in the inset of Figure 17c. Thus, the intrinsic anomalous Hall effect suggests that the impact of electronic topology extends to a Mott insulator in the moderately correlated regime. This is the central idea of the intermediate regime, where delocalized antiferromagnetic moments give rise to activated charge carriers and the two physical quantities increase at the expense of each other.

At the base temperature, the authors found that the magnetic structure indeed had an easy axis along d_{\square} , as shown in the inset of Figure 17d. Nevertheless, through resonant inelastic scattering measurements, the spin gap was found to be surprisingly large (\approx 85 meV), close to the giant magnon gap of the bilayer iridate $\mathrm{Sr_3Ir_2O_7}^{[234]}$ The gap size was far larger than that expected from the linear spin wave theory in the strong-coupling limit and can be understood only using a Hubbard model with a moderate correlation strength. The nonmonotonic anomalous Hall effect and the giant spin gap demonstrate that the interplay between the electronic topology and electronic correlation is so rich that the emergent phenomena are typically beyond the theorems relating to the weak-coupling or strong-coupling limit.

In complementary to the intrinsic anomalous Hall effect driven by the same group of $J_{\rm eff}=1/2$ electrons that form the antiferromagnetic Mott insulating state through symmetry engineering in a 2D square-lattice iridate block, the anomalous Hall effect was also observed in superlattices composed of SrIrO₃ and other magnetic compounds, as is discussed in the next section.



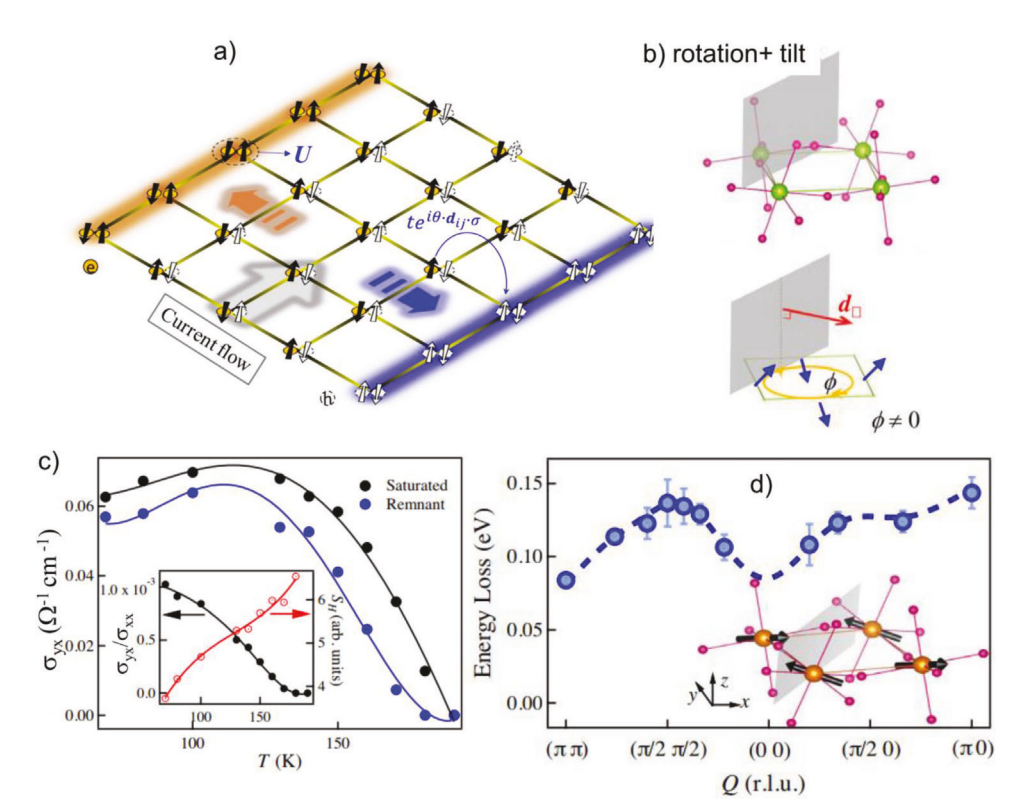


Figure 17. a) Schematic of a distorted 2D Hubbard system with a SU(2) gauge field modulating the electron hopping process. b) Square lattice with a finite octahedral rotation and tilt. The bottom panel displays the orientation of the Dzyaloshinskii-Moriya vectors. c) Temperature-dependent anomalous Hall conductivity of (SrIrO₃)1/(CaTiO₃)1. The inset displays the temperature dependencies of the anomalous Hall angle (left) and anomalous Hall coefficient (right). d) Magnon dispersion of (SrIrO₃)1/(CaTiO₃)1 at base temperature. The inset displays the ground-state magnetic structure of the superlattice. Reproduced with permission.^[206] Copyright 2022, American Physical Society.

4.5. Superlattices Composed of SrIrO₃ and Magnetic Compounds

The anomalous Hall effect is typically observed in materials with spin orbit coupling and broken time-reversal symmetry. [266] Although SrIrO₃ features a large spin—orbit coupling and theory predicts the existence of multiple nontrivial electronic topologies upon breaking a certain crystal symmetry, [268] the material by itself does not break the time-reversal symmetry. Thus, a large effort has been devoted to introducing long-range magnetic order in iridates by heterostructuring SrIrO₃ with different magnetic compounds.

For example, Nichols et al. synthesized a series of superlattices composed of SrIrO₃ and an antiferromagnetic insulator SrMnO₃. [212] In contrast to the two mother phases, the authors found that (SrIrO₃)1/(SrMnO₃)1 displayed a large net magnetization with the easy axis along the film normal direction. The interfacial ferromagnetism was ascribed to the charge transfer between Ir and Mn. In parallel to the spontaneously broken time-reversal symmetry, the anomalous Hall effect was observed below the magnetic ordering temperature. As shown in **Figure 18**a, the anomalous Hall effect is reduced and eventually vanished with increasing layer thickness, highlighting the crucial role of the interface in the emergent ferromagnetism. Skoropata et al. replaced SrMnO₃ with LaMnO₃ in the aforementioned superlattice structures and realized a potential topological Hall effect by engineering the interfacial Dzyaloshinskii-

Moriya interaction. [216] Recently, Gu et al. exploited CaMnO₃ as the main constituent of a superlattice composed of SrIrO₃. [218] The authors observed a metal–nonmetal crossover with decreasing layer thickness (Figure 18b), again highlighting the crucial role of the Ir/Mn interface in modulating the global electrical transport property. In contrast to building a SrIrO₃ based superlattice with magnetic conductors, Jaiswal et al. prepared superlattices with SrIrO₃ and LaCoO₃, which is a magnetic insulator at low temperatures. [213] They reported a large anomalous Hall effect when SrIrO₃ was in direct contact with LaCoO₃ at the atomic scale, whereas such effect was absent when SrIrO₃ and LaCoO₃ layers were separated by a thick SrTiO₃ spacer (Figure 18c). The authors argued that the anomalous Hall effect is due to proximity-induced magnetism in the SrIrO₃ layer.

In addition to the end members of $RMnO_3$, Yoo et al. constructed heterostructures with $SrIrO_3$ and $La_{0.7}Sr_{0.3}MnO_3$, $^{[207]}$ which is the best optimized for the double-exchange-dominated ferromagnetism. In addition to the ordinary Hall effect, the authors extracted the anomalous Hall component of the superlattices. With a systematic variation in the layer thickness, they found that the anomalous Hall resistivity always scales linearly with the square of the longitudinal resistivity, as shown in Figure 18d. $^{[266]}$ The anomalous Hall effect was ascribed to proximity-induced magnetism in the $SrIrO_3$ layer, whereas the intriguing double-SrO layer at the Ir/Mn interface plays a subtle role in mediating the exchange interaction. Yi et al. found

1616328, 2023, 3, B. Downloaded from https://onlinelibrary.wiley.com/doi/10.1002/adfm.202301770 by University Of Temnessee Gsm., Wiley Online Library on [14/04/2024]. See the Terms and Conditions (https://onlinelibrary.wiley.com/emes-and-conditions) on Wiley Online Library for rules of use; OA articles are governed by the applicable Creative Commons Licenses

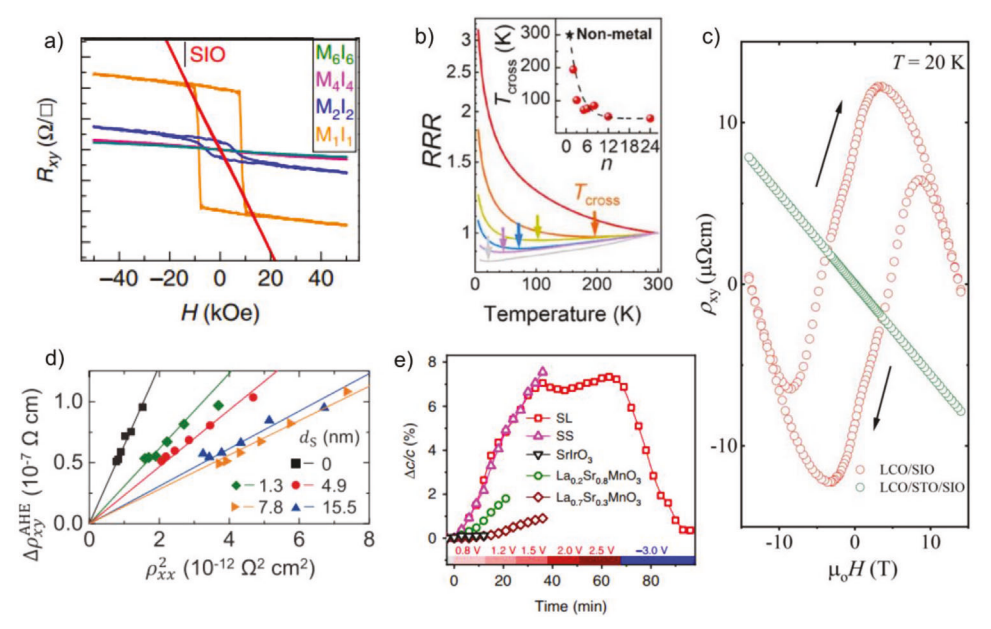


Figure 18. a) Anomalous Hall resistivity as a function of *c*-axis magnetic field of a series of (SrIrO₃)γ/(SrMnO₃)*x* (Mxly in the notation) superlattices. Reproduced with permission.^[218] Copyright 2016, Springer Nature. b) Temperature-dependent resistivity of SrIrO₃/CaMnO₃. Reproduced with permission.^[218] Copyright 2022, American Chemical Society. c) Field-dependent anomalous Hall resistivity of SrIrO₃/LaCoO₃ and SrIrO₃/SrTiO₃/LaCoO₃ heterostructures. Reproduced with permission.^[213] Copyright 2022, Wiley-VCH GmbH. d) Relation between anomalous Hall resistivity and the square of longitudinal resistivity of SrIrO₃/La_{0.7}Sr_{0.3}MnO₃ heterostructures. Reproduced with permission.^[207] Copyright 2021, Springer Nature. e) Time evolution of the lattice structure of SrIrO₃/La_{0.8}Sr_{0.2}MnO₃ superlattice under ionic liquid gating. Reproduced with permission.^[211] Copyright 2022, Springer Nature.

that attaching La_{0.7}Sr_{0.3}MnO₃ to SrIrO₃ at the atomic scale leads to a large variation in magnetic anisotropy. [208,210] In addition to $SrIrO_3/La_{0.7}Sr_{0.3}MnO_3 \ superlattices, \ Yi\ et\ al.\ prepared\ superlattices\ composed\ of\ SrIrO_3\ and\ La_{0.8}Sr_{0.2}MnO_3.^{[211]}\ Interestingly,$ the authors observed a reversible phase transformation with a lattice change as large as 7% at room temperature using ionic liquid gating. The phase transformation is associated with a clear modulation of the electronic, magnetic, and optical properties due to the reversible transfer of oxygen and/or hydrogen ions. This work further demonstrates that digital superlattices usually host emergent functionalities that have not been seen in the mother phases or in their solid solutions. The observed phenomena indicate that the strong spin-orbit coupling of SrIrO₃ and the timereversal symmetry breaking field offered by the magnetic compounds are the two key ingredients for inducing an Anomalous Hall effect. In addition to the atomic spin-orbit coupling, Rashba spin-orbit coupling also plays a critical role in dissipationless transport. Here, breaking the inversion symmetry is the key. One possible direction towards this end is to construct a tricolor iridate superlattice, to simultaneously break the spatial inversion and the time-reversal symmetry.

4.6. Superlattices Composed of Iridates Other Than SrIrO₃

As the 3D end member of the iridate Ruddlesden-Popper family, SrIrO₃ has a simple perovskite structure similar to most functional oxides and is widely used to construct iridate based superlattices. With the development of epitaxy techniques, studies have

also been conducted on superlattices composed of other iridates, such as Sr₂IrO₄ and CaIrO₃.

Liu et al. grew superlattices with alternating Sr₂IrO₄ and SrTiO₂ layers.^[269] The superlattices were found to have an emergent magnetoelectric phase transition, probably due to the double SrO layers at the interface (Figure 19a). By replacing SrTiO₃ with BaTiO₃, the magnetoelectric transition was substantially enhanced, with a pronounced magnetoelectric coefficient. Gruenewald et al. integrated Sr₂IrO₄ and LaSrGaO₄ atomically in a planar manner and realized 1D ${\rm IrO_2}$ stripes. [270] From resonant inelastic X-ray scattering measurements, as shown in Figure 19b, the authors found that the 1D stripes clearly enhanced exchange interactions and confined orbital excitations compared with Sr₂IrO₄. In addition to the interesting dielectric and magnetic behaviors observed on Sr₂IrO₄ based superlattices, Xu et al. found an enhanced anisotropic magnetoresistance effect in superlattices composed of Sr₂IrO₄ and La_{0.7}Sr_{0.3}MnO₃.^[271] By modulating the magnetic field direction, a nonvolatile memory based on the AMR effect was realized.

Similar to SrIrO₃, CaIrO₃ is semimetallic and can be stabilized into the perovskite phase using epitaxy. Recently, CaIrO₃ has been increasingly used to construct atomic-scale superlattices. For example, Lim et al. prepared a series of CaIrO₃/SrTiO₃ superlattices and found enhanced anisotropic magnetoresistance as compared to SrIrO₃/SrTiO₃ superlattices. Interestingly, the authors found that the anisotropic magnetoresistance of (CaIrO₃)1/(SrTiO₃)1 was maximized at 45°, whereas the largest anisotropic magnetoresistance of (SrIrO₃)1/(SrTiO₃)1 occurred at 90°. This anisotropic magnetoresistance difference indicates that replacing SrIrO₃ with CaIrO₃ in the superlattice causes

16163028, 2023, 38, Downloaded from https://onlinelibrary.wiley.com/doi/10.1002/adfm.202301770 by University Of Temessee Gsm, Wiley Online Library on [14/04/2024]. See the Terms and Conditions (https://onlinelibrary.wiley.com/

nditions) on Wiley Online Library for rules of use; OA articles are governed by the applicable Creative Commons License

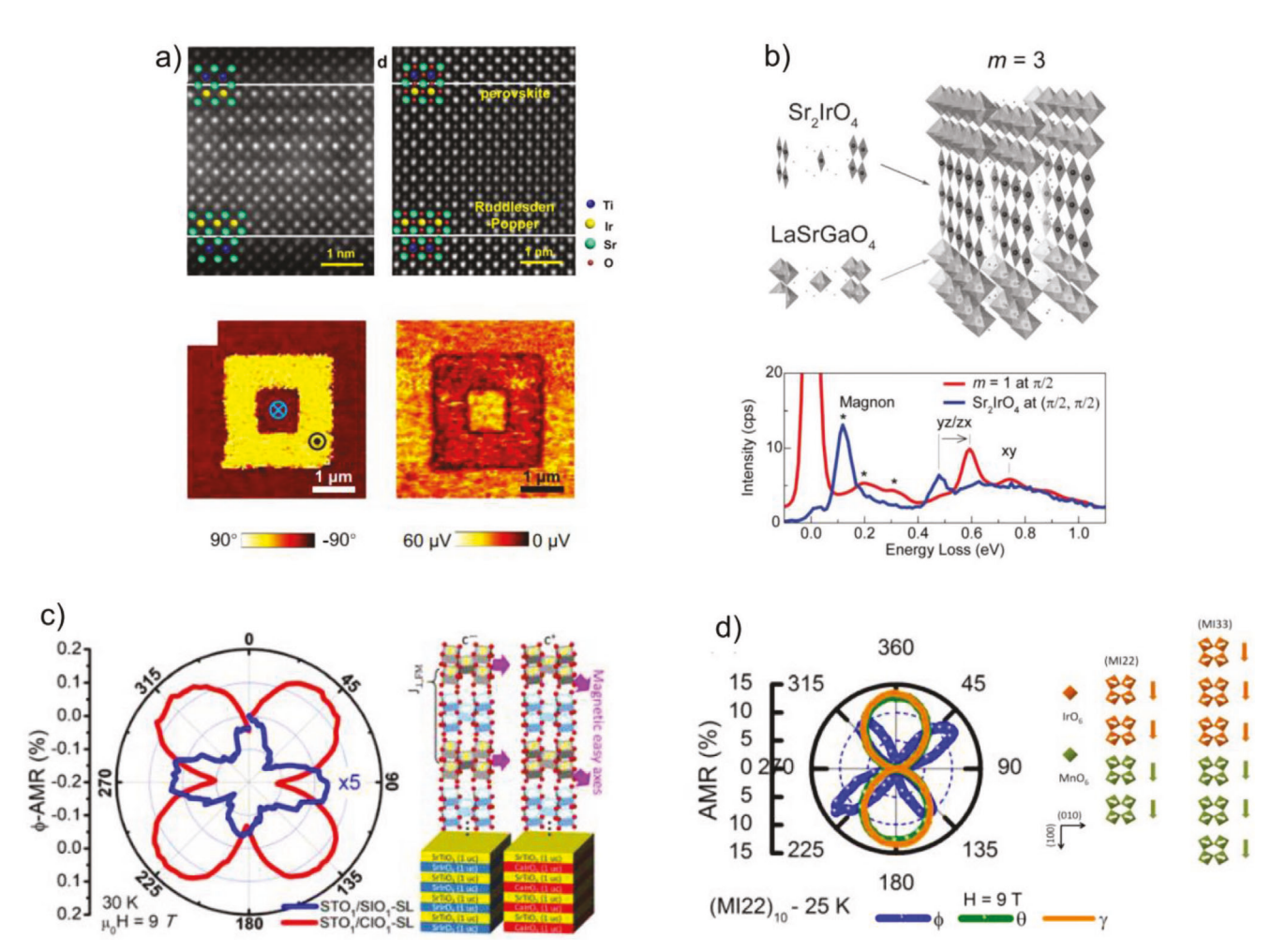


Figure 19. a) Atomically resolved High angle annular dark-field and integrated differential phase contrast images of $(Sr_2IrO_4)3/(SrTiO_3)6$ superlattice. The bottom panel shows the out-of-plane PFM images of the superlattice at 3.7 K. Reproduced with permission. ^[269] Copyright 2021, Springer Nature. b) Schematic diagram of the *a*-axis-oriented $(Sr_2IrO_4)3/(LaSrGaO_4)5$ superlattice. The bottom panel displays resonant inelastic X-ray scattering spectra of the superlattice and Sr_2IrO_4 . Reproduced with permission. ^[270] Copyright 2016, Wiley-VCH GmbH. c) Anisotropic magnetoresistance effect and schematic of $(CaIrO_3)1/(SrTiO_3)1$. Reproduced with permission. ^[273] Copyright 2020, American Chemical Society. d) Anisotropic magnetoresistance effect and magnetic structure of $CaIrO_3/(CaMnO_3)$. Reproduced with permission. ^[274] Copyright 2022, American Physical Society.

a substantial change in the magnetic structure, as shown in Figure 19c. Fourfold anisotropic magnetoresistance was also observed in a recent study by Vagadia et al., who constructed multiple superlattices composed of CaIrO₃ and CaMnO₃. [274] The anisotropic magnetoresistance magnitude was found to be as high as 70%, which is approximately two orders of magnitude greater than the value reported for (CaIrO₃)1/(SrTiO₃)1, as shown in Figure 19d. This unprecedentedly high anisotropic magnetoresistance was ascribed to the combination of a strong biaxial anisotropy and a metamagnetic transition.

In addition to SrIrO₃, CaIrO₃, and Sr₂IrO₄, we would like to point out that BaIrO₃ and Sn-doped SrIrO₃ are another two elegant composites in constructing iridate superlattices. Perovskite BaIrO₃ is reported to host a big lattice and a high crystal symmetry, giving rise to the best conductivity in the perovskite iridate family.^[275] By integrating it with BaTiO₃ into a superlattice, one might able to have a rare combination of strong spin–orbit coupling with strong inversion symmetry breaking field, which

is beneficial for boosting the magnetoelectric coupling. [276] Sndoped SrIrO3 is the first perovskite iridate with long-range magnetic order. [277,278] It would be interesting to see how dimensionality confinement affects the magnetism by carefully designing a superlattice structure.

5. Conclusions and Outlook

Ruthenate and iridate based perovskite oxide superlattices exemplify the power of bottom-up synthesis by heteroepitaxial growth in overcoming the material bottleneck in solid-state chemistry. Unlike the large number of material families of 3d transition metal oxides, studies on 4d and 5d systems have been limited to a few compounds available in bulk form. Artificial crystals built from atomically thin SrRuO₃ and SrIrO₃ demonstrate a route for creating coherent layered structures that are unobtainable using conventional protocols. A particularly important aspect of the reported studies is that one can create analogous systems to the

known bulk compounds. The analogy is not only in the layered character of the crystal structure but also in the physics behind the electronic and magnetic states. It is crucial to make such comparisons when designing artificial crystals because they determine the crystal unit that plays an essential role in the unified picture of the physical properties. A closely related direction is the interface and heterostructures of 3d and 4d, 3d and 5d, and 4d and 5d oxides. One advantage of such systems is that they bring together different degrees of correlation and spin-orbit coupling. Although some studies have adopted this direction, the complexity of such systems often renders difficulty in disentangling the roles of the different layers in driving the observed properties, particularly when the layers are unit-cell thin. The superlattices with quantum-confined structures of atomically thin SrRuO₃ and SrIrO₃ layers fill the gap in understanding. They established that the ground state and properties of a monolayer of SrRuO3 and SrIrO₃ are favorable, which serves as the basis for using them as building blocks for more complex structures with spin-orbit coupling. This allows the reexamination of ultrathin superlattices with 3d oxides and rejuvenates this research direction. It also sets a blueprint for developing new superlattices of this kind. Note that the analogy between the superlattice and bulk does not mean that the properties of the artificial crystals are the same as those of the bulk in every aspect. Instead, the key is to be able to identify both their similarities and differences and understand the reasons behind them. This builds the foundation for further exploiting the additional structural degrees of freedom afforded by the superlattice to generate structural variants beyond the bulk compounds and stabilize new phases.

An immediate benefit of superlattice synthesis is the possibility of obtaining a large variety of new oxide systems with strong spin-orbit coupling, which is the key property that distinguishes 4d and 5d systems from their 3d counterparts. This opens the door to exploring topology-driven physics and properties of oxides through structural and symmetry engineering. This is an important future direction for this class of systems. Proposals of topological designs of perovskite oxide superlattices have indeed been put forward for about ten years. However, numerous predictions are based on the single-particle picture, which may not be realistic because of the significant electronic correlation remaining in the 4d and 5d orbitals. This characteristic could result in 4d and 5d oxides in a regime where topology and correlation coexist and interact with each other. For instance, one of the most important consequences of correlation is magnetism, and the role of spin-orbit coupling in correlated systems has traditionally been viewed as a perturbation that controls magnetic anisotropy. On the other hand, if spin-orbit coupling leads to a nontrivial electronic topology, magnetically driven topological states may emerge, and their emergence can very well depend on magnetic anisotropy. The intrinsic anomalous Hall effect is an excellent example, in which both the Berry phase and magnetic order with a proper easy axis are necessary. Therefore, one may consider the anomalous Hall effect as a combined result of spinorbit coupling, correlation, and crystal symmetry, which can be implemented in artificial crystals by design. Even in the strong correlation limit, the impact of topology may still survive but in a different form because the spin-dependent hopping that is responsible for topology is mapped to the Dzyaloshinskii-Moriya interactions. In fact, exchange magnetic anisotropy is a result of

Dzyaloshinskii-Moriya interactions, which are a vital source of magnetoelectricity in oxides. Artificial crystals of 4d and 5d electrons may bridge several different research fields.

From the application point of view, creating magnetic oxides with substantial spin-orbit coupling is crucial for the development of spintronics. Future directions include realizing magnetic materials with especially large magnetic anisotropy for nonvolatile memory and developing efficient spin-charge conversion for energy harvesting. Finally, there is great potential for applying new experimental methods from parallel developments. Examples include ionic-liquid gating and freestanding membranes. The superlattice structure could have the advantage of maintaining structural stability when the ions move in and out. Broadly stated, this may have significant implications in catalysis studies because precious metals are known to be good catalysts. Controlling the 4d and 5d electronic states in artificial crystals can lead to improved performances.

Acknowledgements

This work was supported by the Basic Science Research Programs through the National Research Foundation of Korea (NRF-2021R1A2C2011340 and 2022R1C1C2006723). L.H. acknowledges financial support from the international partnership program of the Chinese Academy of Sciences (145GJHZ2022044MI), the Collaborative Innovation Program of Hefei Science Center, CAS (2022HSC-CIP005), and the HFIPS Director's Fund (2023YZGH01). J.L. acknowledges support from the National Science Foundation under Grant No. DMR-1848269.

Conflict of Interest

The authors declare no conflict of interest.

Keywords

epitaxy, iridates, magnetotransport, spin-orbit coupling, ruthenates, superlattices

> Received: February 15, 2023 Revised: May 9, 2023 Published online: May 26, 2023

1616928, 2023, 3, B. Downloaded from https://onlinelibrary.wiley.com/doi/10.1002/adfm.202301770 by University Of Temnessee Gsm, Wiley Online Library on [14/04/2024]. See the Terms and Conditions (https://onlinelibrary.wiley.com/ems-and-conditions) on Wiley Online Library for rules of use; OA articles are governed by the applicable Creative Commons Licenses

- [1] C. H. Ahn, K. M. Rabe, J. M. Triscone, Science 2004, 303, 488.
- [2] J. Chakhalian, J. W. Freeland, A. J. Millis, C. Panagopoulos, J. M. Rondinelli, Rev. Mod. Phys. 2014, 86, 1189.
- [3] H. Y. Hwang, Y. Iwasa, M. Kawasaki, B. Keimer, N. Nagaosa, Y. Tokura, Nat. Mater. 2012, 11, 103.
- [4] R. Ramesh, D. G. Schlom, Nat. Rev. Mater. 2019, 4, 257.
- [5] Y. Tokura, N. Nagaosa, Science 2000, 288, 462.
- [6] P. Yu, Y.-H. Chu, R. Ramesh, Mater. Today 2012, 15, 320.
- [7] P. Zubko, S. Gariglio, M. Gabay, P. Ghosez, J.-M. Triscone, Annu. Rev. Condens. Matter Phys. 2011, 2, 141.
- Y. Tokura, M. Kawasaki, N. Nagaosa, Nat. Phys. 2017, 13, 1056.
- [9] I. Heber, Nature 2009, 459, 28.
- [10] H. N. Lee, H. M. Christen, M. F. Chisholm, C. M. Rouleau, D. H. Lowndes, Nature 2005, 433, 395.
- [11] A. K. Geim, I. V. Grigorieva, Nature 2013, 499, 419.
- [12] K. T. Kang, J. Park, D. Suh, W. S. Choi, Adv. Mater. 2019, 31, 1803732.



- [14] T. Takayama, J. Chaloupka, A. Smerald, G. Khaliullin, H. Takagi, J. Phys. Soc. Jpn. 2021, 90, 062001.
- [15] A. Ohtomo, H. Y. Hwang, Nature 2004, 427, 423.
- [16] A. Ohtomo, D. A. Muller, J. L. Grazul, H. Y. Hwang, Nature 2002, 419, 378
- [17] S. S. A. Seo, W. S. Choi, H. N. Lee, L. Yu, K. W. Kim, C. Bernhard, T. W. Noh, *Phys. Rev. Lett.* **2007**, 99, 266801.
- [18] V. R. Cooper, S. S. A. Seo, S. Lee, J. S. Kim, W. S. Choi, S. Okamoto, H. N. Lee, Sci. Rep. 2014, 4, 6021.
- [19] W. S. Choi, S. Lee, V. R. Cooper, H. N. Lee, *Nano Lett.*. 2012, 12, 4590.
- [20] W. S. Choi, H. Ohta, H. N. Lee, Adv. Mater. 2014, 26, 6701.
- [21] W. S. Choi, S. A. Lee, J. H. You, S. Lee, H. N. Lee, *Nat. Commun.* 2015, 6, 7424.
- [22] S. S. A. Seo, M. J. Han, G. W. J. Hassink, W. S. Choi, S. J. Moon, J. S. Kim, T. Susaki, Y. S. Lee, J. Yu, C. Bernhard, H. Y. Hwang, G. Rijnders, D. H. A. Blank, B. Keimer, T. W. Noh, *Phys. Rev. Lett.* **2010**, 104, 036401.
- [23] W. S. Choi, H. Ohta, S. J. Moon, Y. S. Lee, T. W. Noh, *Phys. Rev. B* 2010, 82, 024301.
- [24] H. Ohta, S. Kim, Y. Mune, T. Mizoguchi, K. Nomura, S. Ohta, T. Nomura, Y. Nakanishi, Y. Ikuhara, M. Hirano, H. Hosono, K. Koumoto, *Nat. Mater.* 2007, 6, 129.
- [25] S. S. A. Seo, J. H. Lee, H. N. Lee, M. F. Chisholm, W. S. Choi, D. J. Kim, J. Y. Jo, H. Kim, J. Yu, T. W. Noh, Adv. Mater. 2007, 19, 2460.
- [26] Y. L. Tang, Y. L. Zhu, X. L. Ma, A. Y. Borisevich, A. N. Morozovska, E. A. Eliseev, W. Y. Wang, Y. J. Wang, Y. B. Xu, Z. D. Zhang, S. J. Pennycook, *Science* 2015, 348, 547.
- [27] A. K. Yadav, C. T. Nelson, S. L. Hsu, Z. Hong, J. D. Clarkson, C. M. Schlepütz, A. R. Damodaran, P. Shafer, E. Arenholz, L. R. Dedon, D. Chen, A. Vishwanath, A. M. Minor, L. Q. Chen, J. F. Scott, L. W. Martin, R. Ramesh, *Nature* 2016, 530, 198.
- [28] E. R. Hoglund, D.-L. Bao, A. O'Hara, S. Makarem, Z. T. Piontkowski, J. R. Matson, A. K. Yadav, R. C. Haislmaier, R. Engel-Herbert, J. F. Ihlefeld, J. Ravichandran, R. Ramesh, J. D. Caldwell, T. E. Beechem, J. A. Tomko, J. A. Hachtel, S. T. Pantelides, P. E. Hopkins, J. M. Howe, Nature 2022, 601, 556.
- [29] J. Ravichandran, A. K. Yadav, R. Cheaito, P. B. Rossen, A. Soukiassian, S. J. Suresha, J. C. Duda, B. M. Foley, C.-H. Lee, Y. Zhu, A. W. Lichtenberger, J. E. Moore, D. A. Muller, D. G. Schlom, P. E. Hopkins, A. Majumdar, R. Ramesh, M. A. Zurbuchen, *Nat. Mater.* 2014, 13, 168.
- [30] D. W. Jeong, W. S. Choi, T. D. Kang, C. H. Sohn, A. David, H. Rotella, A. A. Sirenko, C. H. Lee, J. H. Kim, U. Lüders, W. Prellier, Y. J. Kim, Y. S. Lee, T. W. Noh, *Phys. Rev. B* **2011**, *84*, 115132.
- [31] W. S. Choi, D. W. Jeong, S. S. A. Seo, Y. S. Lee, T. H. Kim, S. Y. Jang, H. N. Lee, K. Myung-Whun, *Phys. Rev. B* **2011**, *83*, 195113.
- [32] S. H. Chang, S. K. Kim, Y.-M. Kim, Y. Dong, C. M. Folkman, D. W. Jeong, W. S. Choi, A. Y. Borisevich, J. A. Eastman, A. Bhattacharya, D. D. Fong, APL Mater. 2019, 7, 071117.
- [33] D. W. Jeong, W. S. Choi, S. Okamoto, J. Y. Kim, K. W. Kim, S. J. Moon, D. Y. Cho, H. N. Lee, T. W. Noh, Sci. Rep. 2014, 4, 6124.
- [34] A. V. Boris, Y. Matiks, E. Benckiser, A. Frano, P. Popovich, V. Hinkov, P. Wochner, M. Castro-Colin, E. Detemple, V. K. Malik, C. Bernhard, T. Prokscha, A. Suter, Z. Salman, E. Morenzoni, G. Cristiani, H. U. Habermeier, B. Keimer, *Science* 2011, 332, 937.
- [35] J. A. Mundy, C. M. Brooks, M. E. Holtz, J. A. Moyer, H. Das, A. F. Rébola, J. T. Heron, J. D. Clarkson, S. M. Disseler, Z. Liu, A. Farhan, R. Held, R. Hovden, E. Padgett, Q. Mao, H. Paik, R. Misra, L. F. Kourkoutis, E. Arenholz, A. Scholl, J. A. Borchers, W. D. Ratcliff, R. Ramesh, C. J. Fennie, P. Schiffer, D. A. Muller, D. G. Schlom, *Nature* 2016, 537, 523.

- [36] W. R. Grove, Philos. Trans. R. Soc. London 1852, 142, 87.
- [37] J. E. Greene, J. Vac. Sci. Technol. A 2017, 35, 05C204.
- [38] M. Dawber, in Epitaxial Growth of Complex Metal Oxides, 2nd ed. (Eds: G. Koster, M. Huijben, G. Rijnders), Woodhead Publishing, Sawston, UK 2015, p. 37.
- [39] J. M. Triscone, O. Fischer, O. Brunner, L. Antognazza, A. D. Kent, M. G. Karkut, Phys. Rev. Lett. 1990, 64, 804.
- [40] M. Dawber, N. Stucki, C. Lichtensteiger, S. Gariglio, P. Ghosez, J.-M. Triscone, Adv. Mater. 2007, 19, 4153.
- [41] S. J. Callori, J. Gabel, D. Su, J. Sinsheimer, M. V. Fernandez-Serra, M. Dawber, *Phys. Rev. Lett.* **2012**, *109*, 067601.
- [42] C. Domínguez, A. B. Georgescu, B. Mundet, Y. Zhang, J. Fowlie, A. Mercy, A. Waelchli, S. Catalano, D. T. L. Alexander, P. Ghosez, A. Georges, A. J. Millis, M. Gibert, J.-M. Triscone, *Nat. Mater.* 2020, 19, 1182.
- [43] B. Mundet, C. Domínguez, J. Fowlie, M. Gibert, J.-M. Triscone, D. T. L. Alexander, Nano Lett.. 2021, 21, 2436.
- [44] M. Gibert, P. Zubko, R. Scherwitzl, J. Íñiguez, J.-M. Triscone, *Nat. Mater.* 2012, 11, 195.
- [45] H. M. Smith, A. F. Turner, Appl. Opt. 1965, 4, 147.
- [46] J. R. Arthur Jr., J. Appl. Phys. 1968, 39, 4032.
- [47] H. M. Christen, G. Eres, J. Phys.: Condens. Matter 2008, 20, 264005.
- [48] A. Ojeda-G-P, M. Döbeli, T. Lippert, Adv. Mater. Interfaces 2018, 5, 1701062.
- [49] S. A. Lee, S. Oh, J. Lee, J.-Y. Hwang, J. Kim, S. Park, J.-S. Bae, T. E. Hong, S. Lee, S. W. Kim, W. N. Kang, W. S. Choi, Sci. Rep. 2017, 7, 11583.
- [50] S. Woo, H. Choi, S. Kang, J. Lee, A. David, W. Prellier, Y. Kim, H. Y. Kim, W. S. Choi, Appl. Surf. Sci. 2020, 499, 143924.
- [51] B. Kim, S. A. Lee, D. Seol, W. S. Choi, Y. Kim, Curr. Appl. Phys. 2017, 17, 1721.
- [52] E. K. Ko, J. Mun, H. G. Lee, J. Kim, J. Song, S. H. Chang, T. H. Kim, S. B. Chung, M. Kim, L. Wang, T. W. Noh, Adv. Funct. Mater. 2020, 30, 2001486
- [53] J. Thompson, J. Nichols, S. Lee, S. Ryee, J. H. Gruenewald, J. G. Connell, M. Souri, J. Johnson, J. Hwang, M. J. Han, Appl. Phys. Lett. 2016, 109, 161902.
- [54] Z. Deng, J. Liu, Y. Hong, L. Wei, S. Hu, W. Xiao, L. Li, L. Wang, K. Chen, Z. Liao, Adv. Mater. Interfaces 2022, 9, 2201371.
- [55] S. G. Jeong, J. Kim, A. Seo, S. Park, H. Y. Jeong, Y.-M. Kim, V. Lauter, T. Egami, J. H. Han, W. S. Choi, Sci. Adv. 2022, 8, eabm4005.
- [56] W. Nunn, T. K. Truttmann, B. Jalan, J. Mater. Res. 2021, 36, 4846.
- [57] W. Nunn, A. K. Manjeshwar, J. Yue, A. Rajapitamahuni, T. K. Truttmann, B. Jalan, Proc. Natl. Acad. Sci. USA 2021, 118, e2105713118
- [58] G. Koster, L. Klein, W. Siemons, G. Rijnders, J. S. Dodge, C.-B. Eom, D. H. A. Blank, M. R. Beasley, *Rev. Mod. Phys.* **2012**, *84*, 253.
- [59] I. I. Mazin, D. J. Singh, Phys. Rev. B 1997, 56, 2556.
- [60] M. Cuoco, A. Di Bernardo, APL Mater. 2022, 10, 090902.
- [61] C. W. Jones, P. D. Battle, P. Lightfoot, W. T. A. Harrison, Acta Crystallogr., Sect. C: Struct. Chem. 1989, 45, 365.
- [62] P. A. Cox, R. G. Egdell, J. B. Goodenough, A. Hamnett, C. C. Naish, J. Phys. C: Solid State Phys. 1983, 16, 6221.
- [63] P. B. Allen, H. Berger, O. Chauvet, L. Forro, T. Jarlborg, A. Junod, B. Revaz, G. Santi, *Phys. Rev. B* **1996**, *53*, 4393.
- [64] S. A. Lee, S. Oh, J.-Y. Hwang, M. Choi, C. Youn, J. W. Kim, S. H. Chang, S. Woo, J.-S. Bae, S. Park, Y.-M. Kim, S. Lee, T. Choi, S. W. Kim, W. S. Choi, *Energy Environ. Sci.* 2017, 10, 974
- [65] C. B. Eom, R. J. Cava, R. M. Fleming, J. M. Phillips, R. B. van Dover, J. H. Marshall, J. W. P. Hsu, J. J. Krajewski, W. F. Peck, *Science* 1992, 258, 1766.
- [66] A. Rastogi, M. Brahlek, J. M. Ok, Z. Liao, C. Sohn, S. Feldman, H. N. Lee, APL Mater. 2019, 7, 091106.



16163028, 2023, 38, Downloaded from https://onlinelibrary.wiley.com/doi/10.1002/adfm.202301770 by University Of Temessee Gsm, Wiley Online Library on [14/04/2024]. See the Terms and Conditions (https://onlinelibrary.wiley.com/

litions) on Wiley Online Library for rules of use; OA articles are governed by the applicable Creative Commons I

- [67] H. Jeong, S. G. Jeong, A. Y. Mohamed, M. Lee, W.-s. Noh, Y. Kim, J.-S. Bae, W. S. Choi, D.-Y. Cho, Appl. Phys. Lett. 2019, 115, 092906.
- [68] S. H. Chang, Y. J. Chang, S. Y. Jang, D. W. Jeong, C. U. Jung, Y. J. Kim, J. S. Chung, T. W. Noh, *Phys. Rev. B* 2011, 84, 104101.
- [69] D. Kan, Y. Shimakawa, Cryst. Growth Des. 2011, 11, 5483.
- [70] S. G. Jeong, S. Y. Lim, J. Kim, S. Park, H. Cheong, W. S. Choi, Nanoscale 2020, 12, 13926.
- [71] D. W. Jeong, H. C. Choi, C. H. Kim, S. H. Chang, C. H. Sohn, H. J. Park, T. D. Kang, D.-Y. Cho, S. H. Baek, C. B. Eom, J. H. Shim, J. Yu, K. W. Kim, S. J. Moon, T. W. Noh, *Phys. Rev. Lett.* **2013**, *110*, 247202.
- [72] S. Hahn, B. Sohn, M. Kim, J. R. Kim, S. Huh, Y. Kim, W. Kyung, M. Kim, D. Kim, Y. Kim, T. W. Noh, J. H. Shim, C. Kim, *Phys. Rev. Lett.* 2021, 127, 256401.
- [73] D. Kan, R. Aso, R. Sato, M. Haruta, H. Kurata, Y. Shimakawa, *Nat. Mater.* 2016, 15, 432.
- [74] J. Matsuno, N. Ogawa, K. Yasuda, F. Kagawa, W. Koshibae, N. Nagaosa, Y. Tokura, M. Kawasaki, Sci. Adv. 2016, 2, e1600304.
- [75] J. Matsuno, K. Ihara, S. Yamamura, H. Wadati, K. Ishii, V. V. Shankar, H. Y. Kee, H. Takagi, *Phys. Rev. Lett.* 2015, 114, 247209.
- [76] L. Wang, Q. Feng, Y. Kim, R. Kim, K. H. Lee, S. D. Pollard, Y. J. Shin, H. Zhou, W. Peng, D. Lee, W. Meng, H. Yang, J. H. Han, M. Kim, Q. Lu, T. W. Noh, *Nat. Mater.* 2018, 17, 1087.
- [77] B. Sohn, B. Kim, S. Y. Park, H. Y. Choi, J. Y. Moon, T. Choi, Y. J. Choi, H. Zhou, J. W. Choi, A. Bombardi, D. G. Porter, S. H. Chang, J. H. Han, C. Kim, *Phys. Rev. Res.* **2021**, *3*, 023232.
- [78] B. Sohn, E. Lee, S. Y. Park, W. Kyung, J. Hwang, J. D. Denlinger, M. Kim, D. Kim, B. Kim, H. Ryu, S. Huh, J. S. Oh, J. K. Jung, D. Oh, Y. Kim, M. Han, T. W. Noh, B.-J. Yang, C. Kim, *Nat. Mater.* 2021, 20, 1643.
- [79] W. Lin, L. Liu, Q. Liu, L. Li, X. Shu, C. Li, Q. Xie, P. Jiang, X. Zheng, R. Guo, Z. Lim, S. Zeng, G. Zhou, H. Wang, J. Zhou, P. Yang, Ariando, S. J. Pennycook, X. Xu, Z. Zhong, Z. Wang, J. Chen, Adv. Mater. 2021, 33, 2101316.
- [80] Z. Fang, N. Nagaosa, K. S. Takahashi, A. Asamitsu, R. Mathieu, T. Ogasawara, H. Yamada, M. Kawasaki, Y. Tokura, K. Terakura, *Science* 2003. 302, 92.
- [81] S. Itoh, Y. Endoh, T. Yokoo, S. Ibuka, J.-G. Park, Y. Kaneko, K. S. Takahashi, Y. Tokura, N. Nagaosa, Nat. Commun. 2016, 7, 11788.
- [82] K. Jenni, S. Kunkemöller, D. Brüning, T. Lorenz, Y. Sidis, A. Schneidewind, A. A. Nugroho, A. Rosch, D. I. Khomskii, M. Braden, Phys. Rev. Lett. 2019, 123, 017202.
- [83] Z. Wang, H. P. Nair, G. C. Correa, J. Jeong, K. Lee, E. S. Kim, A. Seidner H, C. S. Lee, A. J. Lim, D. A. Muller, D. G. Schlom, APL Mater.. 2018, 6, 086101.
- [84] D. Popescu, B. Popescu, G. Jegert, S. Schmelzer, U. Boettger, P. Lugli, IEEE Trans. Electron Devices 2014, 61, 2130.
- [85] H. M. Kim, J. H. Lee, A. Yom, H. S. Lee, D. G. Kim, D. W. Ko, H. S. Kim, J.-H. Ahn, J. Alloys Compd. 2021, 857, 157627.
- [86] M. Izumi, K. Nakazawa, Y. Bando, J. Phys. Soc. Jpn. 1998, 67, 651.
- [87] M. Izumi, K. Nakazawa, Y. Bando, Y. Yoneda, H. Terauchi, Solid State Ionics 1998, 108, 227.
- [88] S. G. Jeong, A. Seo, W. S. Choi, Adv. Sci. 2022, 9, 2103403.
- [89] S. G. Jeong, H. Kim, S. J. Hong, D. Suh, W. S. Choi, ACS Appl. Nano Mater. 2021, 4, 2160.
- [90] S. W. Cho, S. G. Jeong, H. Y. Kwon, S. Song, S. Han, J. H. Han, S. Park, W. S. Choi, S. Lee, J. W. Choi, Acta Mater. 2021, 216, 117153.
- [91] S. G. Jeong, G. Han, S. Song, T. Min, A. Y. Mohamed, S. Park, J. Lee, H. Y. Jeong, Y.-M. Kim, D.-Y. Cho, W. S. Choi, Adv. Sci. 2020, 7, 2001643.
- [92] S. G. Jeong, T. Min, S. Woo, J. Kim, Y.-Q. Zhang, S. W. Cho, J. Son, Y.-M. Kim, J. H. Han, S. Park, H. Y. Jeong, H. Ohta, S. Lee, T. W. Noh, J. Lee, W. S. Choi, *Phys. Rev. Lett.* **2020**, *124*, 026401.
- [93] S. G. Jeong, S. Song, S. Park, V. Lauter, W. S. Choi, Small Methods 2023, 7, 2201386.

- [94] S. G. Jeong, W. S. Choi, A. Y. Mohamed, D.-Y. Cho, J. Korean Phys. Soc. 2023, 82, 386.
- [95] C. v. Korff Schmising, A. Harpoeth, N. Zhavoronkov, Z. Ansari, C. Aku-Leh, M. Woerner, T. Elsaesser, M. Bargheer, M. Schmidbauer, I. Vrejoiu, D. Hesse, M. Alexe, *Phys. Rev. B* 2008, 78, 060404.
- [96] M. Kim, C.-J. Kang, J.-H. Han, K. Kim, B. Kim, Phys. Rev. B 2022, 106, L201103.
- [97] B. Kim, S. Khmelevskyi, C. Franchini, I. I. Mazin, K. Kim, Phys. Rev. B 2020, 101, 220502.
- [98] P.-C. Wu, H. Song, Y. Yuan, B. Feng, Y. Ikuhara, R. Huang, P. Yu, C.-G. Duan, Y.-H. Chu, *Phys. Rev. Mater.* **2020**, *4*, 014401.
- [99] J. Zhang, L. Cheng, H. Cao, M. Bao, J. Zhao, X. Liu, A. Zhao, Y. Choi, H. Zhou, P. Shafer, X. Zhai, *Nano Res.* 2022, 15, 7584.
- [100] F. Bern, M. Ziese, A. Setzer, E. Pippel, D. Hesse, I. Vrejoiu, J. Phys.: Condens. Matter 2013, 25, 496003.
- [101] M. Gu, Q. Xie, X. Shen, R. Xie, J. Wang, G. Tang, D. Wu, G. P. Zhang, X. S. Wu, Phys. Rev. Lett. 2012, 109, 157003.
- [102] M. Verissimo-Alves, P. García-Fernández, D. I. Bilc, P. Ghosez, J. Junquera, Phys. Rev. Lett. 2012, 108, 107003.
- [103] C.-Y. Yang, P.-C. Wu, Y.-H. Chu, K.-H. Lin, New J. Phys. 2021, 23, 053009.
- [104] P. García-Fernández, M. Verissimo-Alves, D. I. Bilc, P. Ghosez, J. Junquera, Phys. Rev. B 2012, 86, 085305.
- [105] H. Boschker, T. Harada, T. Asaba, R. Ashoori, A. V. Boris, H. Hilgenkamp, C. R. Hughes, M. E. Holtz, L. Li, D. A. Muller, H. Nair, P. Reith, X. Renshaw Wang, D. G. Schlom, A. Soukiassian, J. Mannhart, *Phys. Rev. X* 2019, *9*, 011027.
- [106] M. Gu, K. Wang, Y. Wang, Q. Xie, H. Cai, G.-P. Zhang, X. Wu, npj Quantum Mater. 2016, 1, 16011.
- [107] Z. Cui, A. J. Grutter, H. Zhou, H. Cao, Y. Dong, D. A. Gilbert, J. Wang, Y.-S. Liu, J. Ma, Z. Hu, J. Guo, J. Xia, B. J. Kirby, P. Shafer, E. Arenholz, H. Chen, X. Zhai, Y. Lu, Sci. Adv. 2020, 6, eaay0114.
- [108] A. Bojahr, D. Schick, L. Maerten, M. Herzog, I. Vrejoiu, C. von Korff Schmising, C. Milne, S. L. Johnson, M. Bargheer, *Phys. Rev. B* 2012, 85, 224302.
- [109] H.-J. Liu, M. Ye, C.-Y. Yang, Y.-W. Fang, Y.-Y. Chin, C.-Y. Chen, R. T. Hung, Y. Zhu, L.-C. He, M.-Y. Huang, L. Chen, M. Gu, S. Ke, Y.-F. Liao, K.-D. Tsuei, H.-J. Lin, C.-T. Chen, S. Agrestini, J. Herrero-Martin, C.-H. Lai, Appl. Mater. Today 2021, 24, 101101.
- [110] J. L. Lin, Y. Sun, R. He, Y. Li, Z. Zhong, P. Gao, X. Zhao, Z. Zhang, Z. J. Wang, *Nano Lett.* 2022, 22, 7104.
- [111] K. Ueda, H. Saeki, H. Tabata, T. Kawai, Solid State Commun. 2000, 116, 221.
- [112] M. Ye, S. Hu, Y. Zhu, Y. Zhang, S. Ke, L. Xie, Y. Zhang, S. Hu, D. Zhang, Z. Luo, M. Gu, J. He, P. Zhang, W. Zhang, L. Chen, *Nano Lett.*. 2021, 21, 144.
- [113] C. v. Korff Schmising, M. Bargheer, M. Kiel, N. Zhavoronkov, M. Woerner, T. Elsaesser, I. Vrejoiu, D. Hesse, M. Alexe, *Phys. Rev. Lett.* 2007, 98, 257601.
- [114] M. Hadjimichael, Y. Li, L. Yedra, B. Dkhil, P. Zubko, Phys. Rev. Mater. 2020, 4, 094415.
- [115] J. L. Lin, Z. J. Wang, X. Zhao, Z. D. Zhang, Ceram. Int. 2020, 46, 9328.
- [116] Z. Q. Liu, Y. Ming, W. M. Lü, Z. Huang, X. Wang, B. M. Zhang, C. J. Li, K. Gopinadhan, S. W. Zeng, A. Annadi, Y. P. Feng, T. Venkatesan, Ariando, Appl. Phys. Lett. 2012, 101, 223105.
- [117] S. Lin, Q. Zhang, X. Sang, J. Zhao, S. Cheng, A. Huon, Q. Jin, S. Chen, S. Chen, W. Cui, H. Guo, M. He, C. Ge, C. Wang, J. Wang, M. R. Fitzsimmons, L. Gu, T. Zhu, K. Jin, E.-J. Guo, *Nano Lett.* 2021, 21, 3146
- [118] M. Ziese, I. Vrejoiu, D. Hesse, Appl. Phys. Lett. 2010, 97, 052504.
- [119] S. Thota, Q. Zhang, F. Guillou, U. Lüders, N. Barrier, W. Prellier, A. Wahl, P. Padhan, Appl. Phys. Lett. 2010, 97, 112506.
- [120] Y. Shiomi, Y. Handa, T. Kikkawa, E. Saitoh, Phys. Rev. B 2015, 92, 024418.

16163028, 2023, 38, Downloaded from https://onlinelibrary.wiley.com/doi/10.1002/adfm.202301770 by University Of Tennessee Gsm, Wiley Online Library on [14/04/2024]. See the Terms and Conditions (https://onlinelibrary.wiley.

) on Wiley Online Library for rules of use; OA articles are governed by the applicable Creative Commons

- [121] K. Lv, H. P. Zhu, W. Q. Zou, F. M. Zhang, X. S. Wu, J. Appl. Phys. 2015, 117, 185305.
- [122] I. Lindfors-Vrejoiu, M. Ziese, Phys. Status Solidi B 2017, 254, 1600556.
- [123] R. S. Helen, W. Prellier, P. Padhan, J. Appl. Phys. 2020, 128, 033906.
- [124] M. Ziese, E. Pippel, E. Nikulina, M. Arredondo, I. Vrejoiu, Nanotechnology 2011, 22, 254025.
- [125] M. Ziese, I. Lindfors-Vrejoiu, J. Appl. Phys. 2018, 124, 163905.
- [126] B. C. Behera, P. Padhan, W. Prellier, J. Magn. Magn. Mater. 2015, 388,
- [127] M. Ziese, Phys. Status Solidi RRL 2011, 5, 444.
- [128] I. Razdolski, R. R. Subkhangulov, D. G. Gheorghe, F. Bern, I. Vrejoiu, A. V. Kimel, A. Kirilyuk, M. Ziese, T. Rasing, Phys. Status Solidi RRL **2015**. 9. 583.
- [129] B. C. Behera, A. V. Ravindra, P. Padhan, W. Prellier, Appl. Phys. Lett. 2014, 104, 092406.
- [130] R. Hillebrand, E. Pippel, D. Hesse, I. Vrejoiu, Phys. Status Solidi A 2011, 208, 2144.
- [131] S. N. Jammalamadaka, J. Vanacken, V. V. Moshchalkov, Appl. Phys. Lett. 2014, 105, 033505.
- [132] P. Padhan, W. Prellier, Appl. Phys. Lett. 2011, 99, 263108.
- [133] M. Ziese, F. Bern, E. Pippel, D. Hesse, I. Vrejoiu, Nano Lett.. 2012, 12, 4276.
- [134] S. Das, A. Herklotz, E. Pippel, E. J. Guo, D. Rata, K. Dörr, Phys. Rev. B 2015, 91, 134405.
- [135] Roshna S. H., W. Prellier, P. Padhan, Nanoscale 2020, 12, 5151.
- [136] M. Ziese, I. Vrejoiu, E. Pippel, P. Esquinazi, D. Hesse, C. Etz, J. Henk, A. Ernst, I. V. Maznichenko, W. Hergert, I. Mertig, Phys. Rev. Lett. 2010, 104, 167203.
- [137] Y. Shiomi, Y. Handa, T. Kikkawa, E. Saitoh, Appl. Phys. Lett. 2015, 106, 232403.
- [138] M. Ziese, L. Jin, I. Lindfors-Vrejoiu, J. Phys.: Condens. Mater. 2019, 2,
- [139] M. Ziese, I. Vrejoiu, Phys. Rev. B 2011, 84, 104413.
- [140] M. Ziese, F. Bern, I. Vrejoiu, J. Appl. Phys. 2013, 113, 063911.
- [141] M. Ziese, I. Vrejoiu, E. Pippel, A. Hähnel, E. Nikulina, D. Hesse, J. Phys. D: Appl. Phys. 2011, 44, 345001.
- [142] R. Hillebrand, E. Pippel, I. Vrejoiu, D. Hesse, Phys. Status Solidi A **2014**, 211, 536.
- [143] M. Ziese, I. Vrejoiu, Phys. Status Solidi RRL 2013, 7, 243.
- [144] L. Qu, D. Lan, L. Si, C. Ma, S. Wang, L. Xu, K. Zhang, F. Jin, Z. Zhang, E. Hua, B. Chen, G. Gao, F. Chen, H. Du, K. Held, L. Wang, W. Wu, Nano Res. 2021, 14, 3621.
- [145] L. Qu, D. Lan, K. Zhang, E. Hua, B. Ge, L. Xu, F. Jin, G. Gao, L. Wang, W. Wu, AIP Adv. 2021, 11, 075001.
- [146] G. Q. Gong, A. Gupta, G. Xiao, P. Lecoeur, T. R. McGuire, Phys. Rev. B **1996**, *54*, R3742,
- [147] A. Sahoo, W. Prellier, P. Padhan, Adv. Mater. Interfaces 2018, 5, 1800913.
- [148] A. Sahoo, P. Padhan, W. Prellier, ACS Appl. Mater. Interfaces 2017, 9, 36423.
- [149] A. Sahoo, W. Prellier, P. Padhan, ACS Appl. Mater. Interfaces 2018, 10, 44190.
- [150] S. Dong, Q. Zhang, S. Yunoki, J. M. Liu, E. Dagotto, Phys. Rev. B **2011**, *84*, 224437.
- [151] P. Padhan, W. Prellier, Eur. Phys. J. B 2005, 45, 169.
- [152] P. Padhan, W. Prellier, Appl. Phys. Lett. 2006, 88, 263114.
- [153] Y. Choi, Y. C. Tseng, D. Haskel, D. E. Brown, D. Danaher, O. Chmaissem, Appl. Phys. Lett. 2008, 93, 192509.
- [154] P. Padhan, W. Prellier, B. Mercey, Phys. Rev. B 2004, 70, 184419.
- [155] Y.-Z. Yoo, O. Chmaissem, J.-H. Song, Curr. Appl. Phys. 2014, 14, 378.
- [156] W. Wang, H. Zhang, X. Shen, X. Guan, Y. Yao, Y. Wang, J. Sun, R. Yu, J. Cryst. Growth 2018, 490, 110.
- [157] P. Liu, X. Ning, Mater. Res. Lett. 2020, 8, 173.

- [158] X. Yao, C. Wang, E.-J. Guo, X. Wang, X. Li, L. Liao, Y. Zhou, S. Lin, Q. Jin, C. Ge, M. He, X. Bai, P. Gao, G. Yang, K.-J. Jin, ACS Appl. Mater. Interfaces 2022, 14, 6194.
- [159] A. Singh, J. Chen, Ceram. Int. 2019, 45, 20465.
- [160] S. Yousfi, M. El Marssi, H. Bouyanfif, Superlattices Microstruct. 2021, 156, 106983.
- [161] Z. Zeng, J. Feng, X. Zheng, C. Wang, J. Liu, Z. Lu, F.-X. Jiang, X.-H. Xu, Z. Wang, R.-W. Li, Appl. Phys. Lett. 2020, 116, 142401.
- [162] L. Yang, L. Wysocki, J. Schöpf, L. Jin, A. Kovács, F. Gunkel, R. Dittmann, P. H. M. van Loosdrecht, I. Lindfors-Vrejoiu, Phys. Rev. Mater. 2021, 5, 014403.
- [163] B. Pang, L. Zhang, Y. B. Chen, J. Zhou, S. Yao, S. Zhang, Y. Chen, ACS Appl. Mater. Interfaces 2017, 9, 3201.
- [164] L. Wysocki, J. Schöpf, M. Ziese, L. Yang, A. Kovács, L. Jin, R. B. Versteeg, A. Bliesener, F. Gunkel, L. Kornblum, R. Dittmann, P. H. M. van Loosdrecht, I. Lindfors-Vrejoiu, ACS Omega 2020, 5,
- [165] A. Herklotz, K. Dörr, Eur. Phys. J. B 2015, 88, 60.
- [166] S. J. May, J. W. Kim, J. M. Rondinelli, E. Karapetrova, N. A. Spaldin, A. Bhattacharya, P. J. Ryan, Phys. Rev. B 2010, 82, 014110.
- [167] A. A. Balandin, E. P. Pokatilov, D. L. Nika, J. Nanoelectron. Optoelectron. 2007, 2, 140.
- [168] A. Bartels, T. Dekorsy, H. Kurz, K. Köhler, Phys. Rev. Lett. 1999, 82, 1044.
- [169] T. A. Palomaki, J. W. Harlow, J. D. Teufel, R. W. Simmonds, K. W. Lehnert, Nature 2013, 495, 210.
- [170] R. W. Andrews, R. W. Peterson, T. P. Purdy, K. Cicak, R. W. Simmonds, C. A. Regal, K. W. Lehnert, Nat. Phys. 2014, 10, 321.
- [171] F. Massel, T. T. Heikkilä, J. M. Pirkkalainen, S. U. Cho, H. Saloniemi, P. J. Hakonen, M. A. Sillanpää, Nature 2011, 480, 351.
- [172] R. Manenti, A. F. Kockum, A. Patterson, T. Behrle, J. Rahamim, G. Tancredi, F. Nori, P. J. Leek, Nat. Commun. 2017, 8, 975.
- [173] D. Kirillov, Y. Suzuki, L. Antognazza, K. Char, I. Bozovic, T. H. Geballe, Phys. Rev. B 1995, 51, 12825.
- [174] M. N. Iliev, A. P. Litvinchuk, H. G. Lee, C. L. Chen, M. L. Dezaneti, C. W. Chu, V. G. Ivanov, M. V. Abrashev, V. N. Popov, Phys. Rev. B **1999** 59 364
- [175] L. Liu, O. Qin, W. Lin, C. Li, Q. Xie, S. He, X. Shu, C. Zhou, Z. Lim, J. Yu, W. Lu, M. Li, X. Yan, S. J. Pennycook, J. Chen, Nat. Nanotechnol. 2019, 14, 939.
- [176] M. Yamanouchi, Y. Araki, T. Sakai, T. Uemura, H. Ohta, J. I. Ieda, Sci. Adv. 2022, 8, eabl6192.
- [177] Y. Chen, D. L. Bergman, A. A. Burkov, Phys. Rev. B 2013, 88, 125110.
- [178] H. G. Lee, L. Wang, L. Si, X. He, D. G. Porter, J. R. Kim, E. K. Ko, J. Kim, S. M. Park, B. Kim, A. T. S. Wee, A. Bombardi, Z. Zhong, T. W. Noh, Adv. Mater. 2020, 32, 1905815.
- [179] Z. Zhong, P. Hansmann, Phys. Rev. X 2017, 7, 011023.
- [180] L. Sheng, D. N. Sheng, C. S. Ting, Phys. Rev. Lett. 2006, 96, 155901.
- [181] D. M. Juraschek, N. A. Spaldin, Phys. Rev. Mater. 2019, 3, 064405.
- [182] V. L. Korenev, M. Salewski, I. A. Akimov, V. F. Sapega, L. Langer, I. V. Kalitukha, J. Debus, R. I. Dzhioev, D. R. Yakovlev, D. Müller, C. Schröder, H. Hövel, G. Karczewski, M. Wiater, T. Wojtowicz, Y. G. Kusrayev, M. Bayer, Nat. Phys. 2016, 12, 85.
- [183] D. Liu, J. Shi, Phys. Rev. Lett. 2017, 119, 075301.
- [184] G. Grissonnanche, S. Thériault, A. Gourgout, M. E. Boulanger, E. Lefrançois, A. Ataei, F. Laliberté, M. Dion, J. S. Zhou, S. Pyon, T. Takayama, H. Takagi, N. Doiron-Leyraud, L. Taillefer, Nat. Phys. **2020**, 16, 1108.
- [185] D. Kan, T. Moriyama, K. Kobayashi, Y. Shimakawa, Phys. Rev. B 2018, 98, 180408.
- [186] H. Huang, S.-J. Lee, B. Kim, B. Sohn, C. Kim, C.-C. Kao, J.-S. Lee, ACS Appl. Mater. Interfaces 2020, 12, 37757.
- [187] L. Hao, D. Yi, M. Wang, J. Liu, P. Yu, Fundam. Res. 2022, https://doi. org/10.1016/j.fmre.2022.09.030.

- [188] W. Witczak-Krempa, G. Chen, Y. B. Kim, L. Balents, Annu. Rev. Condens. Matter Phys. 2014, 5, 57.
- [189] J. G. Rau, E. K.-H. Lee, H.-Y. Kee, Annu. Rev. Condens. Matter Phys. 2016, 7, 195.
- [190] R. Schaffer, E. K. H. Lee, B. J. Yang, Y. B. Kim, Rep. Prog. Phys. 2016, 79, 094504.
- [191] G. Cao, P. Schlottmann, Rep. Prog. Phys. 2018, 81, 042502.
- [192] J. Bertinshaw, Y. K. Kim, G. Khaliullin, B. J. Kim, Annu. Rev. Condens. Matter Phys. 2019, 10, 315.
- [193] A. Biswas, Y. H. Jeong, Curr. Appl. Phys. 2017, 17, 605.
- [194] B. J. Kim, H. Jin, S. J. Moon, J. Y. Kim, B. G. Park, C. S. Leem, J. Yu, T. W. Noh, C. Kim, S. J. Oh, J. H. Park, V. Durairaj, G. Cao, E. Rotenberg, *Phys. Rev. Lett.* **2008**, *101*, 076402.
- [195] S. J. Moon, H. Jin, K. W. Kim, W. S. Choi, Y. S. Lee, J. Yu, G. Cao, A. Sumi, H. Funakubo, C. Bernhard, T. W. Noh, *Phys. Rev. Lett.* 2008, 101, 226402.
- [196] F. Wang, T. Senthil, Phys. Rev. Lett. 2011, 106, 136402.
- [197] H. Watanabe, T. Shirakawa, S. Yunoki, Phys. Rev. Lett. 2013, 110, 027002.
- [198] G. Jackeli, G. Khaliullin, Phys. Rev. Lett. 2009, 102, 017205.
- [199] L. Hao, D. Meyers, C. Frederick, G. Fabbris, J. Yang, N. Traynor, L. Horak, D. Kriegner, Y. Choi, J.-W. Kim, D. Haskel, P. J. Ryan, M. P. M. Dean, J. Liu, Phys. Rev. Lett. 2017, 119, 027204.
- [200] B. Kim, P. Liu, C. Franchini, Phys. Rev. B 2017, 95, 115111.
- [201] J. Hubbard, Proc. R. Soc. London, Ser. A 1963, 276, 238.
- [202] S. Y. Kim, C. H. Kim, L. J. Sandilands, C. H. Sohn, J. Matsuno, H. Takagi, K. W. Kim, Y. S. Lee, S. J. Moon, T. W. Noh, *Phys. Rev. B* 2016, 94 245113
- [203] D. Meyers, Y. Cao, G. Fabbris, N. J. Robinson, L. Hao, C. Frederick, N. Traynor, J. Yang, J. Lin, M. H. Upton, D. Casa, J.-W. Kim, T. Gog, E. Karapetrova, Y. Choi, D. Haskel, P. J. Ryan, L. Horak, X. Liu, J. Liu, M. P. M. Dean, Sci. Rep. 2019, 9, 4263.
- [204] D. Gong, J. Yang, L. Hao, L. Horak, Y. Xin, E. Karapetrova, J. Strempfer, Y. Choi, J.-W. Kim, P. J. Ryan, J. Liu, *Phys. Rev. Lett.* 2022, 129, 187201.
- [205] L. Hao, D. Meyers, H. Suwa, J. Yang, C. Frederick, T. R. Dasa, G. Fabbris, L. Horak, D. Kriegner, Y. Choi, J.-W. Kim, D. Haskel, P. J. Ryan, H. Xu, C. D. Batista, M. P. M. Dean, J. Liu, Nat. Phys. 2018, 14, 806
- [206] J. Yang, H. Suwa, D. Meyers, H. Zhang, L. Horak, Z. Wang, G. Fabbris, Y. Choi, J. Karapetrova, J.-W. Kim, D. Haskel, P. J. Ryan, M. P. M. Dean, L. Hao, J. Liu, Phys. Rev. X 2022, 12, 031015.
- [207] M.-W. Yoo, J. Tornos, A. Sander, L.-F. Lin, N. Mohanta, A. Peralta, D. Sanchez-Manzano, F. Gallego, D. Haskel, J. W. Freeland, D. J. Keavney, Y. Choi, J. Strempfer, X. Wang, M. Cabero, H. B. Vasili, M. Valvidares, G. Sanchez-Santolino, J. M. Gonzalez-Calbet, A. Rivera, C. Leon, S. Rosenkranz, M. Bibes, A. Barthelemy, A. Anane, E. Dagotto, S. Okamoto, S. G. E. te Velthuis, J. Santamaria, J. E. Villegas, Nat. Commun. 2021, 12, 3283.
- [208] D. Yi, J. Liu, S. L. Hsu, L. P. Zhang, Y. Choi, J. W. Kim, Z. H. Chen, J. D. Clarkson, C. R. Serrao, E. Arenholz, P. J. Ryan, H. X. Xu, R. J. Birgeneau, R. Ramesh, *Proc. Natl. Acad. Sci. USA* 2016, 113, 6397.
- [209] J. W. Kim, Y. Choi, S. H. Chun, D. Haskel, D. Yi, R. Ramesh, J. Liu, P. J. Ryan, Phys. Rev. B 2018, 97, 094426.
- [210] D. Yi, C. L. Flint, P. P. Balakrishnan, K. Mahalingam, B. Urwin, A. Vailionis, A. T. N'Diaye, P. Shafer, E. Arenholz, Y. Choi, K. H. Stone, J.-H. Chu, B. M. Howe, J. Liu, I. R. Fisher, Y. Suzuki, *Phys. Rev. Lett.* 2017, 119, 077201.
- [211] D. Yi, Y. Wang, O. M. J. van 't Erve, L. Xu, H. Yuan, M. J. Veit, P. P. Balakrishnan, Y. Choi, A. T. N'Diaye, P. Shafer, E. Arenholz, A. Grutter, H. Xu, P. Yu, B. T. Jonker, Y. Suzuki, Nat. Commun. 2020, 11, 902.
- [212] J. Nichols, X. Gao, S. Lee, T. L. Meyer, J. W. Freeland, V. Lauter, D. Yi, J. Liu, D. Haskel, J. R. Petrie, E.-J. Guo, A. Herklotz, D. Lee, T. Z.

- Ward, G. Eres, M. R. Fitzsimmons, H. N. Lee, *Nat. Commun.* **2016**, *7*. 12721.
- [213] A. K. Jaiswal, D. Wang, V. Wollersen, R. Schneider, M. L. Tacon, D. Fuchs, Adv. Mater. 2022, 34, 2109163.
- [214] J. Liu, X. Zhang, Y. Ji, X. Gao, J. Wu, M. Zhang, L. Li, X. Liu, W. Yan, T. Yao, Y. Yin, L. Wang, H. Guo, G. Cheng, Z. Wang, P. Gao, Y. Wang, K. Chen, Z. Liao, J. Phys. Chem. Lett. 2022, 13, 11946.
- [215] A. K. Jaiswal, R. Schneider, M. L. Tacon, D. Fuchs, AIP Adv. 2022, 12, 035120.
- [216] E. Skoropata, J. Nichols, J. M. Ok, R. V. Chopdekar, E. S. Choi, A. Rastogi, C. Sohn, X. Gao, S. Yoon, T. Farmer, R. D. Desautels, Y. Choi, D. Haskel, J. W. Freeland, S. Okamoto, M. Brahlek, H. N. Lee, Sci. Adv. 2020, 6, eaaz3902.
- [217] X. Liu, M. Kotiuga, H.-S. Kim, A. T. N'Diaye, Y. Choi, Q. Zhang, Y. Cao, M. Kareev, F. Wen, B. Pal, J. W. Freeland, L. Gu, D. Haskel, P. Shafer, E. Arenholz, K. Haule, D. Vanderbilt, K. M. Rabe, J. Chakhalian, Proc. Natl. Acad. Sci. USA 2019, 116, 19863.
- [218] M. Gu, R. Zhu, X. Zhang, Z. Wang, Q. An, F. Yang, X. Liu, P. Gao, M. Meng, J. Guo, ACS Appl. Electron. Mater. 2022, 4, 3707.
- [219] K. H. Kim, H. S. Kim, M. J. Han, J. Phys.: Condens. Matter 2014, 26, 185501.
- [220] D. J. Groenendijk, N. Manca, G. Mattoni, L. Kootstra, S. Gariglio, Y. Huang, E. van Heumen, A. D. Caviglia, Appl. Phys. Lett. 2016, 109, 041906.
- [221] D. Hirai, J. Matsuno, H. Takagi, APL Mater. 2015, 3, 041508.
- [222] T. J. Anderson, S. Ryu, H. Zhou, L. Xie, J. P. Podkaminer, Y. Ma, J. Irwin, X. Q. Pan, M. S. Rzchowski, C. B. Eom, Appl. Phys. Lett. 2016, 108, 151604.
- [223] C. C. Fan, Z. T. Liu, S. H. Cai, Z. Wang, P. Xiang, K. L. Zhang, W. L. Liu, J. S. Liu, P. Wang, Y. Zheng, D. W. Shen, L. X. You, AIP Adv. 2017, 7, 085307.
- [224] A. M. Glazer, Acta Cryst. 1972, B28, 3384.
- [225] A. M. Glazer, Acta Cryst. 1975, A31, 756.
- [226] L. Shekhtman, O. Entin-Wohlman, A. Aharony, Phys. Rev. Lett. 1992, 69, 836.
- [227] M. P. M. Dean, R. S. Springell, C. Monney, K. J. Zhou, J. Pereiro, I. Božović, B. Dalla Piazza, H. M. Rønnow, E. Morenzoni, J. van den Brink, T. Schmitt, I. P. Hill, Nat. Mater. 2012, 11, 850.
- [228] S. Boseggia, R. Springell, H. C. Walker, H. M. Ronnow, C. Ruegg, H. Okabe, M. Isobe, R. S. Perry, S. P. Collins, D. F. McMorrow, Phys. Rev. Lett. 2013, 110, 117207.
- [229] L. Paolasini, École thématique de la Société Française de la Neutronique 2014. 13. 03002.
- [230] J. Stöhr, H. C. Siegmann, in Magnetism: From Fundamentals to Nanoscale Dynamics, Springer, Berlin 2006, pp. 351–429.
- [231] J. W. Kim, Y. Choi, J. Kim, J. F. Mitchell, G. Jackeli, M. Daghofer, J. van den Brink, G. Khaliullin, B. J. Kim, *Phys. Rev. Lett.* 2012, 109, 037204.
- [232] K. Ohgushi, J.-i. Yamaura, H. Ohsumi, K. Sugimoto, S. Takeshita, A. Tokuda, H. Takagi, M. Takata, T.-h. Arima, Phys. Rev. Lett. 2013, 110, 217212.
- [233] H. Kim, J. Bertinshaw, J. Porras, B. Keimer, J. Kim, J. W. Kim, J. Kim, J. Kim, G. Noh, G.-Y. Kim, S.-Y. Choi, B. J. Kim, *Phys. Rev. Res.* 2022, 4, 013229.
- [234] J. Kim, A. H. Said, D. Casa, M. H. Upton, T. Gog, M. Daghofer, G. Jackeli, J. van den Brink, G. Khaliullin, B. J. Kim, Phys. Rev. Lett. 2012, 109, 157402.
- [235] D. G. Mazzone, Y. Shen, H. Suwa, G. Fabbris, J. Yang, S. S. Zhang, H. Miao, J. Sears, K. Jia, Y. G. Shi, M. H. Upton, D. M. Casa, X. Liu, J. Liu, C. D. Batista, M. P. M. Dean, *Nat. Commun.* 2022, 13, 913.
- [236] A. Vasiliev, O. Volkova, E. Zvereva, M. Markina, npj Quantum Mater.. 2018, 3, 18.
- [237] M. Gibertini, M. Koperski, A. F. Morpurgo, K. S. Novoselov, Nat. Nanotechnol. 2019, 14, 408.
- [238] N. D. Mermin, H. Wagner, Phys. Rev. Lett. 1966, 17, 1133.



www.advancedsciencenews.com

FUNCTIONAL MATERIALS

www.afm-journal.de

16163028, 2023, 38, Downloaded from https://onlinelibrary.wiley.com/doi/10.1002/adfm.202301770 by University Of Temessee Gsm, Wiley Online Library on [14/04/2024]. See the Terms and Conditions (https://onlinelibrary.wiley.com/doi/10.1002/adfm.202301770 by University Of Temessee Gsm, Wiley Online Library on [14/04/2024]. See the Terms and Conditions (https://onlinelibrary.wiley.com/doi/10.1002/adfm.202301770 by University Of Temessee Gsm, Wiley Online Library on [14/04/2024]. See the Terms and Conditions (https://onlinelibrary.wiley.com/doi/10.1002/adfm.202301770 by University Of Temessee Gsm, Wiley Online Library on [14/04/2024]. See the Terms and Conditions (https://onlinelibrary.wiley.com/doi/10.1002/adfm.202301770 by University Of Temessee Gsm, Wiley Online Library on [14/04/2024]. See the Terms and Conditions (https://onlinelibrary.wiley.com/doi/10.1002/adfm.202301770 by University Of Temessee Gsm, Wiley Online Library on [14/04/2024].

nditions) on Wiley Online Library for rules of use; OA articles are governed by the applicable Creative Con

- [239] E. Manousakis, Rev. Mod. Phys. 1991, 63, 1.
- [240] E. Dagotto, Rev. Mod. Phys. 1994, 66, 763.
- [241] L. Hao, D. Meyers, M. P. M. Dean, J. Liu, J. Phys. Chem. Solids 2019, 128, 39.
- [242] L. Néel, Nobel Lectures, Physics 1970, 1963. https://www.nobelprize. org/uploads/2018/06/neel-lecture.pdf Accessed: May 2023
- [243] V. Baltz, A. Manchon, M. Tsoi, T. Moriyama, T. Ono, Y. Tserkovnyak, Rev. Mod. Phys. 2018, 90, 015005.
- [244] C. Song, Y. You, X. Chen, X. Zhou, Y. Wang, F. Pan, Nanotechnology 2018, 29, 112001.
- [245] T. Jungwirth, X. Marti, P. Wadley, J. Wunderlich, *Nat. Nanotechnol.* 2016, 11, 231.
- [246] P. Wadley, B. Howells, J. Železný, C. Andrews, V. Hills, R. P. Campion, V. Novák, K. Olejník, F. Maccherozzi, S. S. Dhesi, S. Y. Martin, T. Wagner, J. Wunderlich, F. Freimuth, Y. Mokrousov, J. Kuneš, J. S. Chauhan, M. J. Grzybowski, A. W. Rushforth, K. W. Edmonds, B. L. Gallagher, T. Jungwirth, *Science* 2016, 351, 587.
- [247] B. H. Brandow, Adv. Phys. 1977, 26, 651.
- [248] P. A. Lee, N. Nagaosa, X.-G. Wen, Rev. Mod. Phys. 2006, 78, 17.
- [249] J. Yang, L. Hao, D. Meyers, T. Dasa, L. Xu, L. Horak, P. Shafer, E. Arenholz, G. Fabbris, Y. Choi, D. Haskel, J. Karapetrova, J.-W. Kim, P. J. Ryan, H. Xu, C. D. Batista, M. P. M. Dean, J. Liu, *Phys. Rev. Lett.* 2020, 124, 177601.
- [250] H.-J. Noh, S. J. Oh, B. G. Park, J. H. Park, J. Y. Kim, H. D. Kim, T. Mizokawa, L. H. Tjeng, H. J. Lin, C. T. Chen, S. Schuppler, S. Nakatsuji, H. Fukazawa, Y. Maeno, *Phys. Rev. B* **2005**, *72*, 052411.
- [251] S. J. Moon, M. W. Kim, K. W. Kim, Y. S. Lee, J. Y. Kim, J. H. Park, B. J. Kim, S. J. Oh, S. Nakatsuji, Y. Maeno, I. Nagai, S. I. Ikeda, G. Cao, T. W. Noh, *Phys. Rev. B* **2006**, *74*, 113104.
- [252] T. Moriya, Phys. Rev. 1960, 120, 91.
- [253] J. P. F. LeBlanc, A. E. Antipov, F. Becca, I. W. Bulik, G. K.-L. Chan, C.-M. Chung, Y. Deng, M. Ferrero, T. M. Henderson, C. A. Jiménez-Hoyos, E. Kozik, X.-W. Liu, A. J. Millis, N. V. Prokof'ev, M. Qin, G. E. Scuseria, H. Shi, B. V. Svistunov, L. F. Tocchio, I. S. Tupitsyn, S. R. White, S. Zhang, B.-X. Zheng, Z. Zhu, E. Gull, *Phys. Rev. X* 2015, 5, 041041
- [254] L. Hao, Z. Wang, J. Yang, D. Meyers, J. Sanchez, G. Fabbris, Y. Choi, J.-W. Kim, D. Haskel, P. J. Ryan, K. Barros, J.-H. Chu, M. P. M. Dean, C. D. Batista, J. Liu, *Nat. Commun.* 2019, 10, 5301.
- [255] C. Haas, Phys. Rev. 1968, 168, 531.
- [256] S. Alexander, J. S. Helman, I. Balberg, Phys. Rev. B 1976, 13, 304.

- [257] A. R. Bishop, H. Roder, Curr. Opin. Solid State Mater. Sci. 1997, 2, 244.
- [258] A. P. Ramirez, J. Phys.: Condens. Matter 1997, 9, 8171.
- [259] J. Z. Sun, A. Gupta, Annu. Rev. Mater. Sci. 1998, 28, 45.
- [260] E. Dagotto, T. Hotta, A. Moreo, Phys. Rep. 2001, 344, 1.
- [261] M. B. Salamon, M. Jaime, Rev. Mod. Phys. 2001, 73, 583.
- [262] M. Ziese, Rep. Prog. Phys. 2002, 65, 143.
- [263] Y. Ando, J. Phys. Soc. Jpn. 2013, 82, 102001.
- [264] M. Z. Hasan, C. L. Kane, Rev. Mod. Phys. 2010, 82, 3045.
- [265] Y. Tokura, Nat. Mater. 2022, 21, 971.
- [266] N. Nagaosa, J. Sinova, S. Onoda, A. H. MacDonald, N. P. Ong, Rev. Mod. Phys. 2010, 82, 1539.
- [267] D. Xiao, M.-C. Chang, Q. Niu, Rev. Mod. Phys. 2010, 82, 1959.
- [268] Y. Chen, Y.-M. Lu, H.-Y. Kee, Nat. Commun. 2015, 6, 6593.
- [269] X. Liu, W. Song, M. Wu, Y. Yang, Y. Yang, P. Lu, Y. Tian, Y. Sun, J. Lu, J. Wang, D. Yan, Y. Shi, N. X. Sun, Y. Sun, P. Gao, K. Shen, G. Chai, S. Kou, C.-W. Nan, J. Zhang, Nat. Commun. 2021, 12, 5453.
- [270] J. H. Gruenewald, J. Kim, H. S. Kim, J. M. Johnson, J. Hwang, M. Souri, J. Terzic, S. H. Chang, A. Said, J. W. Brill, G. Cao, H.-Y. Kee, S. S. A. Seo, Adv. Mater. 2017, 29, 1603798.
- [271] H. Xu, H. Huang, Q. Wu, Z. Wang, Z. Cui, X. Zhai, J. Wang, Z. Fu, Y. Lu, J. Mater. Sci. 2020, 55, 8211.
- [272] S. Y. Jang, H. Kim, S. J. Moon, W. S. Choi, B. C. Jeon, J. Yu, T. W. Noh, J. Phys.: Condens. Matter 2010, 22, 485602.
- [273] Z. S. Lim, C. Li, X. Chi, G. J. Omar, H. H. Ma, Z. Huang, S. Zeng, P. Yang, T. Venkatesan, A. Rusydi, S. J. Pennycook, A. Ariando, *Nano Lett.* 2020, 20, 1890.
- [274] M. Vagadia, S. Sardar, T. Tank, S. Das, B. Gunn, P. Pandey, R. Hübner, F. Rodolakis, G. Fabbris, Y. Choi, D. Haskel, A. Frano, D. S. Rana, *Phys. Rev. B* 2022, 105, L020402.
- [275] J. G. Cheng, T. Ishii, H. Kojitani, K. Matsubayashi, A. Matsuo, X. Li, Y. Shirako, J. S. Zhou, J. B. Goodenough, C. Q. Jin, M. Akaogi, Y. Uwatoko, Phys. Rev. B 2013, 88, 205114.
- [276] T. R. Dasa, L. Hao, J. Liu, H. Xu, J. Mater. Chem. C 2019, 7, 13294.
- [277] Q. Cui, J. G. Cheng, W. Fan, A. E. Taylor, S. Calder, M. A. McGuire, J. Q. Yan, D. Meyers, X. Li, Y. Q. Cai, Y. Y. Jiao, Y. Choi, D. Haskel, H. Gotou, Y. Uwatoko, J. Chakhalian, A. D. Christianson, S. Yunoki, J. B. Goodenough, J. S. Zhou, *Phys. Rev. Lett.* 2016, 117, 176603.
- [278] J. Yang, L. Hao, Q. Cui, J. Lin, L. Horak, X. Liu, L. Zhang, H. Yang, J. Karapetrova, J.-W. Kim, P. J. Ryan, M. P. M. Dean, J. Cheng, J. Liu, *Phys. Rev. Mater.* 2019, 3, 124411.



Seung Gyo Jeong received his Ph.D. in physics from Sungkyunkwan University in 2022. After that, he worked as a postdoctoral researcher at the Institute of Basic Science at Sungkyunkwan University. He was honored the Sejong Science Fellowship from the National Research Foundation of Korea and the Duk Joo Kim Young Scientist Award from Korean Physical Society. His research area of interest involves exploring spin-related quantum phenomena in complex oxide heterostructures and superlattices that grown through atomic scale epitaxy.

16163028, 2023, 38, Downloaded from https://onlinelibrary.wiley.com/doi/10.1002/adfm.202301770 by University Of Tennessee Gsm, Wiley Online Library on [14/04/2024]. See the Terms and Conditions (https://onlinelibrary.wiley.com/terms

nditions) on Wiley Online Library for rules of use; OA articles are governed by the applicable Creative Commons I



Jin Young Oh received his B.S. from Sungkyunkwan University in 2020. He is currently in an integrated Ph.D. course under the supervision of Prof. Woo Seok Choi at Sungkyunkwan University. His research interest mainly focuses on functional oxide and emergent phenomena in those systems.



Lin Hao received his Ph.D. from The University of Science and Technology of China in 2016. He then moved to The University of Tennessee as a postdoc until 2020. In the end of 2020, he joined the high magnetic field lab as an experimental scientist. His group focuses on the designing, synthesizing, apprehending, and exploring emergent phenomena in strong spin—orbit coupled artificial structures.



Jian Liu obtained his Ph.D. in 2012 from the University of Arkansas. He was a postdoctoral fellow at the University of California-Berkeley from 2012 to 2015, and became an assistant professor in 2015 and an associate professor in 2021 at the University of Tennessee. He is a recipient of the CAREER award by the National Science Foundation and the Young Investigator Program award by the Office of Naval Research. His research currently focuses on emergent phenomena of quantum materials, especially complex oxides with strong spin—orbit coupling.



Woo Seok Choi is a professor in the Department of Physics, Sungkyunkwan University, Korea. He received his Ph.D. degree in physics from Seoul National University, Korea, in 2010. From 2010, he worked as a postdoctoral research associate in the Oak Ridge National Laboratory, USA. Since 2013, he has been a professor in Sungkyunkwan. University. His research interest lies in the field of emergent physical and chemical properties in complex oxide heterostructures with a particular emphasis on the growth of the epitaxial thin film and heterostructures with atomic scale precision.